2011

Thermomechanical Behavior Of High-temperature Shape Memory Alloy Ni-ti-pd-pt Actuators

Douglas E. Nicholson
University of Central Florida

STARS Citation

Nicholson, Douglas E., "Thermomechanical Behavior Of High-temperature Shape Memory Alloy Ni-ti-pd-pt Actuators" (2011). *Electronic Theses and Dissertations, 2004-2019*. 1785.
https://stars.library.ucf.edu/etd/1785

THERMOMECHANICAL BEHAVIOR OF HIGH-TEMPERATURE SHAPE MEMORY ALLOY Ni-Ti-Pd-Pt ACTUATORS

by

DOUGLAS E. NICHOLSON
B.S. Florida Atlantic University, 2008

A thesis submitted in partial fulfillment of the requirements
for the degree of Master of Science
in the Department of Mechanical, Materials and Aerospace Engineering
in the College of Engineering and Computer Science
at the University of Central Florida
Orlando, Florida

Fall Term
2011

ABSTRACT

To date the commercial use of shape memory alloys (SMAs) has been mostly limited to binary NiTi alloys with transformation temperatures approximately in the -100 to 100 ºC range. In an ongoing effort to develop high-temperature shape memory alloys (HTSMAs), ternary and quaternary additions are being made to binary NiTi to form NiTi-X (e.g., X: Pd, Pt, Au and Hf) alloys. Stability and repeatability can be further increased at these higher temperatures by limiting the stress, but the tradeoff is reduced work output and stroke. However, HTSMAs operating at decreased stresses can still be used effectively in actuator applications that require large strokes when used in the form of springs. The overall objective of this work is to facilitate the development of HTSMAs for use as high-force actuators in active/adaptive aerospace structures.

A modular test setup was assembled with the objective of acquiring stroke, stress, temperature and moment data in real time during joule heating and forced convective cooling of $Ni_{19.5}Ti_{50.5}Pd_{25}Pt_5$ HTSMA springs. The spring actuators were evaluated under both monotonic axial loading and thermomechanical cycling. The role of rotational constraints (i.e., by restricting rotation or allowing for free rotation at the ends of the springs) on stroke performance was also assessed. Recognizing that evolution in the material microstructure results in changes in geometry and vice versa in HTSMA springs, the objective of the present study also included assessing the contributions from the material microstructural evolution, by eliminating contributions from changes in geometry, to overall HTSMA spring performance. The finite element method (FEM) was used to support the analytical analyses and provided further insight into the behavior and heterogeneous stress states that exist in these spring actuators.

Furthermore, with the goal of improving dimensional stability there is a need to better understand the microstructural evolution in HTSMAs that contributes to irrecoverable strains. Towards this goal, available $Ni_{29.5}Ti_{50.5}Pd_{20}$ neutron diffraction data (from a comparable HTMSA alloy without the solid solution strengthening offered by the Pt addition) were analyzed. The data was obtained from *in situ* neutron diffraction experiments performed on $Ni_{29.5}Ti_{50.5}Pd_{20}$ during compressive loading while heating/cooling, using the Spectrometer for Materials Research at Temperature and Stress (SMARTS) at Los Alamos National Laboratory. Specifically, in this work emphasis was placed on neutron diffraction data analysis via Rietveld refinement and capturing the texture evolution through inverse pole figures. Such analyses provided quantitative information on the evolution of lattice strain, phase volume fraction (including retained martensite that exists above the austenite finish temperature) and texture (martensite variant reorientation and detwinning) under temperature and stress.

Financial support for this work from NASA's Fundamental Aeronautics Program Supersonics Project (NNX08AB51A), Subsonic Fixed Wing Program (NNX11AI57A) and the Florida Center for Advanced Aero-Propulsion (FCAAP) is gratefully acknowledged. It benefited additionally from the use of the Lujan Neutron Scattering Center at Los Alamos National Laboratory, which is funded by the Office of Basic Energy Sciences (Department of Energy) and is operated by Los Alamos National Security LLC under DOE Contract DE-AC52-06NA25396.

ACKNOWLEDGMENTS

First and foremost, I would like to express my sincere gratitude to my advisor Dr. Raj Vaidyanathan for making my graduate research experience possible. His advice and guidance throughout this experience was instrumental in making me the person I am today. My gratitude also goes out to Dr. Ruey Chen and Dr. Ranganathan Kumar for their contribution to this thesis by serving on my committee.

I would like to thank collaborators from NASA Glenn Research Center (GRC), Dr. Ron Noebe and Dr. Santo Padula for their valuable advice and contributions. I would also like to express gratitude to collaborators at Los Alamos National Laboratory (LANL), Dr. Don Brown, Dr. Bjørn Clausen and Thomas Sisneros for their valuable knowledge and experimental help. My thanks also goes out to my friends and colleagues in Dr. Raj Vaidyanathan's Group, Othmane Benafan, Dr. Shipeng Qiu, Dr. Mahadevan Manjeri and Mathew Fox for passing down to me valuable shape memory alloy and neutron diffraction knowledge. I would all also like to thank the Advanced Materials Processing and Analysis Center (AMPAC) administrative staff, Cynthia Harle and Angelina Feliciano, for helping to arrange travel to conferences, LANL and NASA GRC. I would like to acknowledge Jian Liu and Albert Mak of Dr. Chenyging Xu's group at the University of Central Florida for contributing knowledge in developing data acquisition systems.

Finally and above all I would like to thank my parents, family and friends for, their love and support, always being there for me and their encouragement to make it through this important step in my life.

TABLE OF CONTENTS

LIST OF FIGURES

LIST OF TABLES

LIST OF ACRONYMS/SYMBOLS

A_f	Austenite finish
A_s	Austenite start
FEM	Finite element method
GRC	Glenn Research Center
GSAS	General Structure Analysis System
HTSMA	High temperature shape memory alloy
IPF	Inverse pole figure
LANL	Los Alamos National Laboratory
M_f	Martensite finish
M_s	Martensite start
MRD	Multiples of random distribution
NiTi	Nickel-Titanium (alloy)
NiTiPd	Nickel-Titanium Palladium (alloy)
SMA	Shape memory alloy
SMARTS	Spectrometer for Materials Research at Temperature and Stress
UCT	Upper cycle temperature

CHAPTER ONE: INTRODUCTION

1.1 Motivation

During the last few decades there has been growing demand for smart/active structures in the aeronautic and aerospace industries as a means for improving aircraft performance and decreasing environmental impact [1]. In 2009 the American Institute of Aeronautics and Astronautics (AIAA) Emerging Technologies Committee released a list naming the top ten emerging aerospace technologies [2], encompassing the following:

1. ***"Greener Aviation" Technologies*** *- including emission reduction and noise reduction technologies as used in the Federal Aviation Administration's Continuous Low Emissions, Energy and Noise (CLEEN) program, and the European Environmentally Friendly Engine (EFE) program and "Clean Sky" Joint Technology Initiative.*

2. ***Alternative Fuels*** *- including biofuels, as promoted by the FAA's Commercial Aviation Alternative Fuels Initiative (CAAFI), and the recent FAA grant to the X Prize Foundation to spur development of renewable aviation fuels and technologies.*

3. ***High Speed Flight Technologies*** *- such as supersonic and hypersonic aerodynamics, sonic boom reduction technology, and thermal management aids.*

4. ***Efficient Propulsion Technologies*** *- including open rotors and geared turbofans, such as those used in the European DREAM (valiDation Radical Engine Architecture systeMs) program.*

5. ***Active Flow Technologies*** *- such as plasma actuators.*

6. ***Advanced Materials*** *- such as nanotechnology and composites.*

7. ***Active Structures*** *- such as shape memory alloys, morphing, and flapping.*

8. ***Health Management*** *- such as monitoring, prognostics, and self-healing.*

9. ***Remote Sensing Technologies*** *- including unmanned aerial vehicles and satellites such as those used in NASA's Global Earth Observation System of Systems (GEOSS) program.*

10. ***Advanced Space Propulsion Technologies*** *- including plasma-based propulsion such as the Variable Specific Impulse Magnetoplasma Rocket, and solar sail technologies.*

Active structures are included on the list at number seven and additionally benefits in "greener aviation" (number one on the list) can be obtained from such active structures. Operating conditions change throughout various stages of flight, including take-off, cruising and landing. Such active structures enable morphing of several aircraft components, thus, optimizing performance for various stages of flight and operating conditions. Aircraft performance can gain efficiency from active flow control of wings (i.e., flaps, winglets, trailing edges, etc.), aeronautical gas turbines (i.e., variable area inlets, chevrons, etc.) and reconfigurable rotary blades, among others. Increases in efficiency and benefits to the aircraft performance include reduced operating cost, increased range or payload, and reduced noise [3]. Applications utilizing active structures driven by conventional hydraulic and electric actuators are limited by weight, the requirement of associated devices and components, and price. Solutions to overcome these limitations include the use of smart materials such as shape memory alloys (SMAs) to create "state-of-the-art" actuation systems.

SMAs have the ability to recover their shape (up to 8% inelastic strain) against external loads (up to 500 MPa of stress) as a result of a thermally induced solid-state phase transformation. This ability to do work while transforming from one phase to another enables their use as high-force actuators with both sensory and actuation functions [4-11]. SMAs have the following advantages when compared to conventional actuators. SMAs have increased work output per unit mass. Being a thermally-induced phase transformation SMA actuation can be controlled by heat transfer or resistive heating as compared to more complex controllers in electromagnetic systems or hydraulic fluid. This eliminates the potential for leaks, sparks and moving parts typically associated with hydraulic and electric actuators, thus increasing safety and reliability, while reducing the need for maintenance. Other advantages include the ability to operate in unique forms (e.g., beams and flexures) and in more compact spaces.

Examples of the use of SMAs for active aeronautical structures include the following. The variable geometry chevron (VGC) was implemented by Boeing to optimize noise mitigation during take-off and landing [1, 6, 12]. The Smart Aircraft and Marine Project System Demonstration (SAMPSON) smart inlet program, funded by DARPA, was used to demonstrate a smart structure inlet on a full scale F-15 [13, 14]. The reconfigurable rotor blade program, funded by NAVIAR, was used to optimize blade twist during cruise and hovering flight conditions [1, 15]. SMA actuation is not limited to active structures for noise and flow control. SMA actuated spark-free release mechanisms have been used for stage separation and satellite deployment [16]. NiTiFe SMA has been utilized as a sensor and actuator to passively control heat pipe based thermal switches that can potentially be used for thermal management on the lunar or Martian surface [7].

Currently, commercial success and availability of SMAs has been mostly limited to binary NiTi and ternary NiTiCu with transformation temperatures approximately in the -100 ºC to 100 ºC range. It is difficult or impossible to control actuation of the SMA in environments in which the ambient temperature exceeds the limits of the SMA’s transformation temperatures. On the lunar surface temperatures can vary between 40 K and 400 K with the day/night cycle. In aeronautical gas turbines temperatures can vary depending on sectional location (i.e., fan, compression, combustion, turbine, exhaust, bypass, etc.) between ambient to in excess of 1300 K. Towards the goal of facilitating use of SMAs for actuation in such environments, there is a need to develop high-temperature SMAs (HTSMAs) with increased operating temperatures.

In an ongoing effort at NASA Glenn Research Center (GRC) to develop HTSMAs, ternary and quaternary additions are being made to binary NiTi to form NiTi-X (e.g., X: Pd, Pt, Au and Hf) alloys with transformation temperatures above 100 ºC [17-25]. One such alloy that has been studied is $Ni_{19.5}Ti_{50.5}Pd_{30}$ [18, 20, 21, 24, 25], which exhibits a B2 (cubic austenite) to B19 (orthorhombic martensite) phase transformation, has relatively high transformation temperatures (on the order of 250 °C) and superior work capabilities (i.e., ~9 J/cm^3 at 393 MPa). However, this alloy experiences increasing irrecoverable strains during thermal cycling under increased stress or upper cycle temperature (UCT) [18, 21, 24], approaching ~0.5% irrecoverable strain per cycle at 393 MPa. Hence, the alloy was modified by solid-solution strengthening, substituting 5 at.% Pt for Pd to form a $Ni_{19.5}Ti_{50.5}Pd_{25}Pt_5$ alloy. This solid-solution strengthened quaternary alloy exhibits greater dimensional stability without a significant loss of work output and achieves an additional margin of safety in terms of increased UCT capability [21, 26]. In addition, it was shown that this enhanced dimensional stability could be improved even further through appropriate training processes [21].

Stability and repeatability can be further increased at these higher temperatures by limiting the stress (<0.1% open loop strain at 100MPa for $Ni_{19.5}Ti_{50.5}Pd_{25}Pt_5$) [21], but the tradeoff is reduced work output and stroke. However, HTSMAs operating at decreased stresses can still be used effectively in actuator applications that require large strokes when used in the form of springs. Springs are also advantageous when compared to wires because of the ability to work in tension and/or compression and the potential for increased heat transfer (achieved e.g., by forced convective cooling over compact areas or creating springs from tubes [27]). Thus there is value in evaluating the thermomechanical behavior of $Ni_{19.5}Ti_{50.5}Pd_{25}Pt_5$ HTSMA springs.

In previous work, $Ni_{19.5}Ti_{50.5}Pd_{25}Pt_5$ springs of various geometries were assessed for the effects of thermomechanical history on performance (i.e., work output, stability and monotonic response) [28, 29]. It was recognized that irrecoverable strain caused unrecovered axial deformation or an increase in the spring's free length with each thermomechanical cycle, which could not be recovered upon heating; however training could be used to significantly reduce or eliminate this effect. In this case, the cause of the irrecoverable strain was not identified but was attributed to microstructural evolution, including, martensite variant reorientation, detwinning, the buildup of retained martensite or plasticity. Training was used to stabilize the microstructure and thus the response of the springs. However, the performance of the trained springs was assessed without taking into consideration the effect of unrecovered axial deformation on the spring geometry.

The overall objective of this work is to facilitate the development of HTSMAs for use as high-force actuators in active/adaptive structures. Realizing that material evolution generates geometry change and vice versa in $Ni_{19.5}Ti_{50.5}Pd_{25}Pt_5$ springs, more specifically the first objective of the present study was to assess the contributions of microstructural evolution, by eliminating the contributions of geometry change, to overall $Ni_{19.5}Ti_{50.5}Pd_{25}Pt_5$ spring performance. This was done by adapting a previously established methodology for the mechanical analyses of springs [30], which is typically limited to linear elastic springs, but is used in this study after providing basis for its use. This spring analyses methodology was also used to provide insight into the heterogeneous multi-axial stress states of the springs. Finally, the role of grip constraints was systematically investigated by allowing the springs to freely rotate or fixing the ends during actuation. The moment produced at the ends of the springs (caused by axial loading and/or thermomechanical cycling) was measured and compared to theory. The finite element method (FEM) was used to support the analytical analyses and provided further insight into the behavior and heterogeneous stress states that exist in SMA spring actuators.

Secondly, the objective is to improve the understanding of the contributions of microstructural evolution to recoverable and irrecoverable strains with the goal of improving dimensional stability. Towards this goal, available $Ni_{29.5}Ti_{50.5}Pd_{20}$ neutron diffraction data (from a comparable HTMSA alloy without the solid solution strengthening offered by the Pt addition), from Ref. [31], was analyzed. This data included *in situ* neutron diffraction experiments performed on $Ni_{29.5}Ti_{50.5}Pd_{20}$ HTSMA during compressive loading while heating/cooling, using Spectrometer for Materials Research at Temperature and Stress (SMARTS) at Los Alamos National Laboratory (LANL). Specifically, in this work emphasizes was placed on neutron diffraction data analysis via Rieveld refinement. Such analysis provided quantitative information on the evolution of lattice strain, phase volume fraction and texture under various temperatures and stress.

1.2 Organization

The work presented in this thesis is divided into chapters organized as follows: Chapter 2 provides a review of SMAs with an emphasis on aerospace applications. Chapter 3 describes the experimental design and procedures for testing $Ni_{19.5}Ti_{50.5}Pd_{25}Pt_5$ springs, and also, briefly summarizes the *in situ* neutron diffraction setup procedures adopted for acquiring the available $Ni_{29.5}Ti_{50.5}Pd_{20}$ data, from Ref. [31], at SMARTS. Chapter 4 gives a complete step-by-step description of $Ni_{29.5}Ti_{50.5}Pd_{20}$ neutron diffraction data analysis performed via General Structure Analysis System (GSAS) software. Chapter 5 presents the results and analysis of the experiments performed on $Ni_{19.5}Ti_{50.5}Pd_{25}Pt_5$ springs and provides a discussion of the spring's thermomechanical behavior. Chapter 6 uses the finite element method to support the analytical analyses and provide further insight into the behavior and heterogeneous stress states of the tested $Ni_{19.5}Ti_{50.5}Pd_{25}Pt_5$ spring actuators. Chapter 7 presents the results and discussion of the neutron diffraction experiments at SMARTS and data analysis carried out on $Ni_{29.5}Ti_{50.5}Pd_{20}$. Discussion on the contributions of microstructural evolution to recoverable and irrecoverable strains is provided. Chapter 8 presents conclusions of the present study and recommendations for future work.

CHAPTER TWO: LITERATURE REVIEW

From the time of the discovery of shape memory behavior in 1951 [32], SMAs have been extensively researched to better understand their functional properties. Much of this research has been focused on facilitating SMA use in the medical, automotive and aerospace industries. This chapter provides an introduction and review of SMAs and their ability to be used as actuators. Emphasis is place on SMA spring actuators as means of increasing the actuator stroke. The chapter concludes with the current developments of SMAs in aerospace applications.

2.1 Shape memory alloys

SMAs have the ability to recover their shape by going through a thermal or stress induced solid-state phase transformation. This phase transformation occurs between a high-symmetry austenite phase and a low-symmetry martensite phase. Typically in NiTi based SMAs, the austenite phase holds a cubic (B2) structure that is associated with high temperatures, while the martensite holds a monoclinic (B19′) structure that is associated with low temperature. The ability of SMAs to recover up to 8% inelastic strain against external loads in excess of 500 MPa of stress while transforming from one phase to another enables their use as high work output actuators with both sensory and actuation functions.

SMAs exhibit either a stress or temperature induced solid-state phase transformation. The thermally induced phase transformation is known as the shape memory effect (SME). This nomenclature arose because the SMA is deformed in its martensite phase and recovers it shape upon heating to austenite. During the stress induced transformation (often referred to as superelasticity), load is applied to the SMA in its austenite phase and stress induced martensite

(SIM) forms. Upon removing the load, the SIM transforms back to austenite and the strain recovers without plastic deformation.

2.1.1 Shape memory effect

The SME refers the SMAs ability to recover or “remember” its shape. Figure 2.1 shows a simplified illustration of the shape recovery process that results from the SME. During this process, first, the SMA cools and austenite transforms into self-accommodated or twinned martensite (A to B). After cooling, stress is applied and deformation occurs as a result of reorientation and detwinning of martensite variants (B to C). After relieving the stress, the SMA maintains is deformed shape with the exception of elastic recovery in the martensite (C to D). Note, the stress could be held constant between B and C and the shape recovery could occur against load and work would be produced. This is typical SMA actuation and is described in detail in the next section.

Upon heating, the detwinned martensite transforms back to austenite and the original shape is recovered (D to A). The transformation temperatures associated with the SME are defined as follows. The forward transformation begins during cooling in which austenite begins to transform to martensite, this is known as the austenite start, A_s,temperature. The forward transformation is complete when all martensite has transformed to austenite, this is known as austenite finish, A_f, temperature. This process is reversible and completed by heating. The temperature at which austenite begins to transform back to martensite is known as the martensite start, M_s, temperature. Finally, when the process is complete when all of the austenite is transformed back to martensite, this is known as the martensite finish, M_f, temperature. Note, these transformation temperatures vary with the applied stress according to the Clausius-

Clapeyron relationship [33, 34]. Stoichiometry, processing and thermomechanical history will also greatly affect the transformation temperatures [4]. There is a hysteresis associated with the transformation and is defined as the difference between M_s and A_s.

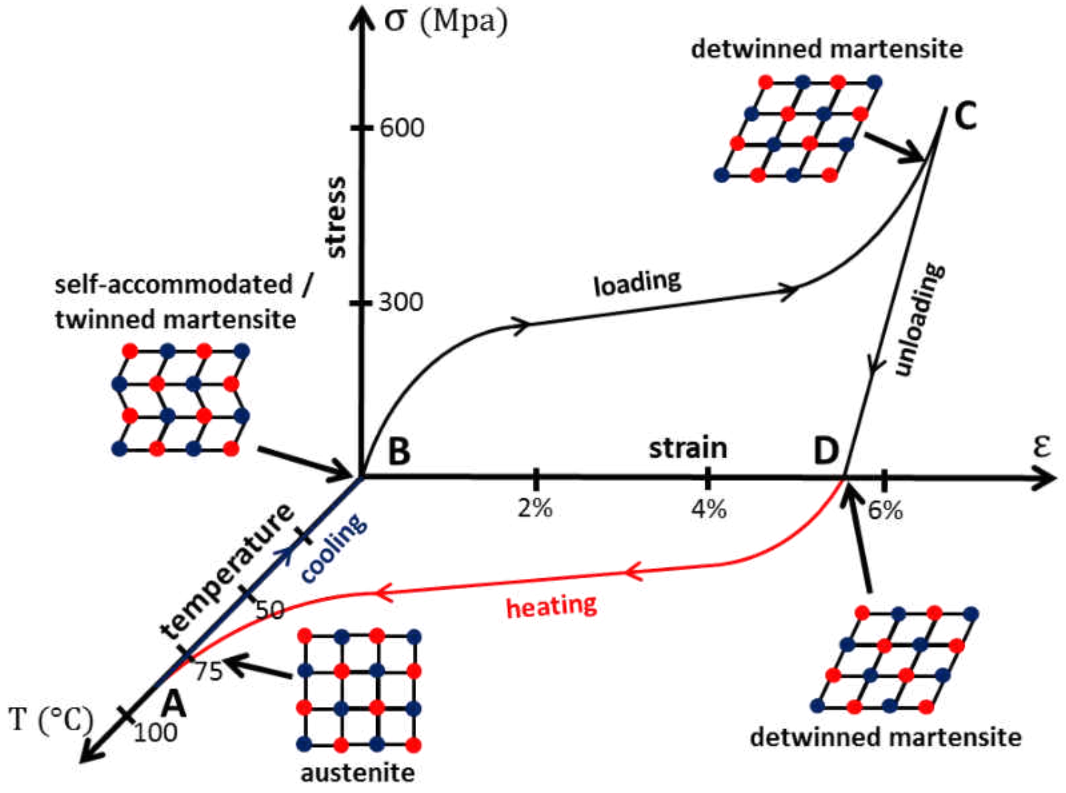

Figure 2.1: Shape memory effect shown in stress-strain-temperature space: (A to B) austenite transforms to self-accommodated martensite or twinned marteniste when cooled; (B to C) twinned martensite reorients and detwins during loading; (C to D) martensite remains detwinned as unloading occurs (thus the system is deformed macroscopically); and (D to A) martensite transforms to austenite and the system recovers the deformation.

The SME can occur in two different ways i.e., one-way (OW) or two-way (TW)SME. OWSME results from applying an external bias load (i.e., load biased actuation) as illustrated in Figure 2.1. TWSME refers to the ability of SMAs to transform between the deformed and unreformed shape with no external load applied.

2.1.2 Superelasticity

Superelasticity refers to the stress induced solid-state phase transformation associated with SMAs. Figure 2.2 shows a simplified illustration of superelasticity during loading and unloading at constant temperature. During this process, stress is applied to the SMA above the A_f. First, austenite shows linear elastic behavior. As stress increases austenite transforms into stress induced martensite (SIM) (A to B). The formation of SIM can be observed as the increased compliance of the stress-strain response in Figure 2.2 (region of decreased slope in the loading curve). Once all the austenite has transformed, elasticity in the SIM can be observed.

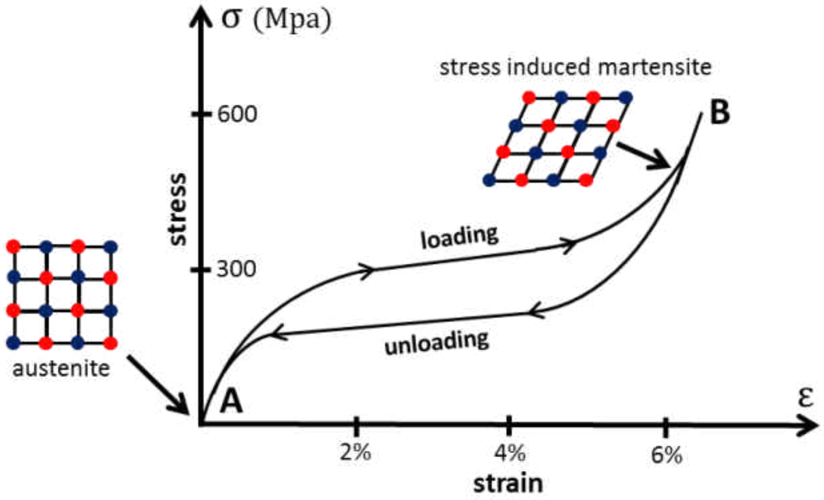

Figure 2.2: Superelastic behavior shown in stress-strain space above the austenite finish temperature: (A to B) loading causes the stress induced phase transformation from austenite to stress-induced martensite; and (B to A) unloading causes the reverse transformation back to austenite.

Conversely, this behavior is observed in the unloading curve. During unloading the SIM transforms back to austenite (B to A) and the strain is fully recovered. Hysteresis associated with the transformation is observed in Figure 2.2 as the difference between the upper (loading) and lower (unloading) curves.

2.2 Shape memory alloy actuators

The ability to do work while transforming from one phase to another enables SMAs to be used as high-force actuators with both sensory and actuation functions [4-8]. When compared to conventional hydraulic or electric actuators, SMA actuators have the potential for increased worked output per unit weight (i.e., efficiency) and the ability to operate in more compact spaces. Furthermore, having no moving parts SMA actuators provide quieter and more reliable operation. Figure 2.3 shows a force output (N) versus weigh (g) comparison for SMA wire, coil spring and strip actuators with other types of thermal actuators and magnetic solenoids. All three SMA actuator forms presented (i.e., wires, springs and strips) demonstrate increased force output per unit weight when compared to magnetic solenoid actuators. The most commonly used form of SMA actuator is the straight wire due to its increased efficiency, commercial availability and simplicity. SMA wires have the highest force output per unit weight out when compared to SMA springs and strips. However, SMA wire actuators have limited stroke. SMA wires can be formed into spring actuators in applications that require increased stroke. In applications, both forms are often heated through the phase transformation by Joule heating by a controlled electric current and are finally, convectively cooled to complete the SME cycle.

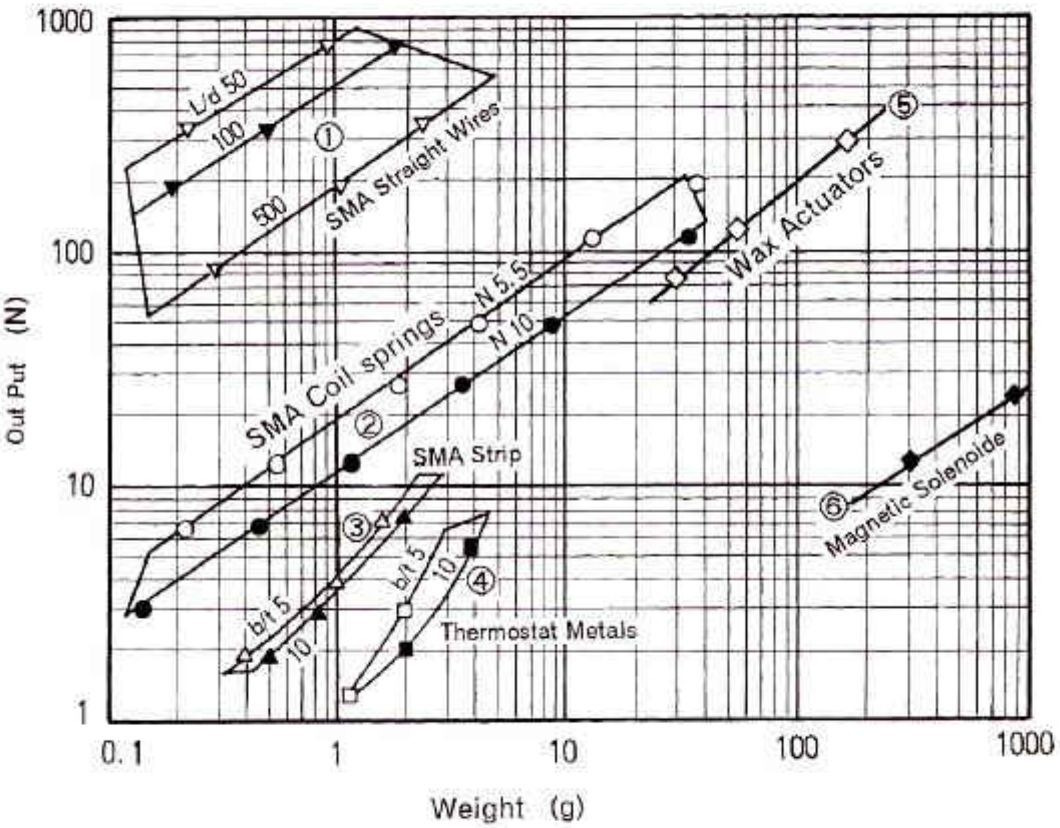

Figure 2.3: Force output (N) versus weigh (g) comparison for SMA wire, coil spring and strip actuators with other types of thermal actuators and magnetic solenoids [4].

The OWSME frequently finds use as the mechanism for SMA actuation. The OWSME is carried out under constant stress/load and can be considered as load-bias recovery during a thermal cycle. Figure 2.4 shows an example of a deflection/strain-temperature response from a load-bias experiment. Here, transformation temperatures under constant load can be determined by fitting tangent lines through the three distinct linear regions on both the cooling and heating curves, and then extrapolating to determine the points of intersection [33].

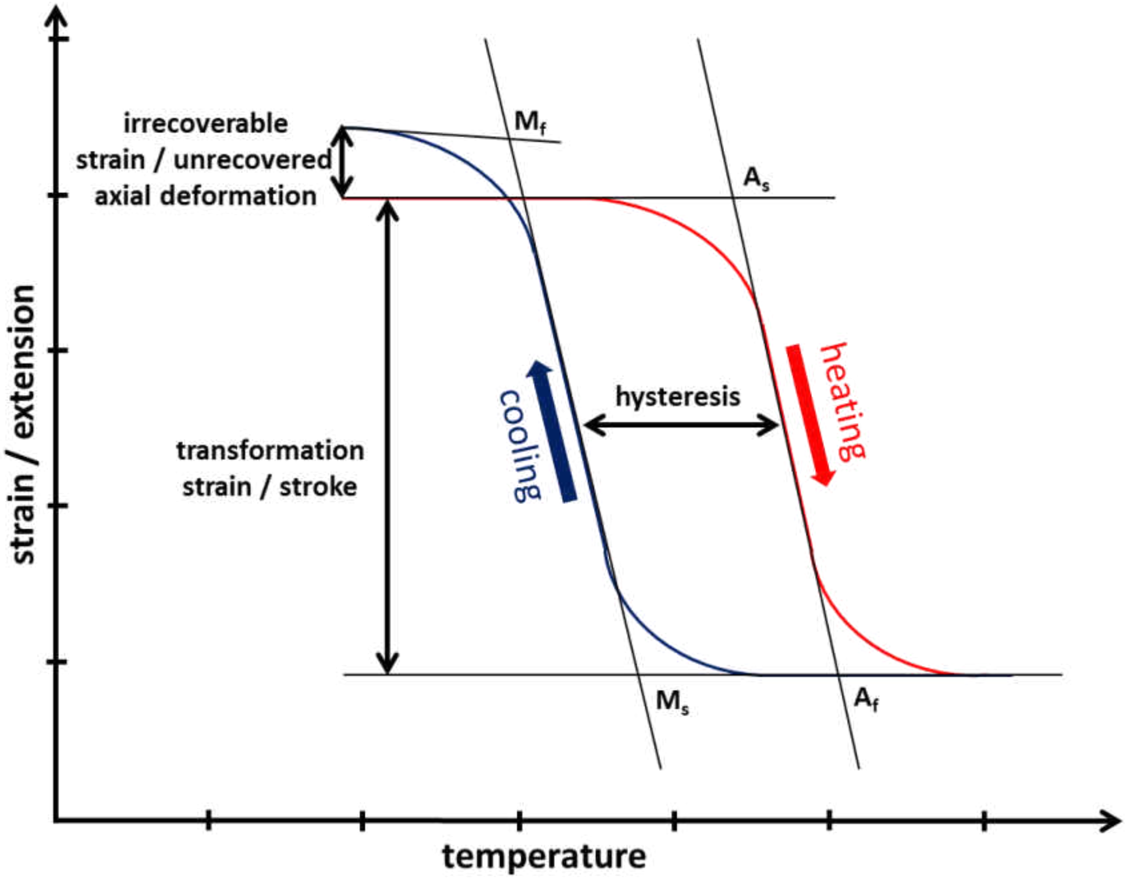

Figure 2.4: A shape memory thermal cycle under constant load (i.e., load-bias actuation) with transformation temperatures determined via the intercept method. Also, associated terminology is defined for SMA actuators, respectively.

Also shown is the transformation strain or the strain recovered during the thermal cycle and irrecoverable strain or strain which is lost or not recovered during the thermal cycle. Note that when used in this context, the irrecoverable strain sometimes assumes the name open-loop strain as it may recover by additional processing (e.g., thermal cycling under a reduced load) [33]. Strain, transformation strain and irrecoverable strain become extension, stroke and unrecovered axial deformation, respectively, when used in reference specifically to SMA spring actuators.

2.3 Shape memory alloy springs

Transformation strains in SMAs can be limited in cases where transformation involves the trigonal R-phase (e.g., in NiTiFe alloys [7]) or in cases where desired stability and repeatability at elevated temperatures occur (e.g., NiTiPdPt alloys [28, 29]). Stability and repeatability can be increased at these higher temperatures by limiting the stress, but the tradeoff is reduced work output and stroke. However, SMAs operating at limited strains and decreased stresses still find effective use in actuator applications that require large strokes when used in the form of springs. Springs are also advantageous when compared to wires because of the ability to work in tension or compression, and their potential for increased heat transfer (achieved e.g., by forced convective cooling over compact areas or creating springs from tubes [27]). Thus there is a need to understand the thermomechanical performance of SMA helical actuators with the objective of obtaining guidelines for their design, fabrication and use.

2.1.1 Shape memory alloy spring design methodology

Waram first outlined the currently used SMA helical spring design and analyses methodology in 1990 [35] and in 1998 Ohkata and Suzuki reviewed it again in Ref. [4]. This SMA spring methodology adapts conventional spring design (see ref. [4, 28, 36] for formulae and notation). Limitations in the aforementioned methodologies ability to predict SMA spring performance was realized when applied to HTSMA $Ni_{19.5}Ti_{50.5}Pd_{25}Pt_{5}$ springs [28, 29]. The inability to properly capture spring deflection was attributed to microstructural evolution. Microstructural evolution includes martensite variant reorientation, detwinning, the buildup of retained martensite and possibly even plasticity. Also, error arises from TWSME which is not accounted for but contributes to the stroke.

In previous work, various spring design methodologies underwent comparisons when applied to the design of NiTiFe low temperature SMA springs [7]. These spring design methodologies included Wahl [37], Ancker and Goodier [30], and the FEM. From this comparison came the realization that conventional spring methodology fails to accurately capture the response of the spring. However, Ancker and Goodier spring theory and FEM with limited assumptions (elastic and isotropic material properties and small deflection) were consistent with the experimental NiTiFe spring response, under the conditions investigated. Also, heterogeneous multi-axial stress states inherent to springs were realized using Ancker and Goodier spring design methodology and the FEM.

By removing the inactive center (not contributing to stroke) of the SMA spring wire, increases in efficiency can be achieved. Thus, Dragoni designed SMA springs to be constructed from tubes in order to reduce weight and increase heat transfer during actuation [27]. This spring design theory, based on Ref. [37], was developed to create hollow cross-section springs with optimal thermal and mechanical efficiency.

2.1.2 Training and characterization of NiTi based springs

$Ni_{19.5}Ti_{50.5}Pd_{25}Pt_5$ springs of various geometries were assessed for the effects of thermomechanical history on performance [28, 29]. Thermomechanical history performed on these springs focused on training until stability was obtained. Training was performed under various loading conditions. The results showed that training at increased loads achieved stability faster; however training at such increased load decreased the work output of the trained actuator. In addition to training, the springs were assessed for work output capabilities. These results showed a linear relationship between work output and the cross-sectional area of the wire investigated. Furthermore, a decreasing *D/d* ratio, while holding *d* constant produced a more efficient actuator. It also showed a linear relationship between work output and number of active coils.

Recently, NiTi and NiTiCu springs were evaluated for the effects of alloy composition and cold work on thermal and cyclic stability [38, 39]. The results showed that cold working decreases the work output, but increases stability. Adding Cu to NiTi and training for several hundred cycles improved both cyclic and thermal stability. Both Stebner and Grossman [38, 39] concluded that microstructure evolution, including, martensite variant reorientation, detwinning, the buildup of retained martensite or plasticity was responsible for instability, while training stabilized this microstructural evolution.

2.4 Aerospace applications of shape memory alloys

Since their discovery, SMAs have had great potential for use in aerospace applications. In the late 1960s, Raychem marketed the first industrial SMA application with an SMA hydraulic tube couple which was used in F-14 fighter aircraft [40]. Since then, the development of SMA with increased dimensional stability and an increased transformation temperature range has accelerated their implementation into application. In 2003, the Cosmic Hot Interstellar Plasma Spectrometer CHIPs observatory was launched. SMA springs were chosen here primarily because of their large stroke with adequate force, to actuate a one-time release mechanism for the detector vacuum chamber door [16]. Two NiTi springs were used. One spring functioned as the primary actuator and the second was a fail-safe actuator. The fail-safe spring actuator was never used as the primary spring actuator functioned properly.

Operating conditions change throughout various stages of flight, including take-off, cruising and landing. SMA actuated flow control can increase aircraft performance by optimizing the configuration of various components to these operating conditions. One such example includes the Smart Aircraft and Marine Project System Demonstration (SAMPSON) program, funded by DARPA, with the goal of demonstrating a smart structure inlet on a full scale F-15 aircraft [13, 14]. Figure 2.5 shows the SMA wire bundle (34 NiTi wires in Teflon tubes) used as the actuator in a cowl rotation actuations system, which deflects the lip of the smart inlet. Figure 2.6 shows a full scale F-15 smart inlet being tested in a transonic wind tunnel at NASA Langley. The lip deflected 23 deg in 30s under the maximum aeroloads for 0.8 mach flow [1, 13, 14].

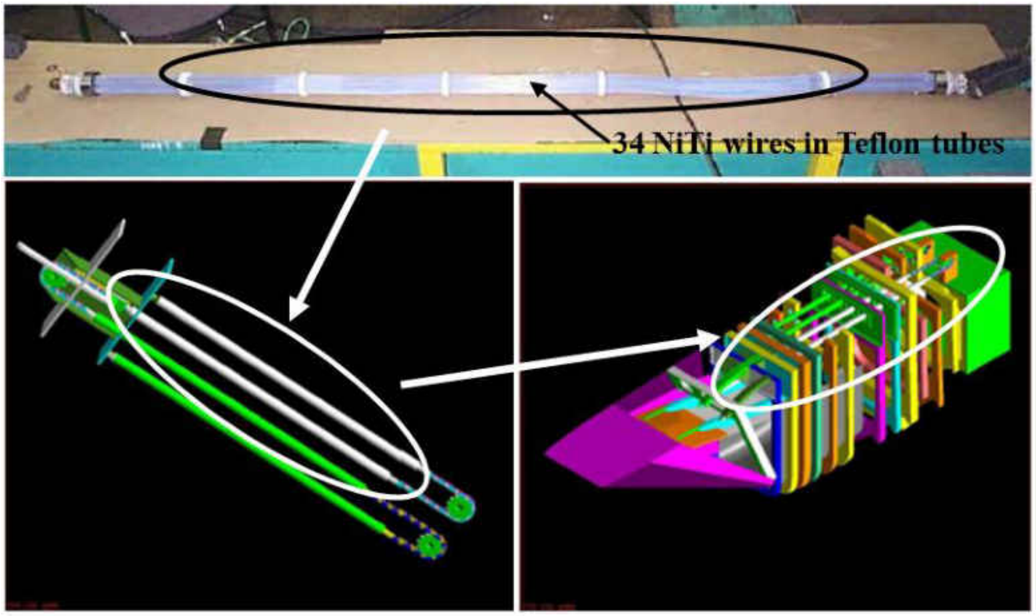

Figure 2.5: SAMPSON NiTi wire bundle actuator and cowl rotation actuation system [13].

Figure 2.6: SAMPSON smart inlet testing in 16 feet transonic wind tunnel at NASA Langley [13].

Another example is a Reconfigurable Rotor Blade (RRB) program, funded by NAVIAR, to optimize blade twist during cruise and hovering flight conditions [41]. Figure 2.7a shows the reconfigurable rotor blade assembly with NiTi tube actuators. In 2007, a 1/4 scale three blade hub assembly was wind tunnel tested. Figure 2.7b shows the RRB 1/4 scale rotor blade testing in the Boeing V/STOL wind tunnel. The SMA actuator produced more than 6.8 Nm of torque and 3.4 J of energy in the rotor environment and was subject to 250 twist cycles over 75 hours with no loss in performance.

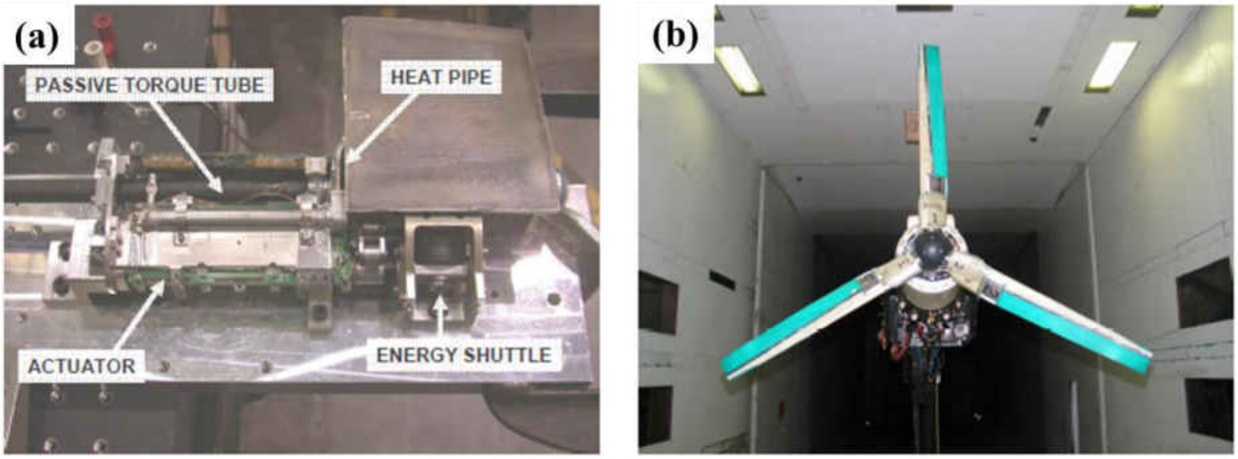

Figure 2.7: Reconfigurable Rotor Blade System (RRB) [41]: (a) reconfigurable rotor blade assembly with NiTi tube actuators; and (b) 1/4 scale rotor blade testing in the Boeing V/STOL wind tunnel.

The Variable Geometry Chevron (VGC) is an example of an active SMA aerostructure, in which noise mitigation is the primary goal. Figure 2.8 shows the VGC sleeve mounted on a GE90-115B engine for 777-300ER flight testing [1, 12]. Three Ni-40Ti (60% by weight Nickel) flexures were used to actuate each of 14 total chevrons. In addition to reducing noise the immersed chevrons will also increase drag and reduce engine thrust. Therefore, the chevrons were immersed only during take-off and landing to reduce noise and retracted for better performance during cruise.

Figure 2.8: Variable Geometry Chevron (VGC) sleeve mounted on GE90-115B engine for 777-300ER flight test [1].

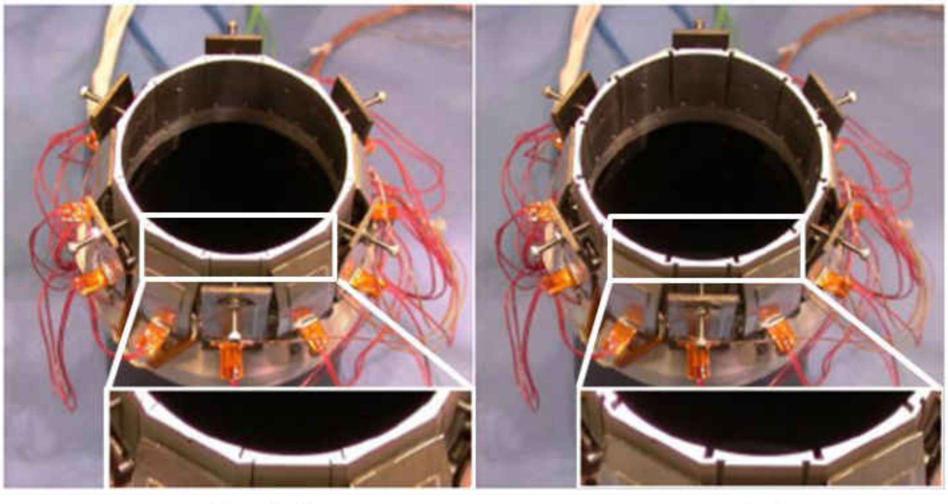

Figure 2.9: Scale model of a Variable Area Fan Nozzle (VAFN) while contracted and expanded 20% [15].

More recently, Boeing demonstrated a variable area fan nozzle (VAFN), in which the goal is to reduce noise and improve fuel consumption [1, 15]. Figure 2.9 shows a scale model of a VAFN while contracted and expanded with 20% area change. It consisted of interlocking panels which had Ni-40Ti flexure actuators attached to each panel. In 2008, as part of their environmental exhibit Boeing showed a VAFN display at the Farnborough Air Show. This display included the aft end of a full scale 777 size engine with a VAFN.

In October 2010, as part of the Continuous Lower Energy, Emissions and Noise (CLEEN) program Boeing set a goal of developing a full-scale flight test of adaptive trailing edges with validation on a 737-800. Figure 2.10 shows Boeings proof of concept of adaptive trailing edge technology. Objectives of the adaptive trailing edge program include reduction of noise and fuel consumption during various stages of flight.

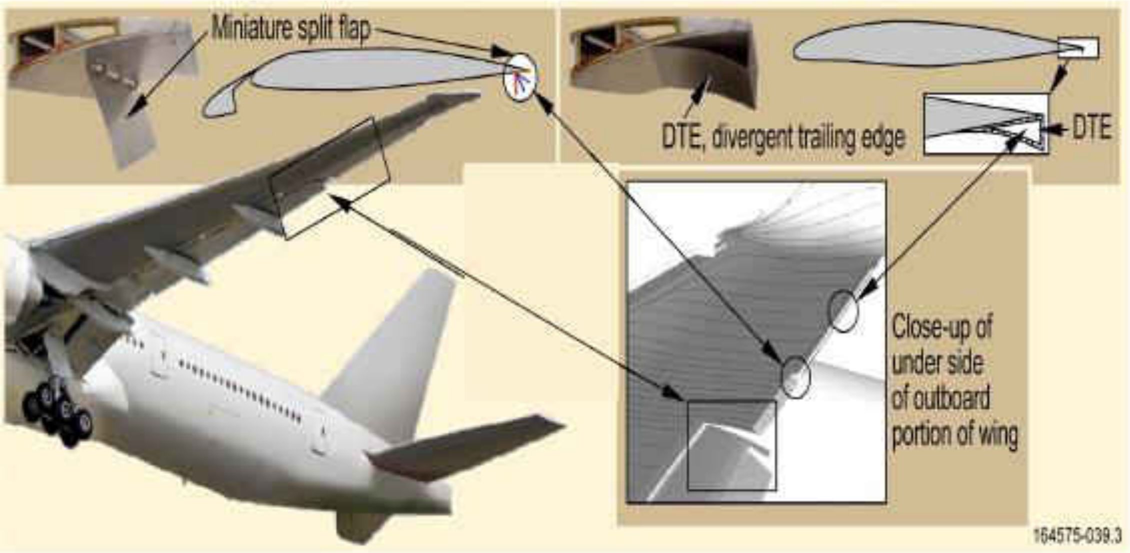

Figure 2.10: Boeings goal of adaptive trailing edge technology as part of the FAA's Continuous Lower Energy, Emissions and Noise (CLEEN) program.

Currently, the commercial availability and use of SMAs has been mostly limited to binary NiTi alloys with transformation temperatures approximately in the -100 to 100 º C range. Applications in the automotive and aerospace industry require transformation temperatures above 100 º C in order to avoid false actuation due the ambient temperatures of their environment. By increasing transformation temperatures, the frequency of actuation increases as the rate of convective cooling increases due to the larger temperature gradient between the SMA actuator and its environment. The development of HTSMAs has the potential to revolutionize the aerospace and power generation industries, among others. Figure 2.11 shows the identified opportunities for HTSMA actuators in a gas turbine [42].

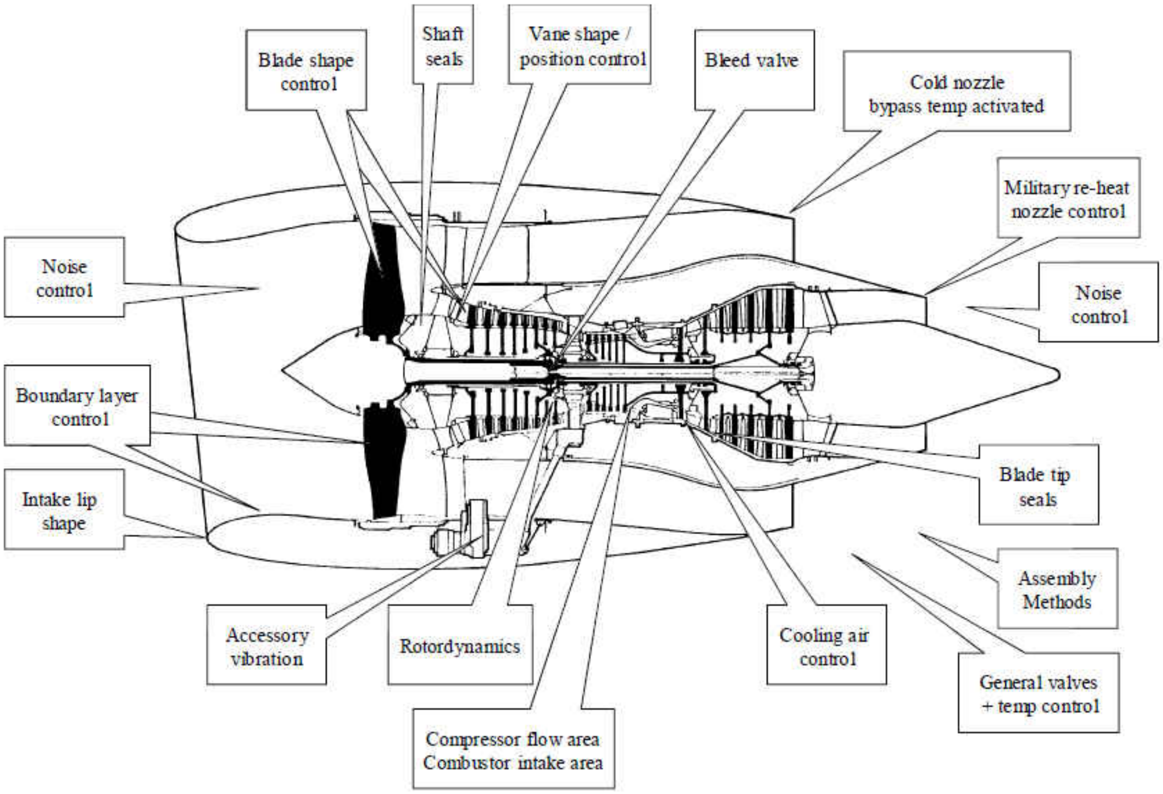

Figure 2.11: Identified opportunities for HTSMA actuators in a gas turbine [42].

CHAPTER THREE: EXPERIMENTAL AND COMPUTATIONAL PROCEDURES

3.1 Spring fabrication

The material used in this work was a quaternary $Ni_{19.5}Ti_{50.5}Pd_{25}Pt_5$ alloy (at %), produced by vacuum induction melting in a graphite crucible. The ingot was homogenized at 1050 °C for 72 hours and furnace cooled. The homogenized ingot was then hot extruded into rods at 900 °C with an area reduction ratio of 7:1. Wires with two different diameters were fabricated: the first was precision ground from the extruded rod to a diameter of 2.16 mm and the second was cold drawn to its final diameter of 0.5 mm. The precision ground wire was fabricated into a spring, *S1*, with a coil diameter of 23.1 mm, 3 active turns and a free length of 19 mm (Fig. 3.1a). The cold drawn wire was fabricated into a spring, *S2*, with a coil diameter of 12.5 mm, 10 active turns and free length of 23 mm (Fig. 3.1b).

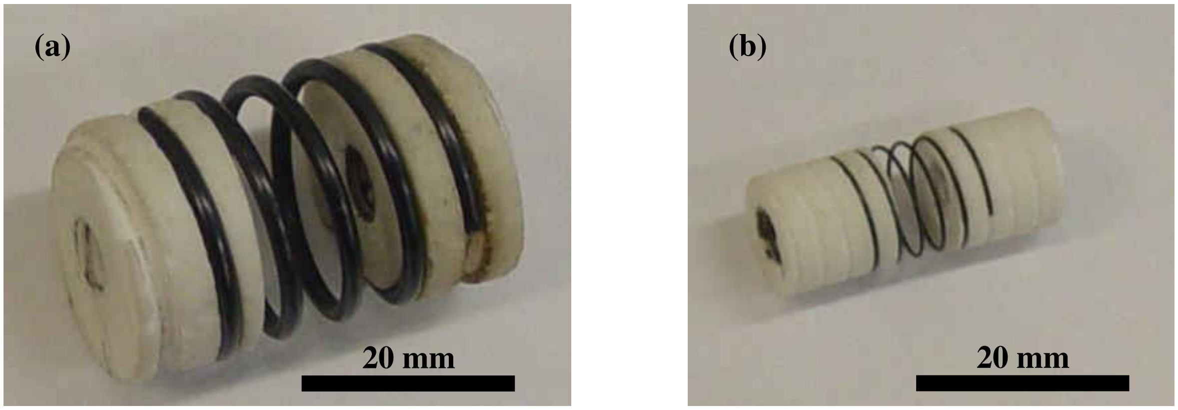

Figure 3.1: As-shape-set $Ni_{19.5}Ti_{50.5}Pd_{25}Pt_5$ high temperature shape memory alloy spring actuators shown with Macor® spring mounts: (a) spring *S1* (wire diameter d=2.16 mm and coil diameter D=23.1 mm); and (b) spring *S2* (wire diameter d=0.5 mm and coil diameter D=12.5 mm).

The wires were wound onto their respective mandrels at room temperature and sleeves were slid over the wire and mandrel to ensure the wires maintained their desired spring shape through the shape-setting process. Following Ref. [28], the springs were shape-set by heating at 515℃ for 45 min in air and then furnace cooled to room temperature.

3.2 Test setup

3.2.1 Thermomechanical test fixture

A test setup (Fig. 3.2) with the capability of testing HTSMAs springs of various geometries was designed and assembled. The setup consisted of an optical table and aluminum brackets for configurational flexibility. The center of one bracket was fitted with linear bearings. An 8 mm diameter rod machined true center and with a spline was used as the actuator shaft through the brackets. A simple pulley system with a load (not shown) was used to apply the bias force on the HTSMA actuator. A MTS Temposonic® G-series magnetostrictive position sensor was used to acquire data on the length of the spring (Fig. 3.3). The actuator was joule heated with a Mastech HY3030E DC power supply (900W) (Fig. 3.2) and cooled by forced convection with a fan. The power supply was run at constant current, and the current to the spring was turned on and off with a solid-state relay (Fig. 3.2) triggered by a control signal from the system described in the following section (Fig. 3.4). The spring mounts (Fig. 3.1) were machined from Macor® with an outside helical channel for the spring and an inside thread for the actuator shaft. This glass-ceramic material was specifically chosen for its low thermal conductivity in order to reduce conductive heat losses during thermal cycling. One spring mount was coupled to one of two torque cells (one shown, Fig. 3.3), to measure the torque produced, during actuation, when the spring was constrained from rotating.

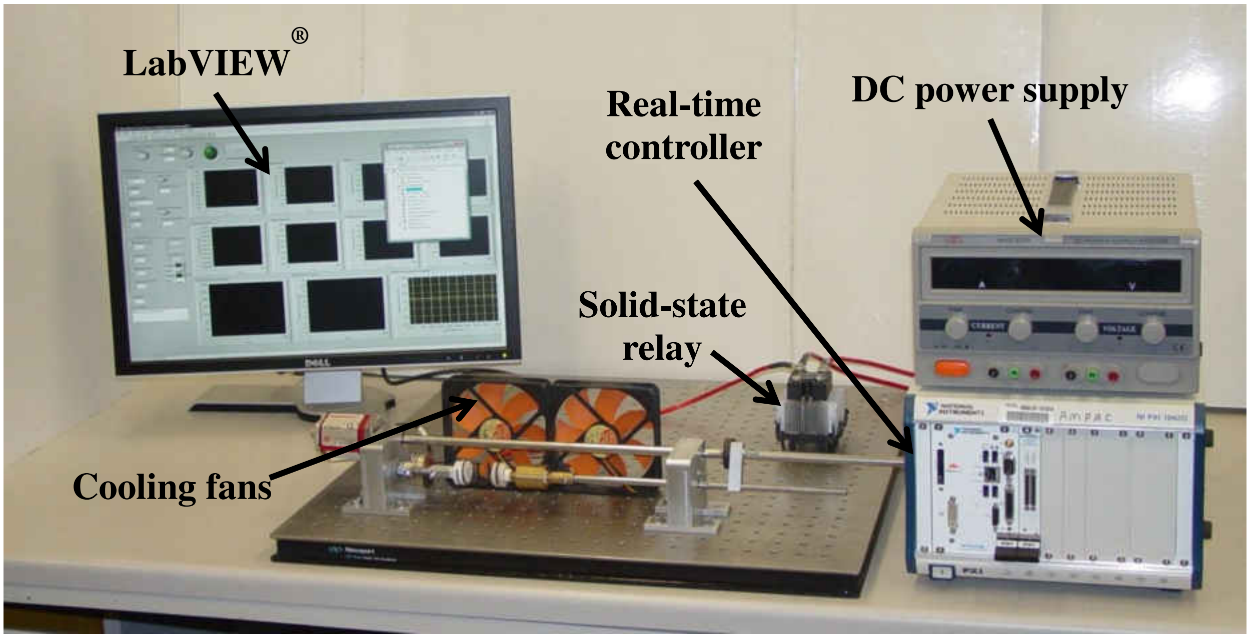

Figure 3.2: Overview of setup for testing of $Ni_{19.5}Ti_{50.5}Pd_{25}Pt_5$ high temperature shape memory alloy spring actuators.

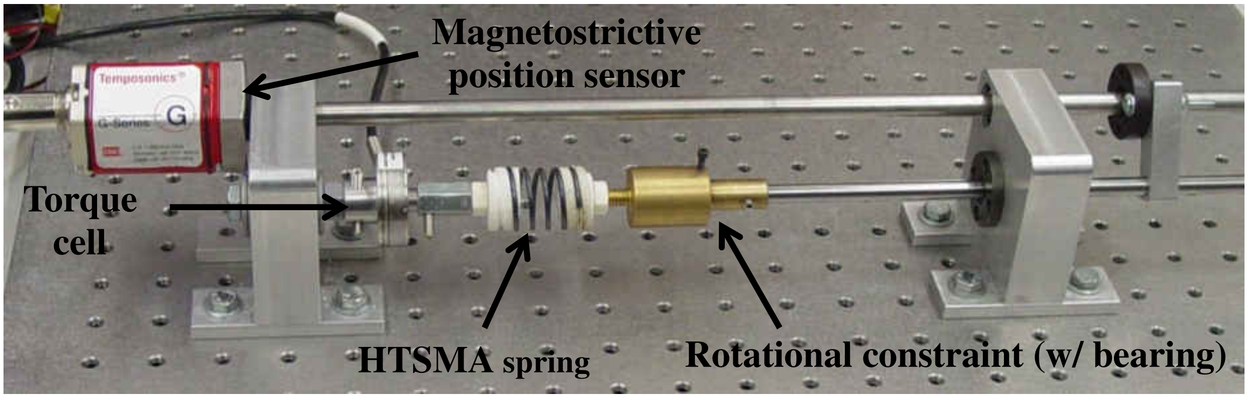

Figure 3.3: Mechanical components and sensors of setup for testing of $Ni_{19.5}Ti_{50.5}Pd_{25}Pt_5$ high temperature shape memory alloy spring actuators.

One torque cell with a 0-176.5 N·mm range for isothermal loading and the other with a larger 0-706.2 N·mm range for acquiring larger moments produced during isobaric thermal cycling. A ceramic rotary bearing was coupled between the actuator shaft and one of the spring mounts, with set screws positioned to add or relieve rotational constraint as desired (Fig. 3.3).

3.2.2 Data acquisition

The base for the data acquisition and control was a National Instruments (NI) PXI-8106 real-time embedded controller (Fig. 3.2) with a NI PXI-6289 M-series multifunction data acquisition card. Figure 3.4 is a schematic of the data acquisition and control implementation. The card acquired data through a NI SCC-2345 signal conditioning carrier (SCC). The SCC-2345 (Fig. 3.5) contained the following signal conditioning modules; three SCC-TC02, one SCC-AI03 and one SCC-SG24, which received input from three thermocouples, a magnetostrictive position sensor (analog voltage) and a torque cell, respectively.

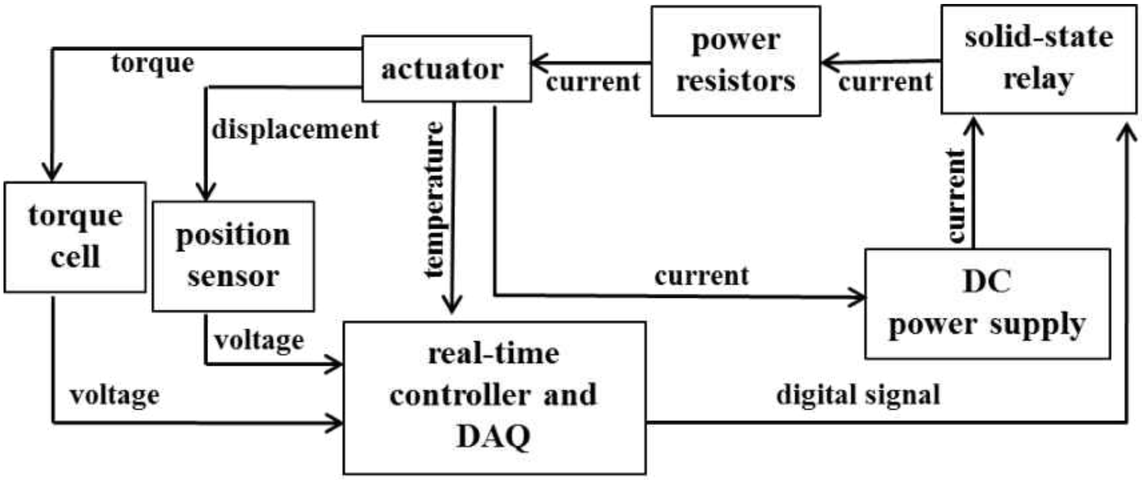

Figure 3.4: Overview of data acquisition and control implemented.

Figure 3.5: National Instruments signal conditioning carrier with various signal condition modules installed (see text for details).

A signal condition module SCC-DO01 (digitial ouput) was used to trigger the relay for heating. LabVIEW® was used to acquire temperature, displacement, and torque data synchronously in real time. Figure 3.6 shows the virtual instruments front panel which includes the ability to turn on/off the relay trigger, control of the upper and lower cycle temperatures and a Boolean indicator (green light) used to indicate the state of the relay. Also, included are the following real time plots: displacement, temperature and torque versus time, and temperature versus displacement.

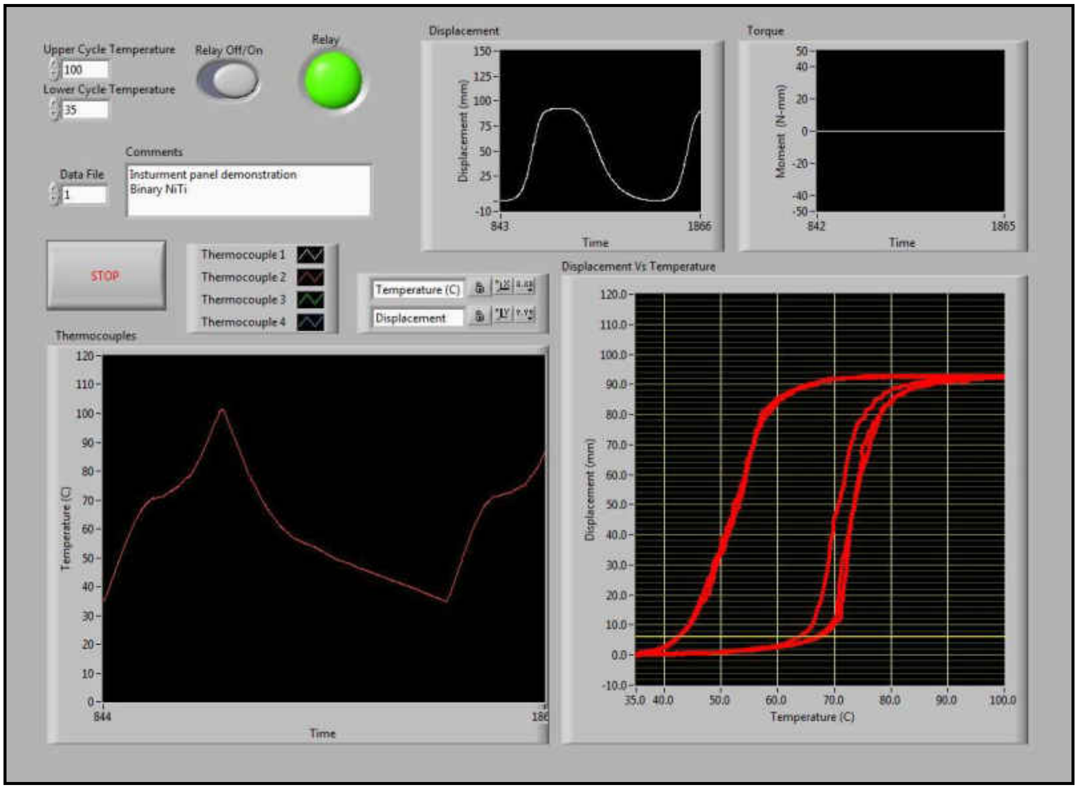

Upper Cycle Temperature 100

Lower Cycle Temperature 35

Data File 1

Comments: Insturment panel demonstration
Binary NiTi

Figure 3.6: Front panel of the virtual instrument used for data acquisition and control.

Figure 3.7a shows the block diagrams used to acquire data from the thermocouples, displacement and torque sensors. DAQ assist VIs were created and were then converted to block diagrams in order to handle error as needed. Timed loops were used which were set to iterate every 10 ms. Temperature data was acquired from four thermocouples. Figure 3.7b shows the block diagram used to determine displacement voltage output from the sensors (calibration parameters received from the manufactures were used). Figure 3.7c shows the block diagram used to determine displacement voltage output from the sensors (calibration parameters received from the manufactures were used).

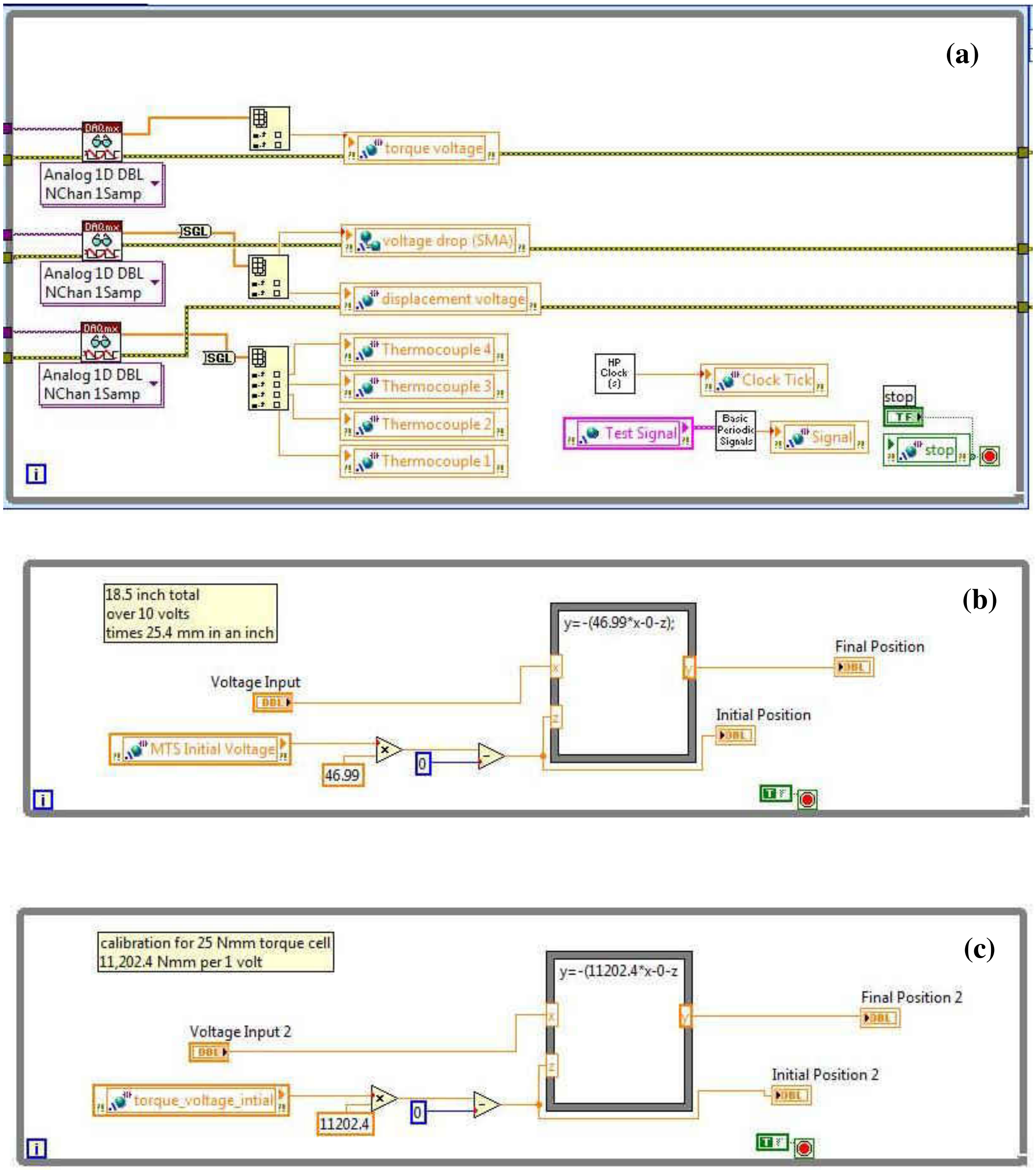

Figure 3.7: LabVIEW® block diagrams used for data acquisition: (a) main data acquisition loop; (b) torque cell voltage to torque loop; and (c) displacement sensor voltage to displacement loop.

Figure 3.8 shows the block diagram used to trigger the solid state relay, in which temperature data from thermocouple 2 is used. When the temperature of the thermocouple is below the set value for the UCT, the digital output connected to the relay is in the “on” state. Once the temperature exceeds the UCT the digital output is switched to the “off” state. Subsequently, when the temperature decreases to below the lower cycle temperature, the digital output is switched back to the “on” state, thus completing a cycle.

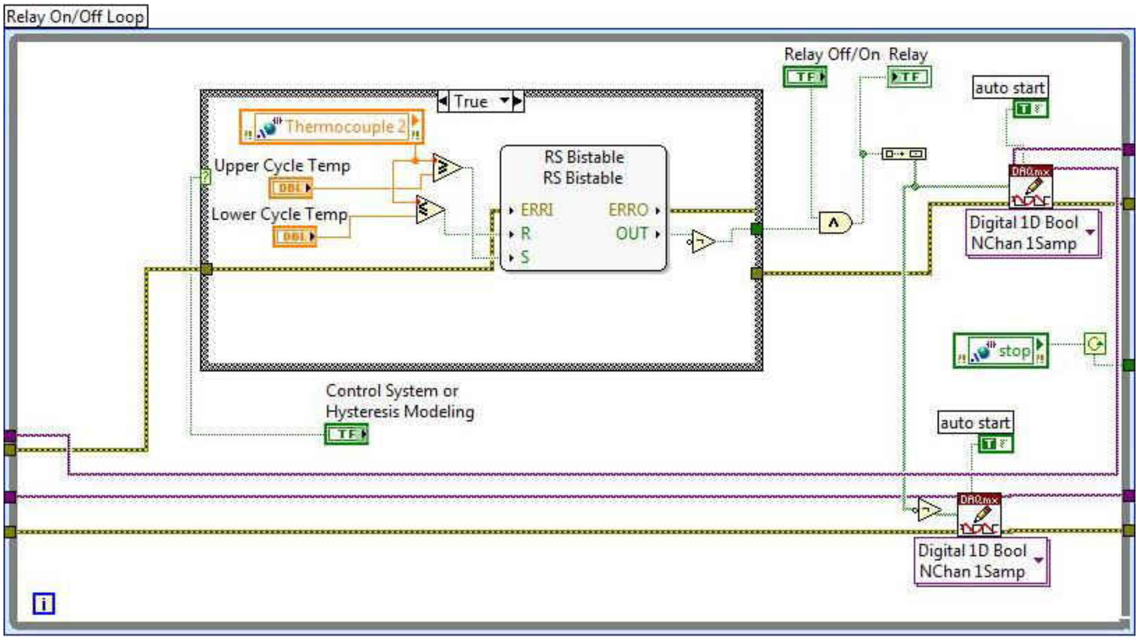

Figure 3.8: LabVIEW® block diagram used to switch “on” and “off” the digital output used to trigger the solid state relay.

3.2.3 Temperature measurement

Due to large displacements associated with SMA spring actuators, thermocouples were not welded on to the springs and other approaches were used. Two K-Type thermocouples were bonded on to the actuator with a thermally conductive, but electrically insulative, high temperature cement. Another two K-Type thermocouples were mechanically fastened using wire with a thermally conductive paste applied over the connection to ensure good conductivity. Figure 3.9 shows the results comparing the two methods of thermocouple attachment on a binary

NiTi spring with the geometry of spring *S1*. Both approaches resulted in similar measurements of temperature (within error). There is small temperature gradient between location 1(directly between the two mounts) and 2 (one half coil from mount) on the spring which was subsequently minimized by the Macor® spring mounts. The wire fastening approach was adopted for all tests since it was more robust for larger actuator stroke.

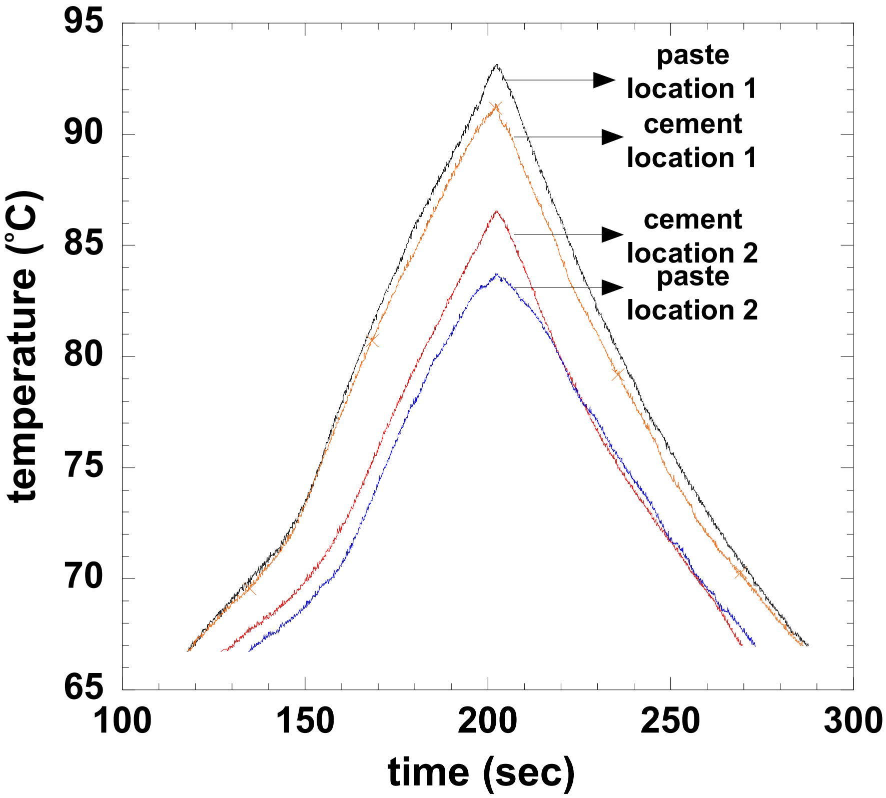

Figure 3.9: Comparison of temperatures from different thermocouples.

3.3 Thermomechanical testing

Using the setup described in Section 3.2, the following tests were performed. Isothermal load versus extension tests were conducted at room temperature for 16 load increments between 0 and 36.3 N for as-shape-set spring *S1* and for 23 load increments between 0 and 1.2 N for as-shape-set spring *S2* with the spring ends unconstrained and free to rotate. An isothermal load versus moment test was performed at room temperature for 7 load increments between 0 and 26.7 N for as-shape-set spring *S1,* where the load was applied with the spring ends prevented from rotating while the moment produced at the spring ends was measured.

All thermal cycling was performed between 180 ^{o}C and 320 ^{o}C. First, spring *S1* was thermally cycled 20 times under a constant load of 2.2 N with the ends of the spring allowed to rotate freely. Second, the same spring *S1* was thermally cycled 20 times under a constant load of 2.2 N with the ends of the spring prevented from rotating. These two conditions were repeated resulting in a total of 80 thermal cycles under a constant load of 2.2 N. The same procedure was then performed in succession under 4.4, 6.7, 8.9, 11.1 and 13.3 N loads, resulting in a total of approximately 500 thermal cycles under load. Spring *S2* was thermally cycled 150 times under a constant load of 1 N with the ends of the spring allowed to rotate freely. Note, springs *S1* and *S2,* with the aforementioned thermomechanical histories, will be referred to as cycled springs *S1* and *S2*.

Following thermal cycling, both springs were mechanically forced back onto the mandrel at room temperature to their starting geometries, but no further thermal processing (i.e., shape-setting, annealing, or aging) was done. The springs were then subjected to a final round of isothermal testing. Isothermal load versus extension tests were then conducted at room temperature for 18 load increments between 0 and 38.5 N for cycled spring *S1* and for 11 load increments between 0 and 1.2 N for cycled spring *S2*.

Following the aforementioned testing, cycled spring *S1* was placed back on the mandrel and shape-set again following the shape setting procedures previously described in Section 3.1. With the aforementioned history, this cycled and re-shape-set spring *S1* will be denoted spring *S1*-shape-set 2 (*SS2)*. After this second shape set, spring *S1-SS2* was thermally cycled 10 times under a constant load of 8.6 N. An isothermal load versus extension test was then conducted at room temperature for 22 load increments between 0 and 30 N for the cycled spring *S1-SS2*. Note spring *S1-SS2*, following cycling, was not forced back onto the mandrel prior to the isothermal load versus extension experiment.

3.4 Finite element method model

A three-dimensional FEM model was constructed for as-shape-set and cycled springs, *S1* and *S2*. The model was also used to view stresses in *S1* in the extended (as a result of unrecovered axial deformation) states (helix angles of 30° and 45°). The model was constructed in commercially available ANSYS software using eight-noded, solid isoparametric elements (parameters are summarized in Table 3.1).

Figure 3.10 displays the mesh for as-shape-set springs *S1* and *S2*. Boundary conditions were applied to all springs in a manner which simulates loading (applied loads are summarized in Table 1) of the springs in tension with ends free to rotate. A linear elastic material model was used, with Young's moduli obtained by assuming isotropy (presented later in Chapter 5). Poisson's ratio was taken to be υ=0.4 following Ref. [28]. Unrecovered axial deformation was accounted for in the initial configuration, in which it was assumed that material evolution had not occurred (again discussed in the context of the experimental results in Chapter 5). Large deformation was accounted for in ANSYS, i.e., the software updates nodal position as the solution proceeds to its final configuration. Note this model was used to assess non-linear behavior resulting from changing spring geometry. Anisotropic and non-linear SMA material behavior was not accounted for. Furthermore, the model was used to assess the degree of heterogeneity and multi-axiality in the stress state that developed in the spring. Model outputs include spring extension and the von Mises stress.

Table 3.1: Summary of FEM parameters.

Spring	**Elements**	**Applied Load (N)**
S1 (shape-set)	6,300	0,1,2,…,40
S2 (shape-set)	5,800	0,0.1,0.2,…,1.2
S1 (cycled)	5,800	0,1,2,…,40
S2 (cycled)	4,600	0,0.1,0.2,…,1.2
S1 (α=30°)	5,900	10
S1 (α=45°)	5,200	10

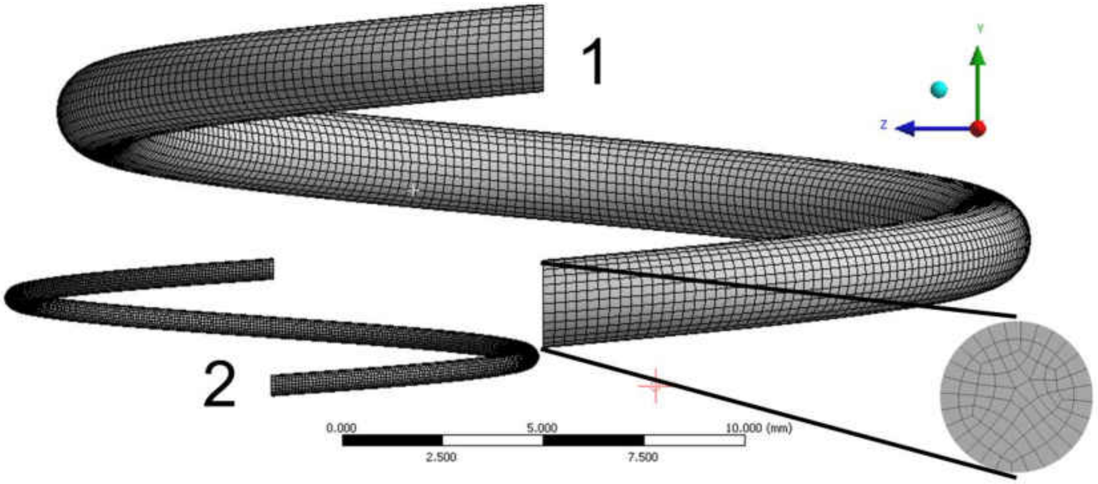

Figure 3.10: Finite element mesh for model of as-shape-set springs *S1* and *S*2. Also, displayed is the coordinate system adopted where the y-axis is the loading direction.

3.5 *In situ* neutron diffraction testing on $Ni_{29.5}Ti_{50.5}Pd_{20}$

This chapter provides a summary of the procedures for previously acquired neutron diffraction data Ref. [31] which is analyzed in this work . Emphasizes in this work will be on the data analysis. A brief review of the theory of neutron diffraction data analysis is given in Section 3.2.4 of this chapter. A detailed account of the data analysis performed using GSAS software is given in the next chapter.

3.5.1 Sample Preparation

The material used in the neutron diffraction experiments was a ternary $Ni_{29.5}Ti_{50.5}Pd_{20}$ alloy (at %), produced by vacuum induction melting in a graphite crucible. The ingot was homogenized at 1050 °C for 72 hours and furnace cooled and then hot extruded into rods at 900°C with an area reduction ratio of 7:1 to a final sample diameter of 9.48 mm. Samples were cut from the extruded rod by EDM to their final length of 23.87 mm.

3.5.2 Neutron diffraction measurements on SMARTS

In situ neutron diffraction was carried out during compressive loading while heating/cooling, using SMARTS at LANL in "time-of-flight" mode. SMARTS has a set of two detector banks, Bank 1 and 2, positioned across from one another as shown in Figure 3.11. A servo-hydraulic load frame with uniaxial tension and compression loading capabilities is mounted horizontally and positioned such that the sample forms a 45 degree angle with incident neutrons. Bank 1 collects diffracted beam from lattice planes with plane normal perpendicular to the loading direction. Bank 2 collects diffracted beam from lattice planes with plane normal parallel to the loading direction. Samples were heated using the high temperature furnace on SMARTS (Fig 3.12). Temperature was acquired (through two thermocouples mounted on the sample) and controlled via LabVIEW®. A detailed description of capabilities on SMARTS diffraction setup can be found in Ref. [43].

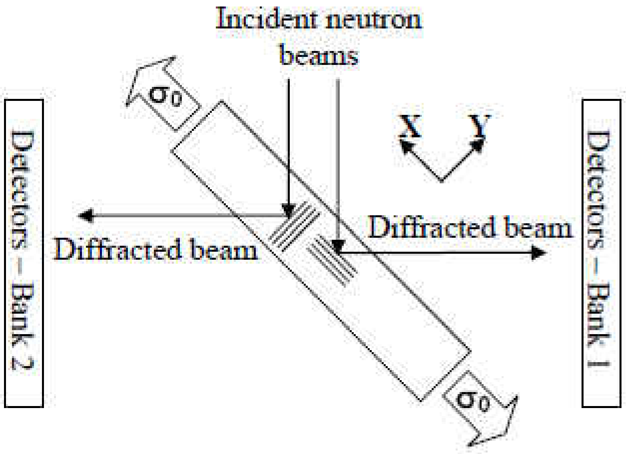

Figure 3.11: Schematic of sample and detector bank locations an orientation at SMARTS [44].

Figure 3.12: Load frame with high temperature furnace at SMARTS [43].

3.5.3 Procedures

All neutron diffraction experiments were conducted in load control mode. At each load and temperature a neutron beam count time of approximately 24 min (nominal beam current of 100 μA) was required to generate a neutron spectrum of sufficient statistical quality. A neutron spectrum was acquired prior to cycling at room temperature under no-load (compressive holding stress of -7 MPa). Load-bias cycles were performed between room temperature and an UCT which was varied with cycle. UCT is defined as the maximum temperature reached during a given thermal cycle. The UCT for each cycle is summarized in Table 3.2. For each load-bias cycle a neutron spectrum was acquired under load at room temperature and UCT. Two load-bias cycles were conducted at each of the following loads -100 MPa, -200 MPa and -300 MPa in sequence, followed by one load-bias cycle at -100 MPa. Following each load-bias cycle a neutron spectrum was acquired under no-load (compressive holding stress of -7 MPa) at RT. All neutron diffraction experiments are summarized in Table 3.2.

Table 3.2: Summary of load-bias cycles performed during neutron diffraction experiments.

Stress (Mpa)	**Temperature (°C)**	**Designation**
-7	**25**	**Cycle 0**
-100	**25**	
-100	**191**	**Cycle 1**
-100	**25**	
-100	**217**	**Cycle 2**
-100	**25**	
-200	**229**	**Cycle 3**
-200	**25**	
-200	**331**	**Cycle 4**
-200	**25**	
-300	**386**	**Cycle 5**
-300	**25**	
-300	**399**	**Cycle 6**
-300	**25**	
-100	**330**	**Cycle 7**
-100	**25**	

3.5.4 Neutron diffraction data analysis methodology

By examining raw diffraction spectra qualitative information can be obtained in the following manner. Shifts in peak position can provide information on elastic lattice. Changes in peak intensity can provide information on texture evolution and phase fraction. In the present study, overlapping raw spectra of cycles as described in Section 3.5.3 were used as one method to observe changes in texture and phase fraction between cycles.

In order to provide a more qualitative analysis, the following two methods for analyzing neutron diffraction spectra were implemented: single-peak fitting and Rietveld refinement. Single peak in the diffraction spectrum are fit with a convolution (of Gaussian and Lorentzian functions) profile function resolved by Windor, Jorgens and Von Dreele which is implemented via General Structure Analysis System (GSAS) software [45]. Figure 3.13 shows a representative single-peak shift related to lattice strain ε_{hkl}, for a plane, *hkl*, which is quantified as follows:

$$\varepsilon_{hkl} = \frac{d^{hkl} - d_0^{hkl}}{d_0^{hkl}} \tag{3.1}$$

where d_0^{hkl} and d^{hkl} are the planar d-spacing at initial and final state, respectively, of temperature and/or stress.

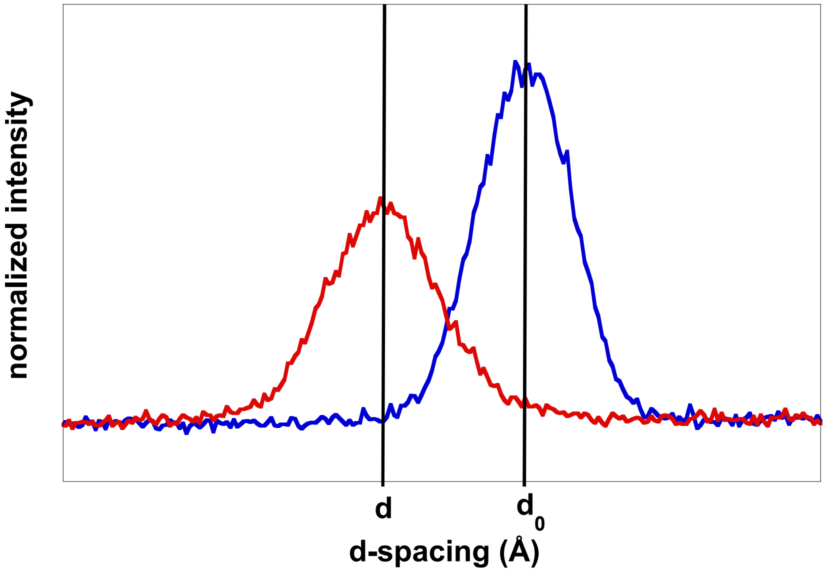

Figure 3.13: Representative peak shift in a neutron diffraction spectrum for a plane, *hkl*.

Rietveld refinement creates a theoretical line profile to fit the diffraction spectrum by method of least square approximation. In this approach phase volume fractions, phase texture and lattice parameters, etc. are varied until a least squares fit with the measured spectrum is obtained. Rieveld refinement is implemented in GSAS using the following mathematical model for the intensity Y_c at every point in the measured spectrum

$$Y_c = Y_b + \sum_h SKF_h^2 P(\Delta T_h) \tag{3.2}$$

where Y_b is the background intensity, S is the scale factor, K is a correction factor containing a description of the changes in predicted intensity due to texture, F_h is the structure factor and $P(\Delta T_h)$ is the profile function dependent on ΔT_h the profile point from the reflection position. An 8th order spherical harmonic description was implemented in the Rietveld refinement code in GSAS. Figure 3.14 shows a typical diffraction pattern acquired at SMARTS with a Rietveld refinement. The red ticks are the measured data and the green line through them is the Rietveld refinement. The purple curve below the data is the error between the Rietveld refinement and measured data.

The primary use of Rietveld refinements in this work was to analyze texture evolution and phase volume fraction. The texture evolution following an increase/decrease in stress, temperature or increment in cycle was examined using inverse pole figures (IPFs). An IPF shows the distribution of a selected direction in the sample relative to the crystal axis. Therefore, texture evolution in the direction perpendicular and parallel to loading was examined separately using this method. Quantification of phase volume faction utilized a two bank, two phase Rietveld refinement.

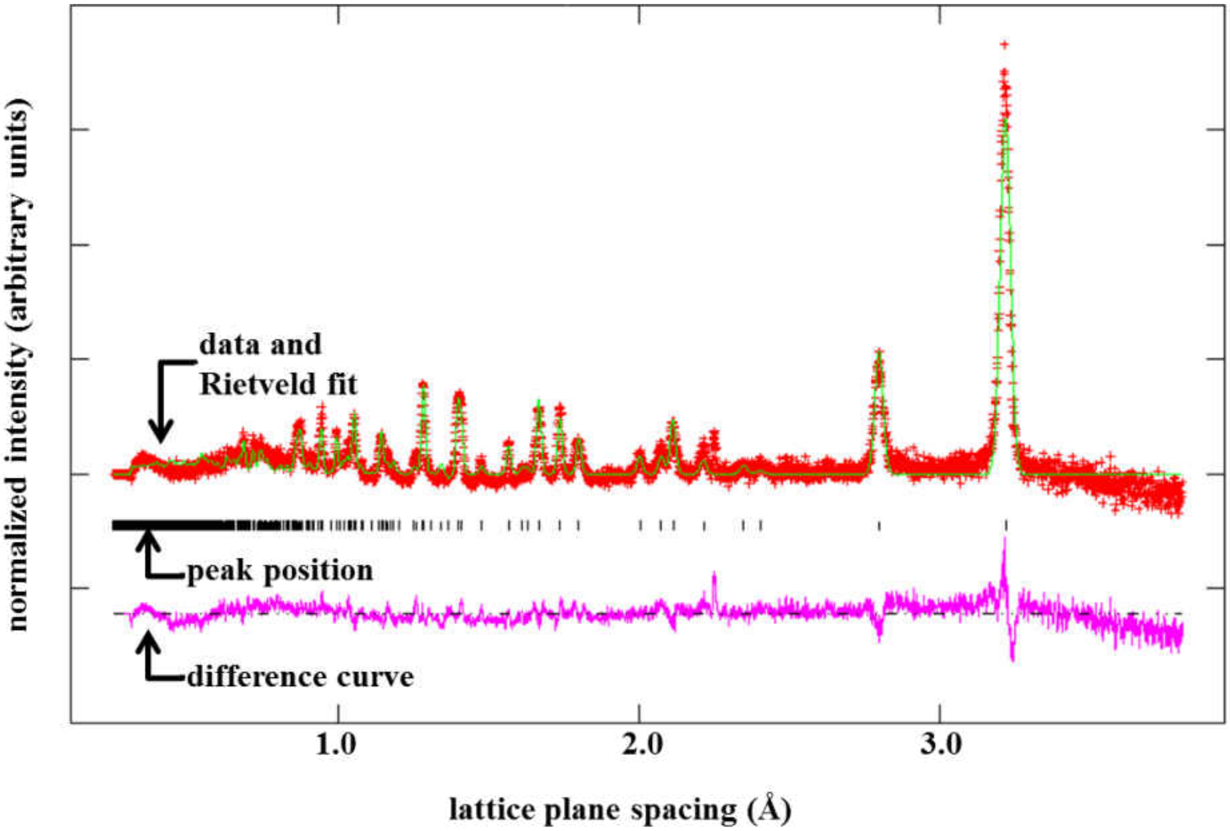

Figure 3.14: Typical Rietveld refinement of a neutron diffraction spectrum acquired at SMARTS.

CHAPTER FOUR: NEUTRON DIFFRACTION DATA ANALYSIS

This chapter outlines Rietveld analysis performed on available $Ni_{29.5}Ti_{50.5}Pd_{20}$ neutron diffraction data (see Section 3.5 for details on data) using the GSAS software. First, procedures for single bank Rietveld refinements for a single phase, either B19 martensite or B2 austenite, are outlined. These refinements are used primarily for texture analysis. Procedures for generating IPFs from the results of the single bank refinements are given. Next, procedures for two bank Rietveld refinements with coexisting phases (in this case B2 austenite and B19 retained martensite) are given. The objective of these refinements was to obtain volume fractions of B19 retained martensite present above the A_f. Finally, procedures for single peak fitting are outlined with the objective of obtaining lattice strains. Note, GSAS and EXPGUI, or the graphical user interface software designed for GSAS, are often used concurrently. This analysis is not restricted to $Ni_{29.5}Ti_{50.5}Pd_{20}$ and may be used as a tutorial for analysis of other materials with appropriate changes. The GSAS manual, articles and tutorials available in the following references [46, 47] provide supplemental information to these procedures. All results from the procedures in this chapter are reported in Chapter Six.

4.1 Single bank / single phase Rietveld refinement

This section outlines the procedures for Rietveld refinement of data from one detector bank (for this example Bank 1 as described in Section 3.5) and one phase B19 (orthorhombic). Before beginning a folder was created in the GSAS folder (C:\gsas\material\type_of_refinement\run#). For this example the folder was C:\gsas\NiTiPd\singlebank_B19\38470. This folder must contain the runnumber.gda and .iparm files. For this example these files were 38470.gda and smarts_141106.iparm as obtained from SMARTS. The .gda file contains the raw data from the experiment and the .iparm file contains the parameters specific to the instrument at the time the experiment was performed. Also, there is typically a .pdf file associated with the .gda file which shows the raw and normalized plots for both banks. It is advisable to keep the .pdf with the .gda file for reference but this file is not necessary for the Rietveld refinement.

4.1.1 Creation of an experiment file

First an experiment file is created as follows:

1. Open the GSAS software.
2. Click Setup > Expname
3. Locate the folder that was just created for this refinement.
4. Enter the file name for the experiment as run#_bank# (for this experiment 38470_1) and click open. Note it's always helpful to distinguish between bank numbers in this manner.
5. Click yes to create the file.
6. Click Setup > Expedt
7. Command prompt interface will open. "Do you wish to create it <Y/<N>?" input > y and press enter
8. Enter the title. Input > 38470_1 and press enter (this is the same as experiment name)
9. EXPEDT now opens. At any time enter can be hit to list the commands.
10. For powder data preparation. Input > p
11. For phases. Input > p
12. No phase exist. To read a phase. Input > r. Note, to save time Steps 10-12 could have been input in Step 10 as input > p p r and enter. This can be done throughout GSAS and will often be done henceforth in these procedures. At any time the commands can be entered one at a time and enter can be pressed to list the commands prior to entering them.

13. In windows 7 the file containing the phase information can be dragged into the command prompt. Otherwise, type its location in manually. For this step a previous .exp must exist for the material and phase. In this example NiTiPd B19 martensite. If not the phase information must be entered manually.

14. Select the phase. In this example only B19 martensite is in the source file only. Input > 1

15. Exit phase selection. Input > x

16. To enter the raw histogram (.gda) file. Input> H I

17. Enter the .gda file.

18. Input > y y

19. Enter bank number (bank 1). Input > 1 N

20. Enter frame orientation (135 0 0 for SMARTS at LANL). Input > a 135 0 0

21. Set a minimum D-spacing. Input > d 0.6

22. Exit EXPEDT. Input > / x

23. Input > 0 x x x

4.1.2 Refinement of experiment files in EXPGUI

Open the folder C:\gsas\NiTiPd\singlebank_B19\38470. The experiment file 38470_1.exp should now be there. Now refinement can be performed in EXPGUI as follows:

1. Double-click the experiment file to open it in EXGUI.
2. Select the Phase tab. Verify phase information and make sure “Refine Cell” is unchecked.

3. Select the Profile tab and make sure every parameter is unchecked.

4. Select SH Pref Orient (corresponds to texture). Uncheck “Refine ODF coefficents”. Spherical harmonics order should be as low as possible (for this example, 12 and 6 were used for B19 martensite and B2 austenite, respectively). It is important to use the same spherical harmonic order from run to run of the same type when data is going to be compared.

5. Perform a refinement

   a) Make a copy of the experiment file. This is in case the refinement diverges in subsequent steps. If this occurs delete the experiment file and rename the last copy to replace the experiment file.

   b) Click powpref.

   c) Then, click genles. Figure 4.1 shows a genles output with reduced Chi square as circled. Continue to run genles until the Chi squared converges.

   d) Click powplot.

   e) Powplot will open in the command prompt. To view the refinement input > c n c b d n i m p. The raw data is indicated by "+" and the Rietveld refinement by the green line. The pink line at the bottom indicates error.

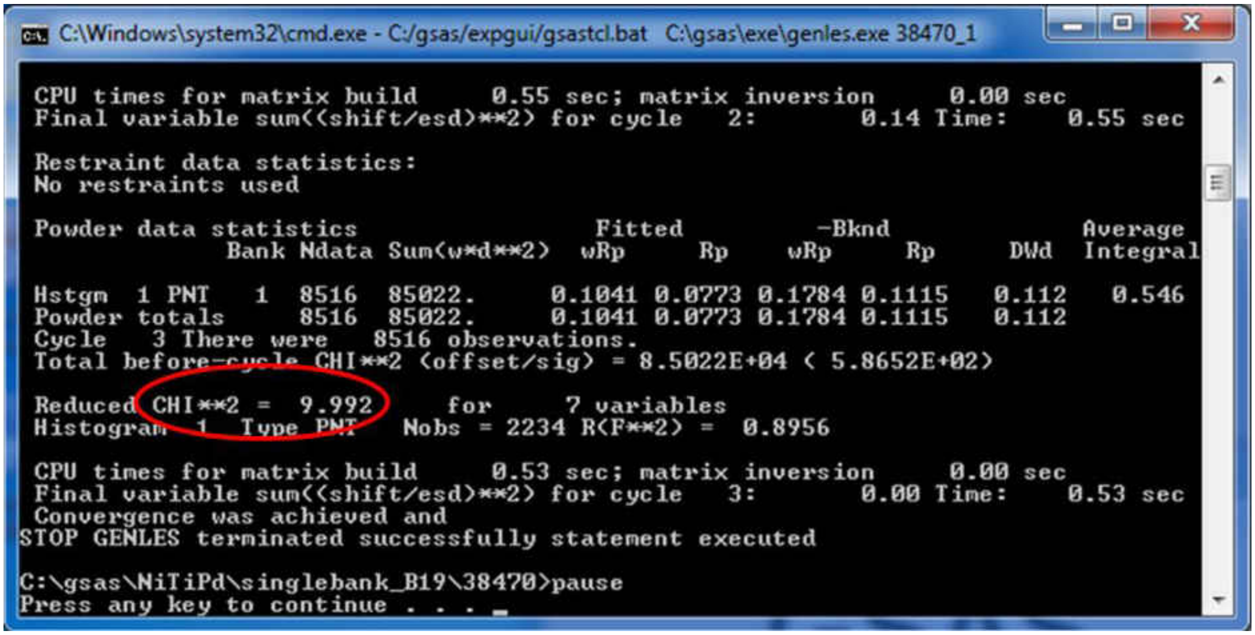

```
 CPU times for matrix build     0.55 sec; matrix inversion     0.00 sec
 Final variable sum((shift/esd)**2) for cycle   2:       0.14 Time:    0.55 sec

 Restraint data statistics:
 No restraints used

 Powder data statistics                   Fitted          -Bknd              Average
              Bank Ndata Sum(w*d**2)   wRp     Rp     wRp     Rp     DWd   Integral

 Hstgm  1 PNT   1  8516  85022.      0.1041 0.0773 0.1784 0.1115   0.112   0.546
 Powder totals     8516  85022.      0.1041 0.0773 0.1784 0.1115   0.112
 Cycle   3 There were   8516 observations.
 Total before-cycle CHI**2 (offset/sig) = 8.5022E+04 ( 5.8652E+02)

 Reduced CHI**2 =   9.992      for      7 variables
 Histogram  1  Type PNT   Nobs = 2234 R(F**2) =  0.8956

 CPU times for matrix build     0.53 sec; matrix inversion     0.00 sec
 Final variable sum((shift/esd)**2) for cycle   3:       0.00 Time:    0.53 sec
 Convergence was achieved and
STOP GENLES terminated successfully statement executed

C:\gsas\NiTiPd\singlebank_B19\38470>pause
Press any key to continue . . . _
```

Figure 4.1: Genles output following a Rietveld refinement, with emphasizes placed on the reduced Chi squared.

The objective is to repeat refinements until the reduced Chi square is as close to 1 as possible, while maintaining a good fit. Between refinements parameters will be adjusted. This involves a little bit of "trial and error"! Guidelines will be given in following steps, however should be changed as needed.

6. Click the Phase tab. Check “Refine Cell”. Repeat Step 5.

7. Click SH Pref Orient. Check “Refine ODF coefficients”. Repeat Step 5.

8. Uncheck “Refine ODF coefficients”. Click Profile tab. Check “rsta”. This for Tetragonal/Orthorombic/Monoclinic structures. If the structure were cubic check “rsca”. Repeat Step 5. Note refine cell, “rsta” and “rsca” refine peak location.

9. Repeat Step 6.

10. Uncheck “Refine ODF coefficients”. Click Profile tab. Check “sig-0” and “sig-2”. Repeat Step 5. Note “sig-#” refines peak broadening.

11. Repeat Step 6.

12. Uncheck “Refine ODF coefficients”. Click Profile tab. Check “sig-1”. Repeat Step 5.

13. Repeat Step 6.

14. Click Histogram tab. Check “Refine Abs./Refl.”. Repeat Step 5. The Chi squared for the B19 NiTiPd is 3.7. This is about as low as can be achieved for the B19 phase of this material.

4.1.3 Refinement of additional runs of same type (SmartsRunRep)

If there are additional runs of the same type (i.e., same material and structure) the refinement made in Section 4.1.2 can be used to refine the additional runs. SmartsRunRep is part SMARTSware, a software package available at [48]. This Section assumes SMARTSware is installed and rooted properly. SmartsRunRep is a batch Rietveld refinement which will automatically repeat the steps taken for an existing refinement (for this example the refinement performed in Section 4.1.2) for as many runs as desired.

1. Copy the experiment file C:\gsas\NiTiPd\singlebank_B19\38470\38470_1 and paste it into C:\gsas\NiTiPd\singlebank_B19.

2. Copy the .gda files of all the runs to be refined by smartsrunrep and the .iparm file into this same folder.

3. Create a text file named run. The run file contains a list of the runs to perform smartsrunrep on. In this example it is as follows:

```
38514
38540
```

38548
38592
38632
38671
38717

Note reference to bank # is not included.

4. Go into the folder C:\gsas\NiTiPd\ and hold Shift, right click the singlebank_B19 folder and click open command window here.

5. To launch smartsrunrep. Input> smartsrunrep.

6. To read from the run file just created. Input > 2

7. Input > run.txt

8. Enter the source run. This is the experiment file refined in section 4.1.2. Input > 38470_1

9. Select the bank. Input > 1

10. Input > 0

11. To create a pdf file with the output. Input > y

12. Enter the title for the runs. Input > NiTiPd_B19_Bank1

13. Smartrunrep will now automatically refine all of the runs in the run file.

14. Perform Step 5 of section 4.1.2 for each refinement generated by smartsrunrep to verify that Chi square and fits are acceptable. Make further changes and refinements as needed.

SmartsRunRep will fail sometimes. If this occurs each run would have to be done manually as in Section 4.1.2.

4.2 Generating inverse pole figures (SmartsInvPol)

SmartsInvPol is part SMARTSware, a software package available at [48]. This Section assumes SMARTSware is installed and rooted properly. Now, IPFs are generated from the refinements as follows:

1. Add the source file for the smartsrunrep refinements to list of runs in the run.txt file. This is so the pole figure for the source refinement will be generated.

2. Go into the folder C:\gsas\NiTiPd\ and hold Shift, right click the singlebank_B19 folder and click open command window here.

3. To launch smartsinvpol. Input> smartsinvpol. This step assumes all the proper SMARTS software (SMARTSware available at [http://public.lanl.gov/clause /SMARTSware.html]) is installed and rooted properly.

4. To read from the run file just created. Input > 2

5. Input > run.txt

6. Input > 0

7. Select the bank. Input > 1

8. Enter phase number. Only one phase is present. Input > 1

9. Select the structure. For this example the structure B19 (Orthorhombic). Input > 3

10. Read nominal lattice parameters from LST file. Input > 0

11. Input > 0

12. Select the resolution. Input > 2

13. Input > 1

14. Enter the title for the runs. Input > NiTiPd_B19_Bank1

15. Input > 0

16. To give a fixed range for the plots. Input > 1

17. Enter a range. Smartsinvpol may need to be ran again once the range of results is known. Adjust accordingly on subsequent attempts to encompasses the proper range.

18. Input > 1

19. The IPF's will appear as postscript files in C:\gsas\NiTiPd\singlebank_ B19. Verify each IPF for consistency.

4.3 Two bank / two phase Rietveld refinement

This section covers the procedures for Rietveld refinement of two detector bank (for this example bank 1 and bank 2 of SMARTS as described in section 3.2) and two phases B2 (Cubic) and B19 (orthorhombic). Similar to Section 4.1 a folder is created for these refinements as C:\gsas\NiTiPd\phasefraction\38701 containing the .gda and .iparm files. Section 4.1.2 will often be referenced as this refinement will be similar.

4.3.1 Creation of an experiment file

1. Follow Steps 1-11 of section 4.1.1. This run will be labeled run 38701_0 (the 0 refers to 2 banks).
2. No phase exist. To read a phase. Input > r
3. Enter the source experiment file containing the phase information for both phases. If one does not exist (input > i) in Step 2 to enter the phase information manually.
4. Select the phase. In this example B2 Austenite and B19 Martensite are in the source file. To enter B2 Austenite. Input > 1
5. Repeat Step 2-4 to add B19 martensite phase information.
6. To verify information both phases are present. Input > l
7. Exit phase selection. Input > x
8. Follow Steps 16-17 of section 4.1.1.
9. Enter bank number (bank 1). Input > 1 N
10. Enter frame orientation (135 0 0 for SMARTS at LANL). Input > a 135 0 0
11. Set a minimum D-spacing. Input > d 0.6
12. Input > x. Repeat Steps 8-12 for bank 2.
13. Input > 0 x x

14. To set the constraints for least squares. Input > l

15. Edit overall parameters. Input > o

16. Phase and element fractions. Input > s

17. Set constraints. Input > k

18. To enter the constraints. Input > i

19. Enter the first constraint (phase number, bank number, constraint). Input > 1 1 1

20. Enter the second constraint (phase number, bank number, constraint). Input > 1 2 1

21. Hit enter to terminate. To verify the constraints. Input > l

22. Exit expedt. Input > x x x x x

4.3.2 Refinement of experiment files in EXPGUI

Open the folder C:\gsas\NiTiPd\phasefraction\38701_0. The experiment file 38701_0.exp should now be there. Now refinement can be performed in EXPGUI as follows:

1. Double-click the experiment file to open it in EXGUI.
2. Select the Phase tab. Notice phase 1 or 2 can be selected. Verify phase information and make sure “Refine Cell” is unchecked in both phases.

3. Select the Profile tab. Notice the bank can be selected under select histogram. Make sure every parameter is unchecked for both phases and banks.

4. Select SH Pref Orient (corresponds to texture). Uncheck “Refine ODF coefficents” for both phases. Spherical harmonics order should be as low as possible (12 and 6 were used for B19 martensite and B2 austenite, respectively). It is important to use the same spherical harmonic order from run to run of the same type when data is going to be compared.

5. Select the Scaling tab. Notice under “select a histogram” a bank can be chosen. Under phase fractions check “Refine” for phase 1. Do this for both banks. This turns on the constraint that requires both banks to have the same phase fractions. Note every time a parameter is changed it should be changed for both banks unless otherwise stated. However, phases will be refined one at a time starting with the dominant phase.

6. Follow Step 5 of Section 4.1.1. It's important to view both histograms in this step. To view the histogram and refinement of bank 2 replace Step 5e with input > c n c b d n n i m p

7. Refine phase one. Click on Phase tab check "refine cell" only for phase one (should be the dominant phase).

8. Repeat Step 6.

9. Only perform this Step if subsequent steps fail on first attempt. Prior to Refining ODF coefficents (refinement for texture) for the first time in Step 9 the peaks of the refinement should have similar position to the peaks of the data. The peaks of the data will often be shifted be strain, thus, the peaks of the refinement need to be shifted accordingly. Otherwise, when Step 9 is performed the refinement will not "catch" the data. This can be done by manually changing the lattice parameters under Phase tab > "edit cell". Make a very small adjustment (< 0.005 Å) and perform Step 6 after each adjustment. The goal is to get the black dashes underneath peaks (which indicate peak position) as close the data peaks as possible. This is a case where "trial and error" is involved. Also "rstr" under the profile tab can be used to adjust for lattice strain in this Step, but be weary when using this as it may affect Rietveld strain output.

10. Click on the SH Pref Orient tab. Check "Refine ODF coefficients" only for phase one.

11. Repeat Step 6.

12. Uncheck "Refine ODF coefficients".

13. Click on the Profile tab. Check "rsca" only for phase one and for both banks. Note, "rsca" is for Cubic structures. In this example current phase (phase one) is B2 Austenite (Cubic).

14. Repeat Steps 8, 10-12.

15. Click Profile tab. Check "sig-0" and "sig-2" only for phase one. Repeat Step 6.

16. Repeat Steps 10-11.

17. Click Histogram tab. Check "Refine Abs./Refl.".

18. Refine phase two. Uncheck everything except for Scaling for phase one and two on both banks.

19. Click on Phase tab check "refine cell" only for phase two.

20. Repeat Step 8, 10-12.

21. Click on the Profile tab. Check “rsta” only for phase two and for both banks. Note, “rsta” is for tetragonal/orthorhombic/monoclinic structures. In this example current phase (phase two) is B19 Martensite (Orthorhombic).

22. Repeat Step 8, 10-12.

23. Click Profile tab. Check “sig-0” and “sig-2” only for phase two. Repeat Step 6.
24. Repeat Steps 10-11.

25. Click Histogram tab. Check “Refine Abs./Refl.”.

26. Turn on all parameter used for both phases on both banks. Repeat Step 6. A Chi squared of 1.9 was obtained at this point in the refinement. This is about as low as can be obtained for this type of refinement with NiTiPd for this run without increasing the Spherical Harmonic Order.

4.3.3 Obtaining phase fraction

The objective of the refinement in 4.2.3 was obtaining volume faction. This is done using reflist in GSAS, as follows:

1. With expgui still open. Click Results > reflist

2. Reflist will open in the command prompt. Input >1 m 0

3. Go to the folder C:\gsas\NiTiPd\phasefraction\38701_0. Refresh the folder if it is already open.

4. Open 38701.lst and Scroll down almost to the bottom. The output for phase fraction for 38701 is shown as follows:

```
Phase/element fractions for phase no.  1

 Hist Elem:     1 1 PNT       2 1 PNT
 Fraction :   8.04815       8.04815
 Sigmas   :  0.727724      0.727724
 Shift/esd:     -0.21         -0.21
 Wt. Frac.:   0.80333       0.80333
 Sigmas   :  0.142859E-01  0.142859E-01

 Phase/element fractions for phase no.  2
```

```
Hist Elem:     1 1 PNT       2 1 PNT
Fraction :   1.00000       1.00000
Sigmas   :   0.00000       0.00000
Shift/esd:     0.00          0.00
Wt. Frac.:   0.19667       0.19667
Sigmas   :   0.00000       0.00000
Phase/element fraction sum(shift/error)**2 :      0.09
```

4.4 Single peak fitting

This section outlines the procedures for single peak fits, using SmartsSPF, performed to quantify lattice strains from the NiTiPd data. SmartsSPF is part SMARTSware, a software package available at [48]. This Section assumes SMARTSware is installed and rooted properly. Similar to Section 4.1 a folder is created for these refinements as C:\gsas\NiTiPd\SPF_B19\hkl containing all .gda files to be refined and the .iparm file. Note, a subfolder will be created for each hkl peak (in this example the 011 will be refined) to be refined. All runs in an hkl folder are normalized to the first run as defined by the run.txt file. Single peak fitting is performed using SmartsSPF as follows:

1. A peak identification file (labeled pkid.txt) needs to be created in the C:\gsas\NiTiPd\SPF_B19\011 as follows:

```
$ Lines that start with a $ are comment lines
$ List peaks and interval for single peak fitting
$ Give position in TOF !!!
$Bank     Peak_ID   #of_peaks Pos1      Pos2      ....     Interval
1         011       1         3.218     0.1
2         011       1         3.218     0.1
```

   This file contains the hkl of the peak (011), number of peaks (1), d-spacing of the peak (3.218) and the approximate width of the peak (0.1). The d-spacing for a given hkl can be calculated in the conventional manner from the lattice parameters obtained from the Rietveld refinement performed in Section 4.1 or literature. The d-spacing will often be shifted by strain, thus, the position of the peak should be verified by viewing the normalized spectrum. If shifted adjust accordingly in the pkid file.

2. Go into the folder C:\gsas\NiTiPd\SPF_B19 and hold Shift, right click the SPF_B19 folder and click open command window here.

3. To launch smartsspf. Input> smartsspf. This step assumes all the proper SMARTS software (SMARTSware available at [http://public.lanl.gov/clause /SMARTSware.html]) is installed and rooted properly.

4. Input > 1

5. To read from the run file. Input>2

6. Enter the run file. Input > run.txt

7. Input > y y

8. Input > 1

9. For real number output. Input > 1

10. Choose the pkid file. Input > pkid.txt

11. Input > 1 y

12. A pdf will be created for each run which shows the data peak and the fit. Verify that each fit is good.

13. The SmartsSPF.txt file contains the output. Open it in excel to view lattice strains and errors for the peak for both banks.

CHAPTER FIVE: THERMOMECHANICAL BEHAVIOR OF $Ni_{19.5}Ti_{50.5}Pd_{25}Pt_5$ SPRINGS

This Chapter presents the results and analysis of the experiments performed on $Ni_{19.5}Ti_{50.5}Pd_{25}Pt_5$ springs and provides a discussion of the springs' thermomechanical behavior. Experimental procedures for these results are given in Chapter 3. To facilitate data comparison between the two spring geometries, the following normalization, adapted from [28], was implemented on all data presented:

$$\delta_{norm} = \delta_{data}\left(n/n_{data}\right) \tag{5.1}$$

where δ_{data} is the extension from the raw data, n_{data} is the number of active turns of the spring and n is the normalized number of active turns arbitrarily chosen to be 10.

5.1 Monotonic behavior of as-shape-set $Ni_{19.5}Ti_{50.5}Pd_{25}Pt_5$ springs at room temperature

5.1.1 Initial response and apparent elastic properties

Figure 5.1 shows the isothermal experimental load versus extension data acquired at room temperature from the as-shape-set spring *S1*. Given that the observed load versus extension response in two regions was mostly linear (i.e., 0-12.6 N and 12.7-40N with linear correlation coefficients of 0.998 and 0.996, respectively), the following relation from Ref.[30] was used to fit the data in each region

$$\delta = \frac{8PD^3n}{Gd^4}\left[1-\frac{3}{16C^2}+\frac{(3+\nu)}{2(1+\nu)}\tan^2\alpha\right] \tag{5.2}$$

where δ is the extension, P is the applied axial load, D is the coil diameter, d is the wire diameter, C is the spring index (D/d), α is the helix angle, υ is the Poisson ratio and G is the shear modulus. The Poisson ratio was taken to be υ=0.4 following Ref. [28]. Using an initial helix angle of 5^{o} for α, a value of 20.1 GPa was obtained for the shear modulus in the first linear region (i.e., 0-12.6 N) and a value of 10.9 GPa was obtained for the shear modulus in the second linear region (i.e., 12.7-40 N).

Implicit in this approach is the fact that microstructural effects in the spring (i.e., martensite variant reorientation and detwinning) are coupled with its linear elastic behavior resulting in an apparent or observed response that is overall linear as shown in Figure 5.1. Also, non-linear contributions that can be associated with the geometry of the spring (to be explained in more detail in subsequent sections) are ignored when fitting for the shear modulus using this approach. Thus, the shear moduli obtained by this method are considered apparent shear moduli G_a.

The observed response, specifically the observation of two linear regions as shown in Figure 5.1, is not typical of most materials (see Ref. [37] for spring response of linear elastic materials). It is possible that the first linear region corresponds to mostly linear elastic behavior of both the material and the spring. The second region probably corresponds to inelastic behavior associated with either the material (i.e., microstructural evolution due to variant reorientation or detwinning) or the spring (i.e., break down of applied force being proportional to extension) or a combination of these two effects. To investigate this further, the values of the apparent shear moduli obtained in Figure 5.1 are compared below with the known uniaxial behavior of $Ni_{19.5}Ti_{50.5}Pd_{25}Pt_5$. It is well known that NiTi based SMAs are not linear elastic materials, while the theory adopted here Ref. [18] is limited to linear elastic springs. However, the apparent moduli considered here are used in conjunction with this theory and the applicability of its use is justified in the proceeding discussion proceeds.

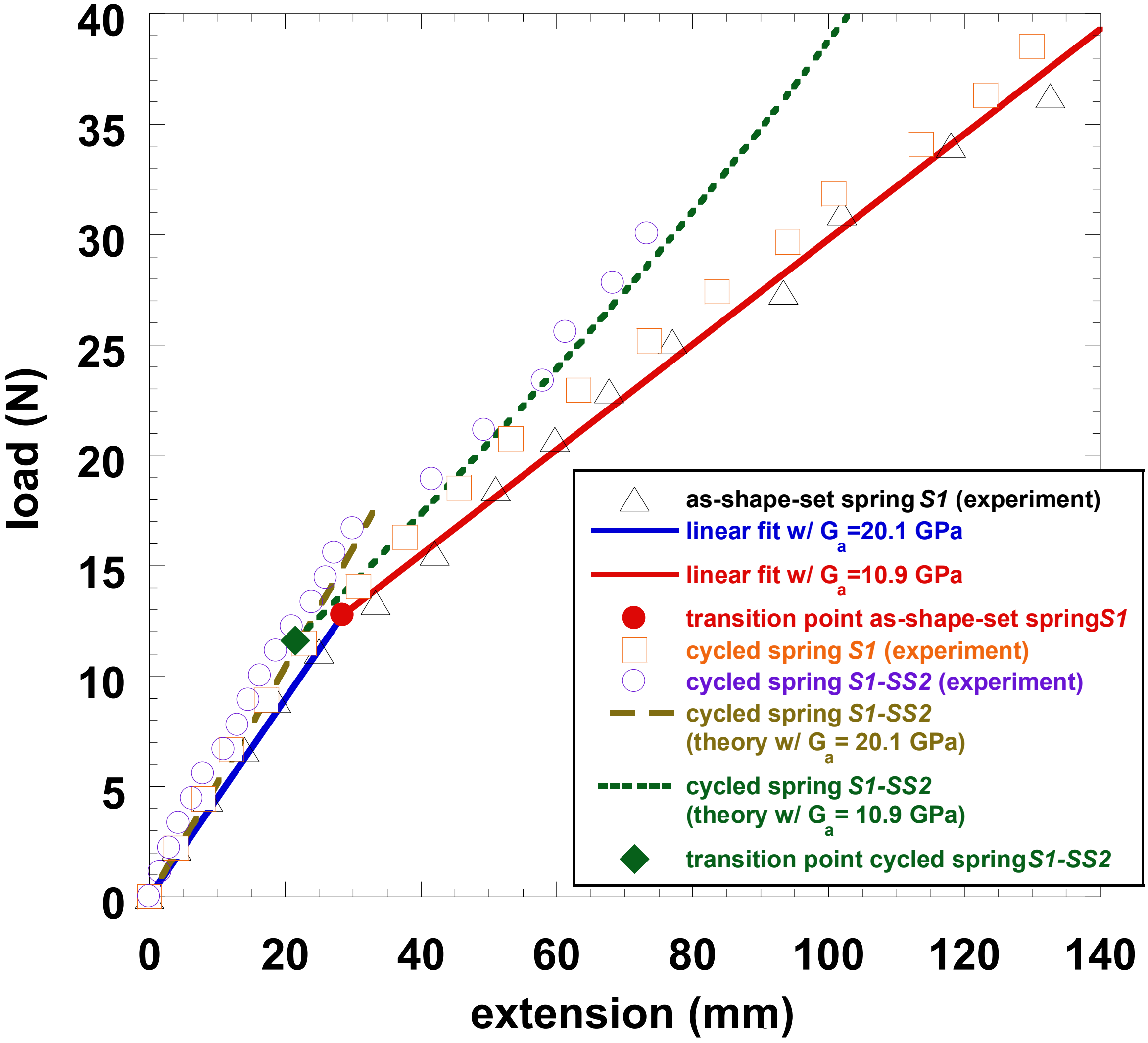

Figure 5.1: Room-temperature isothermal load versus extension response of as-shape-set spring *S1*, cycled spring *S1* and cycled spring *S1*-*SS2*. Also shown are linear fits to determine apparent moduli, model results using the theory outlined in the text and transition points in the observed piecewise linear behaviors.

5.1.2 Comparison to uniaxial stress-strain material behavior

Figure 5.2 shows the monotonic uniaxial stress strain plot for $Ni_{19.5}Ti_{50.5}Pd_{25}Pt_5$ conducted on bulk material at 50 °C below the martensite finish temperature (i.e., 178 °C, from Ref.[21]). To compare the behavior of spring *S1* in Figure 5.1 with the uniaxial behavior of the bulk material in Figure 5.2, it is necessary to first determine the so-called transition point of Figure 5.1, where the first linear region ends and the second linear region begins, in the stress-strain space of Figure 5.2. This was done as follows. From Ref. [30] the shear stresses, τ, and normal stresses, σ, in a spring can be obtained in cylindrical coordinates (r, θ, z) using the same variables defined in Equation 5.2:

$$\tau_{r\theta} = \tau_{rz} = \sigma_r = 0 \tag{5.3}$$

$$\tau_{\theta z} = \frac{8PD}{\pi d^3}\left(1 + \frac{5}{4C} + \frac{7}{8C^2}\right) \tag{5.4}$$

$$\sigma_\theta = \frac{8PD}{\pi d^3}\left(\frac{\left(-2 + \nu + 4\nu^2\right)}{4(1+\nu)C}\tan\alpha\right) \tag{5.5}$$

$$\sigma_z = \frac{8PD}{\pi d^3}\left(2\tan\alpha + \frac{(11+12\nu)}{4(1+\nu)C}\tan\alpha\right) \tag{5.6}$$

Equations (5.3-5.6) can then be combined to obtain the von Mises stress:

$$\sigma_{vm} = \sqrt{\sigma_{\theta\theta}^2 + \sigma_{zz}^2 - \sigma_{\theta\theta}\sigma_{zz} + 3\tau_{\theta z}^2} \tag{5.7}$$

By considering the load at which the transition point occurs in Figure 5.1 (i.e., P=12.6 N for spring *S1*), a value of 144 MPa was obtained for σ_{vm} from Equation 5.7, and thereafter called σ_{vm}^{tran}. Note, σ_{vm}^{tran} represents the maximum von Mises stress, which is highest at the inner most point of the cross-section (relative to the spring axis) and varies to near zero at the center of the wire cross-section [37].

The apparent shear moduli obtained from Figure 5.1 were converted to apparent Young's moduli of 56.3 GPa and 30.5 GPa, for the first and second linear regions, respectively, assuming elastic isotropy. Note, implicit in this assumption is the fact that anisotropic effects typically observed in SMAs are embedded in the apparent moduli. By considering the values of 144 MPa for σ_{vm}^{tran} and 56.3 GPa for E_a, the strain corresponding to the transition point was determined using Hooke's law to be 0.26 %. The two apparent Young's moduli are plotted in Figure 5.2. Thus, the piece-wise linear load-extension response of the spring *S1* in Figure 5.1 is represented in uniaxial stress-strain space in Figure 5.2.

The data in Figure 5.2 suggests that the primary mechanism for the deviation between the two linear regions for the spring response is the onset of bulk detwinning and/or variant reorientation. The first linear region in Figure 5.1 is consistent with elastic behavior, with possible very limited detwinning and/or variant reorientation that is known to occur at small strains Ref. [49], while, the second linear region has a decreased slope due to bulk detwinning and/or variant reorientation. At the maximum load of 35 N for spring *S1* the extension is 137 mm (216% increase in length) and the von Mises stress (determined by Equation 5.7) is 400 MPa.

Following the spring response in Figure 3 for the second linear region it can be observed that even at the maximum stresses (400 MPa) seen here strains are small (< 1.1% for spring *S1*). Inherent to the spring geometry is the fact that despite large spring extensions (216% increase in spring length), strains remain small (1.1% increase in strain). Thus, in the second linear region the effects of bulk detwinning and/or variant reorientation which are occurring should be limited.

In Figure 5.2, the apparent Young's modulus corresponding to the second linear region is larger than the uniaxial stress-strain response. Under large deformation caused by monotonic loading, a spring's response can be expected to become non-linear (i.e., applied force not proportional to extension) even if the material remains linear elastic. This effect arises due to geometry changes as the coil diameter decreases and the helix angle increases, and is a direct result of the spring length increasing while the wire length is constant. The spring deflection as presented in Equation 5.2 quantifies the response of a linear spring as the eqaution assumes constant coil diameter and helix angle as the extension increases. For large extensions and the helix angle and coil diameter can be related to the wire and spring lengths (as shown in the next section). The error between the apparent Young's modulus and the stress-strain response above the transition point in Figure 5.2 can be attributed to this aforementioned change in geometry. In comparing multi-axial spring and uniaxial behaviors in Figure 5.1 and 5.2, it can be concluded from Equation 5.2 it can be concluded that D and G_a are both decreasing at a rate such that D^3/G_a is essentially constant, resulting in a linear relationship between δ and P in the second linear region (i.e., above σ_{vm}^{tran}) of Figure 5.1. Note, the helix angle α also affects the linearity of the response and the relationships between D and α are developed in the next section. The error between the apparent Young's modulus and the stress-strain response above the transition point in Figure 5.2 may also be due to inherent differences in material microstructural development (e.g., variant selection) under uniaxial and multi-axial loading conditions.

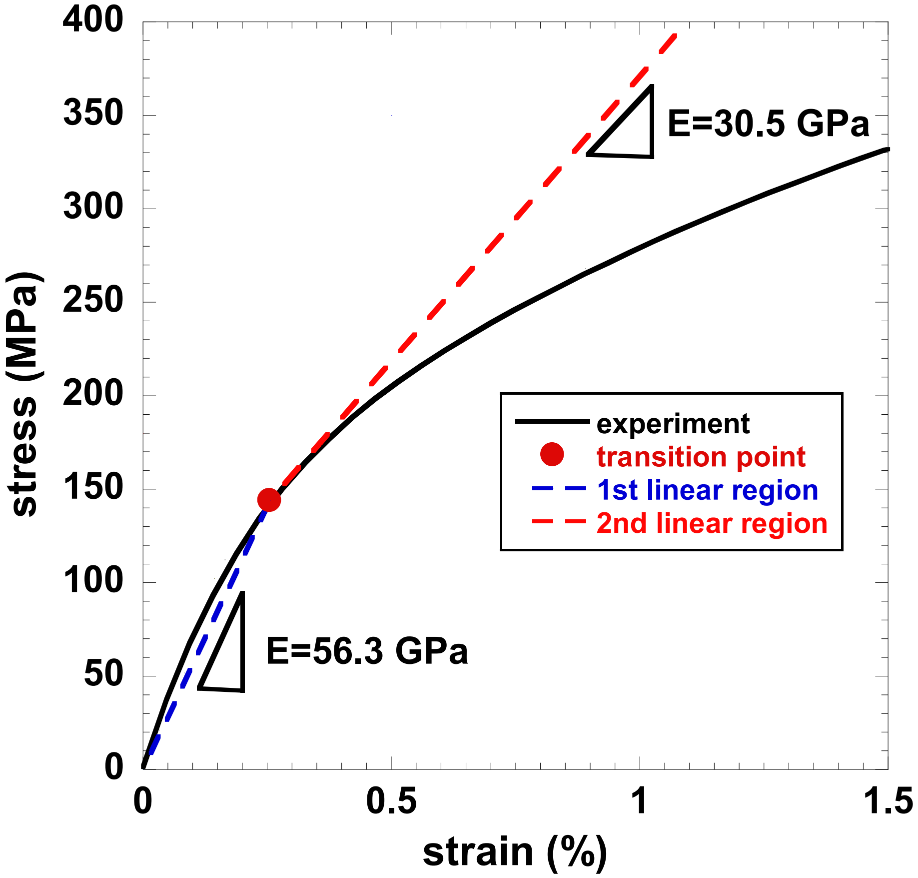

Figure 5.2: Tensile behavior at 178°C (M_s-50°C) for hot-extruded $Ni_{19.5}Ti_{50.5}Pd_{25}Pt_5$ [10] (solid line). Modeled uniaxial behavior of $Ni_{19.5}Ti_{50.5}Pd_{25}Pt_5$ from the behavior of spring *S1* (dashed lines).

5.1.3 Behaviors of spring *S1* and spring *S2*

To attempt to justify the application of linear elastic spring theory to $Ni_{19.5}Ti_{50.5}Pd_{25}Pt_5$ springs and in turn endeavor to decouple material effects from changes in geometry to overall spring behavior, the above analyses is repeated used to predict the response of a second spring geometry. Figure 5.3 shows the experimental load versus extension data acquired at room temperature from the as-shape-set spring *S2*. The predicted response of the first linear region of spring *S2* was obtained using Equation 5.2 with a modulus of 20.1 GPa obtained from the first linear region of spring *S1*. The equivalent transition point shown in Figure 5.3 for spring *S2* occurs at 0.31 N, which was chosen such that σ_{vm}^{tran} is the same for both springs. Also, shown in Figure 5.3 is the predicted response for the second linear region of spring *S2*, obtained using Equation 5.2 with a modulus of 10.9 GPa obtained from the second linear region of spring *S1*.

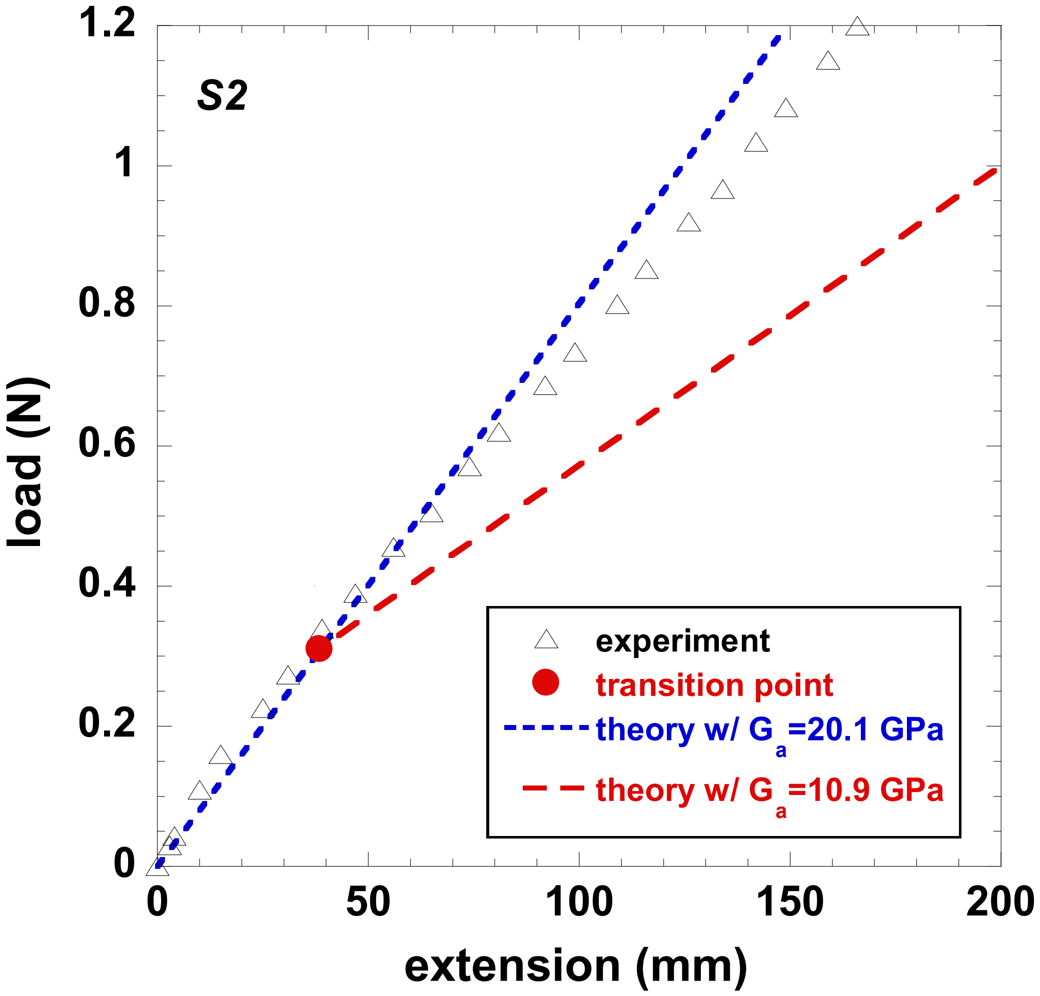

Figure 5.3: Isothermal load versus extension response of as-shape-set spring *S2* (symbols) with modeled response (dashed lines).

Figure 5.3 shows agreement within error between prediction and experiment in the first linear region, thus, further confirming elastic behavior for springs resulting with limited detwinning and/or variant reorientation at small strains. However, the response of spring *S2* is stiffer than the predicted response in the second linear region. The predicted response obtained from the first linear elastic region of spring *S1* is extended into the second region of spring *S2* to emphasize the tendency of spring *S2* to behave stiffer at loads and extensions higher than the transition point. This suggests limited detwinning and/or variant reorientation at increased extensions (i.e., at extensions higher than the onset of detwinning and/or variant reorienation in spring *S1* and the corresponding strains in the tensile sample). A possible reason for this observation is that the wire for spring *S2* was cold drawn as opposed to the wire used for spring *S1,* which was precision ground from hot-extruded rod, similar to the bulk material compared in Figure 5.2. Cold drawing of NiTi SMA wire generally produces a strong 111 fiber texture in the drawing direction and a high density of dislocations [50]. It would be expected that shape setting would reduce these effects, however not fully eliminate them.

5.1.4 Moment resulting from rotational constraint

The apparent elastic properties obtained previously were used to evaluate the moment produced at the ends of the springs during uniaxial loading while the spring ends prevented were constrained and no longer free to rotate. Figure 5.4 shows the experimental load versus moment data acquired at room temperature from the as-shape-set spring *S1*. The data was obtained while rotation was prevented in the spring by using the mechanism described in Section 3.2.1 Thermomechanical test fixture. The straight line through the data was obtained by adapting the theory from Ref. [30], where the respective degrees of twist resulting from axial (Φ_{axial}) and torsional (Φ_{torsion}) loads are as follows:

$$\Phi_{axial} = \frac{8PD^2 n}{Gd^4}\left[\frac{2\nu}{(1+\nu)}\tan\alpha\right] \tag{5.8}$$

$$\Phi_{torsion} = \frac{64MDn}{Ed^4}\left[1+(1+\nu)\tan^2\alpha + \frac{(3-7\nu-20\nu^2-8\nu^3)}{48(1+\nu)C^2}\right] \tag{5.9}$$

where *M* is the applied moment, *E* is the elastic modulus, and the remaining variables are the same as those defined for Equations 5.1 and 5.2. The respective degrees of twist were then superimposed and the resulting equation was set to zero for the case where the spring was not allowed to rotate freely to determine the moment *M* as a function of the load through:

$$M = \frac{PDE}{4G}\left[\frac{\nu}{(1+\nu)}\tan\alpha\right]\left[1+(1+\nu)\tan^2\alpha + \frac{(3-7\nu-20\nu^2-8\nu^3)}{48(1+\nu)C^2}\right]^{-1} \tag{5.10}$$

$$= \frac{PD}{2}\left[\nu\tan\alpha\right]\left[1+(1+\nu)\tan^2\alpha + \frac{(3-7\nu-20\nu^2-8\nu^3)}{48(1+\nu)C^2}\right]^{-1} \tag{5.11}$$

where the second equality results from assuming elastic isotropy. Implicit in this assumption is the fact that *E* and *G* are apparent moduli and contain anisotropic effects typically observed in SMAs. Following Ref. [28], Poisson's ratio ν was taken to be 0.4 and an initial helix angle of 5° was used for α. The straight line through the moment versus load data in Figure 5.4 was thus determined from Equation 5.11. Figure 5.4 shows some piece-wise linear behavior (see solid lines). Since the dependence on moduli (Eq. 5.11) was theoretically eliminated by assuming elastic isotropy this observed piece-wise linear behavior is attributed to elastic anisotropic behavior following detwinning and/or martensite variant reorientation. However, the observed piece-wise linear behavior is limited and relative agreement between experiment and theory in Figure 5.4 provides further evidence of limited microstructural evolution in this alloy at small strains, which is accounted for in the apparent moduli as described previously.

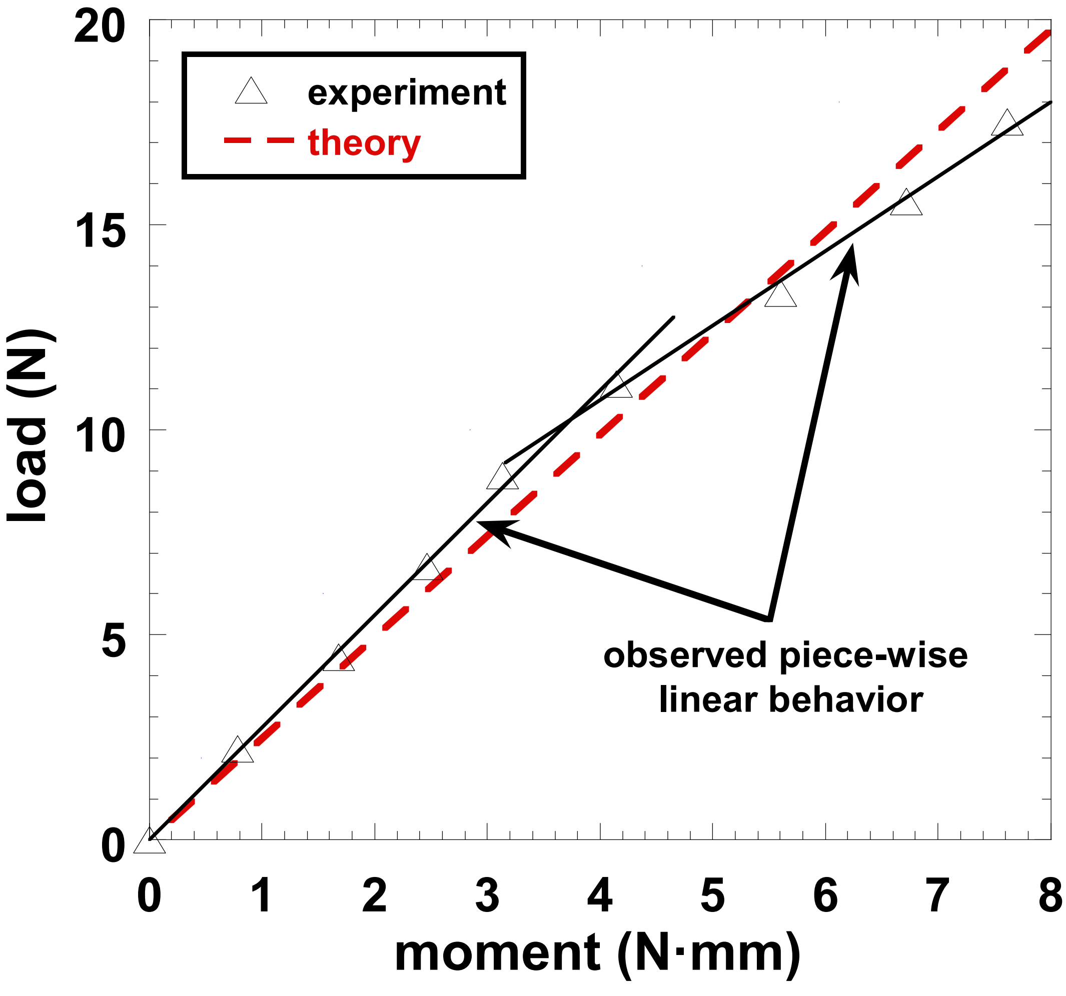

Figure 5.4: Load versus moment response of spring *S1* (symbols) with modeled response (dashed line). Possible piece-wise linear behavior due to anisotropy is shown with solid lines.

5.2 Thermomechanical cycling of $Ni_{19.5}Ti_{50.5}Pd_{25}Pt_5$ springs

5.2.1 Transformation temperatures

In the previous section, the monotonic behavior at room temperature of the as-shape set springs was presented and discussed. In the present section, the thermomechanical cycling behavior will be discussed. First, the transformation temperatures associated with spring *S1* were established under load. Figure 5.5 shows the experimental displacement-temperature data for spring *S1*, acquired using the test setup described in Section 3.2. The data was arbitrarily taken after approximately 100 cycles with a 4.4 N load, at which point there was good balance between stroke and stability. Transformation temperatures were determined by fitting tangent lines through the three distinct linear regions on both the cooling and heating curves and then extrapolating to determine the points of intersection [33]. The transformation temperatures were martensite start, M_s = 268 ^{o}C, martensite finish, M_f = 254 ^{o}C, austenite start, A_s = 263 ^{o}C and austenite finish, A_f = 273 ^{o}C and are consistent with those reported in Ref. [21].

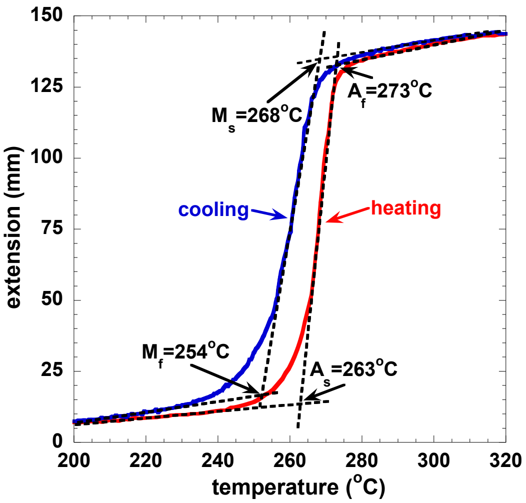

Figure 5.5: Normalized extension versus temperature results for spring *S1* under 4.4 N load with transformation temperatures determined via the intercept method.

5.2.2 Effects of thermomechanical cycling on spring geometry

Figure 5.6 shows spring *S1* before and after thermomechanical cycling. During thermomechanical cycling the load was increased every 80 cycles, and at each load the grip constraint was alternated every 20 cycles (as described in Section 3.1.3). From Figure 5.6 it can be observed that thermomechanical cycling changes the load-free length of the springs, hereafter referred to as unrecovered axial deformation. During thermomechanical cycling of the $Ni_{19.5}Ti_{50.5}Pd_{25}Pt_5$ springs, irrecoverable shape change causes unrecovered axial deformation to accumulate with each cycle. The irrecoverable shape change in this system may be attributed to formation of retained martensite, preferential selection of martensite variants under stress, which occurs predominantly in the first few cycles after a load increase, or transformation induced plasticity. All of these mechanisms have recently been shown to have a major role in the stability of NiTi based systems [21, 22].

As preferred martensite variants become biased and saturated from cycling; the saturated martensite texture should limit further detwinning and variant reorientation processes during subsequent loading of the cycled samples at room temperature. Thus, assuming constant geometry the monotonic load-extension response of the cycled spring *S1* would be expected to be stiffer (since inelastic processes such as variant reorientation and detwinning occurred during cycling) than the monotonic load-extension response of the as-shape-set spring *S1*. This idea would be consistent with results from similar $Ni_{19.5}Ti_{50.5}Pd_{25}Pt_5$ spring [28] and $Ni_{19.5}Ti_{50.5}Pd_{30}$ tensile [24] experiments. However, the spring geometry is not constant, as shown in Figure 5.6. The unrecoverable axial deformation causes an increase in helix angle and decrease in coil diameter as the free length increases while the wire length is conserved. These changes in spring geometry would also produce a stiffer monotonic response as governed by Equation 5.2.

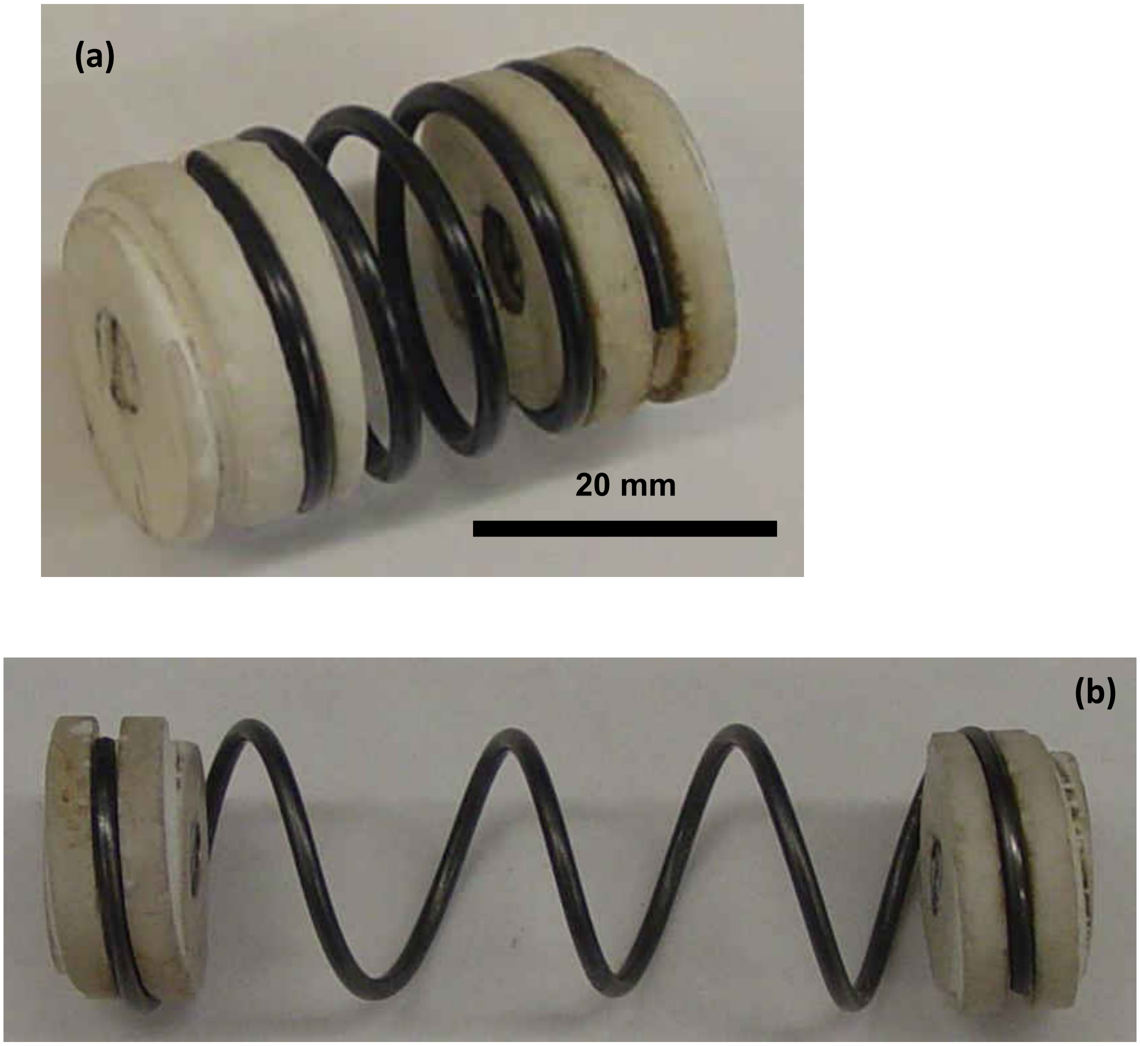

Figure 5.6: Changes in spring geometry *S1*due to thermomechanical cycling in (a) as-shape-set spring *S1*and (b) cycled spring *S1*.

5.2.3 Monotonic behavior of "cycled" $Ni_{19.5}Ti_{50.5}Pd_{25}Pt_5$ springs at room temperature

To separately investigate the role of material microstructural evolution following thermomechanical cycling in the spring, changes in spring geometry must thus be accounted for. Hence, after cycling, spring *S1* was forced back on to the mandrel to its shape set geometry and removed at room temperature. It is to be noted that when spring *S1* was removed from the mandrel, "spring back" resulted in a spring geometry slightly different but still very close to that of the as-shape-set geometry. Figure 5.1 includes the isothermal load versus extension test results from this cycled and reconfigured spring *S1* at room temperature. The monotonic response of cycled spring *S1* is the same (within error) as that of as-shape-set spring *S1*. This behavior is surprising as it does not follow the previously described expectation that the spring behavior would be stiffer due to material microstructural evolution. This unexpected response could be due to several possible reasons. At a minimum, the process of forcing back the spring on its mandrel would result in microstructural changes caused by reorientation of martensite variants and/or detwinning possibly resulting in a structure equivalent to the original as-shape-set spring. In addition, the response could be dominated by the prevailing geometry of the spring and the material microstructural evolution is homogenized and averaged by the multi-axial stress state (Equations 5.3-6) that exists in the spring or the spring simply does not evolve sufficiently to affect the response.

To further examine this issue, cycled spring *S1* was shape-set again (referred to as spring *S1-SS2* as described in Section 3.3), thermomechanically cycled 10 times under an 8.6 N load and an isothermal load versus extension test was performed on this spring without forcing the spring back on the mandrel following the cycling operation. Figure 5.1 includes the isothermal load versus extension test results for cycled spring *S1-SS2* at room temperature. The response is stiffer and non-linear in comparison to the response of as-shape-set and cycled spring *S1*.

To predict the load versus extension results for cycled spring *S1-SS2* an iterative scheme was adopted. Equation 5.2 was iterated with the following equations that relate the initial length, x_o, the helix angle, α, the extension, δ, the coil diameter D, the number of turns, n, and the length of the unwound spring L_{wire}:

$$\alpha = \sin^{-1}\left(\frac{\delta + x_0}{L_{wire}}\right) \tag{5.12}$$

$$D = \frac{L_{wire}\cos\alpha}{n\pi} \tag{5.13}$$

This iterative approach is required to account for the large helix angle in the springs, which was not the case for the theoretical predictions in the previous sections. Using an experimentally measured free length following cycling of 433 mm and apparent moduli (from respective linear regions) obtained from the as-shape-set spring *S1,* the monotonic response of the cycled spring *S1-SS2* was thus predicted (in the same manner as the "forward" prediction for spring *S2* in Section 5.1.3). Reasonable agreement between experiment and theoretical prediction was obtained despite using apparent moduli from the as-shape-set spring *S1*. This points to the deformation mechanics in the cycled spring being dominated by geometry rather than material microstructural evolution which occurred during cycling.

Accounting for the large and evolving helix angle for cycled spring *S1-SS2* resulted in a change in the transition point determined using Equation 5.7. The onset of detwinning and/or variant reorientation for the experiment was greater than the prediction. This may be attributed to texture evolution resulting from detwinning or reorientation of martensite variants. However, the aforementioned methodology still resulted in approximate agreement in the overall response between prediction and experiment, thus, eliminating the possibility that spring *S1* being forced back on to the mandrel following cycling significantly affects the microstructure with respect to the monotonic response. This result is consistent with limited microstructural evolution at small strains, or in this case forcing the spring back on the mandrel results in large spring deformation with small strains. The cycled spring *S1* continues to detwin as load is increased which is consistent with the second linear region of as-shape-set spring *S1*. This behavior is also consistent with the experimental and theoretical predictions for the case of cycled spring *S1-SS2*. This proves cycled spring *S1-SS2* is stiffer in the second linear region primarily because of spring geometry change.

To further validate the results of applying the aforementioned methodology to cycled spring *S1* the same approach is applied to cycled spring *S2*. Figure 5.7 shows the isothermal load versus extension data for cycled spring *S2* at room temperature. The free length after removing cycled spring *S2* from the mandrel was 166.4 mm. The predicted results using apparent shear moduli of 20.1 and 10.9 GPa are compared to the experimental data in Figure 5.7. The use of 20.1 GPa (the initial apparent modulus obtained from the as-shape-set spring *S1* in Equation 5.2 after correcting for geometry) resulted in good agreement over the entire loading regime investigated for spring *S2*. This result further validates the observation of limited detwinning and/or variant reorientation in the first linear region of as-shape-set spring *S1*. However, no piece-wise behavior was observed, in contrast to spring *S1*. Thus, the monotonic behavior of cycled spring *S2* is consistent with as-shape-set spring *S2*, displaying mostly linear behavior over the entire range of loads investigated. Thus, thermomechanical cycling does not modify the cold worked microstructure in cycled spring *S2*.

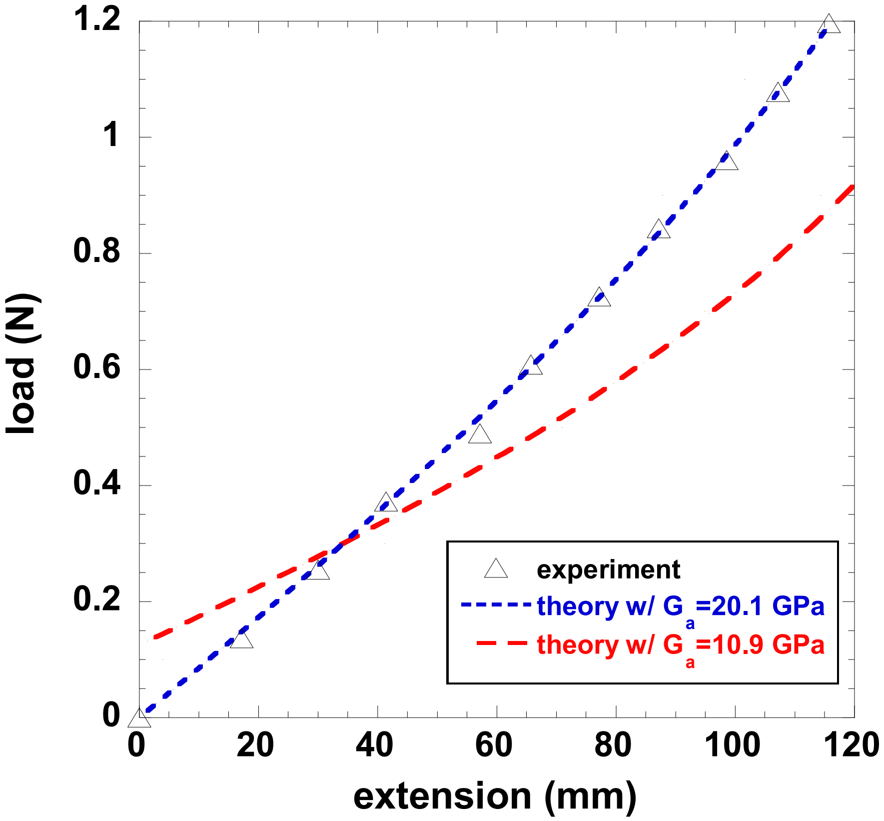

Figure 5.7: Isothermal load versus extension response of cycled spring *S2* (symbols) with modeled response (dashed lines).

5.3 Influence of rotational constraint during thermomechanical cycling

Figure 5.8a shows displacement with cycle number data for spring *S1* obtained by alternating the condition of constraint at the ends of the spring (as previously explained in Section 3.3). This was done to allow for direct comparisons of data acquired with and without rotational constraint. A close up of the 11.1 N section of the curve shown in Figure 5.8a reveals differences between the rotationally constrained and unconstrained conditions, that is the unconstrained stroke is larger than the constrained stroke.

Figure 5.8b shows stroke versus load data (first Y-axis) for the spring under both unconstrained and constrained conditions during thermomechanical cycling. The stroke was determined from the difference in length between the contracted hot and extended cold state of the spring. The stroke was measured and reported as an average from 40 cycles (from the corresponding two sets of 20 cycles each). Figure 5.8b also shows the corresponding moment-load data (second Y-axis) (i.e, the averages of the maximum moment generated during each cycle at each load) for the spring when rotationally constrained. Larger strokes were obtained for the case of the unconstrained spring and a maximum stroke is obtained at an intermediate load. Also, the maximum in the moment versus load occurred at the same load level as the maximum in the stroke versus load data. This is a result of coupling between the axial load and moment generated in the rotationally constrained spring as shown for the monotonic response in Figure 5.4.

The geometry of the spring changes due to unrecovered axial deformation and at some point it passes through a geometry in which an optimal stroke is produced. The decrease in stroke in the spring following a maximum load occurs as the geometry of the spring approaches that of a wire and is associated with a decrease in stress (as governed by Equations 5.3-7).

The increase in stroke obtained for the unconstrained spring compared to the constrained condition results from coupling between the moment generated and the axial load. It was shown in Section 5.1.4 through use of Equation 5.8 and Equation 5.9 that axial loading produces a moment in the constrained spring. On the contrary, in the unconstrained spring the moment which would be produced by the rotational constraint is manifested in the form of increased deflection. This is also aided by the microstructure as the variants selected in the unconstrained condition have fewer constraints during the phase transformation. Also, a decrease in stroke following an intermediate load may be resulting from the formation of retained martensite and plasticity from thermal cycling at increased load. This increased deflection results in increased stroke when the spring is thermomechanically cycled. The maximum moment generated during cycling at an intermediated load for the unconstrained case is also direct evidence of the aforementioned coupling.

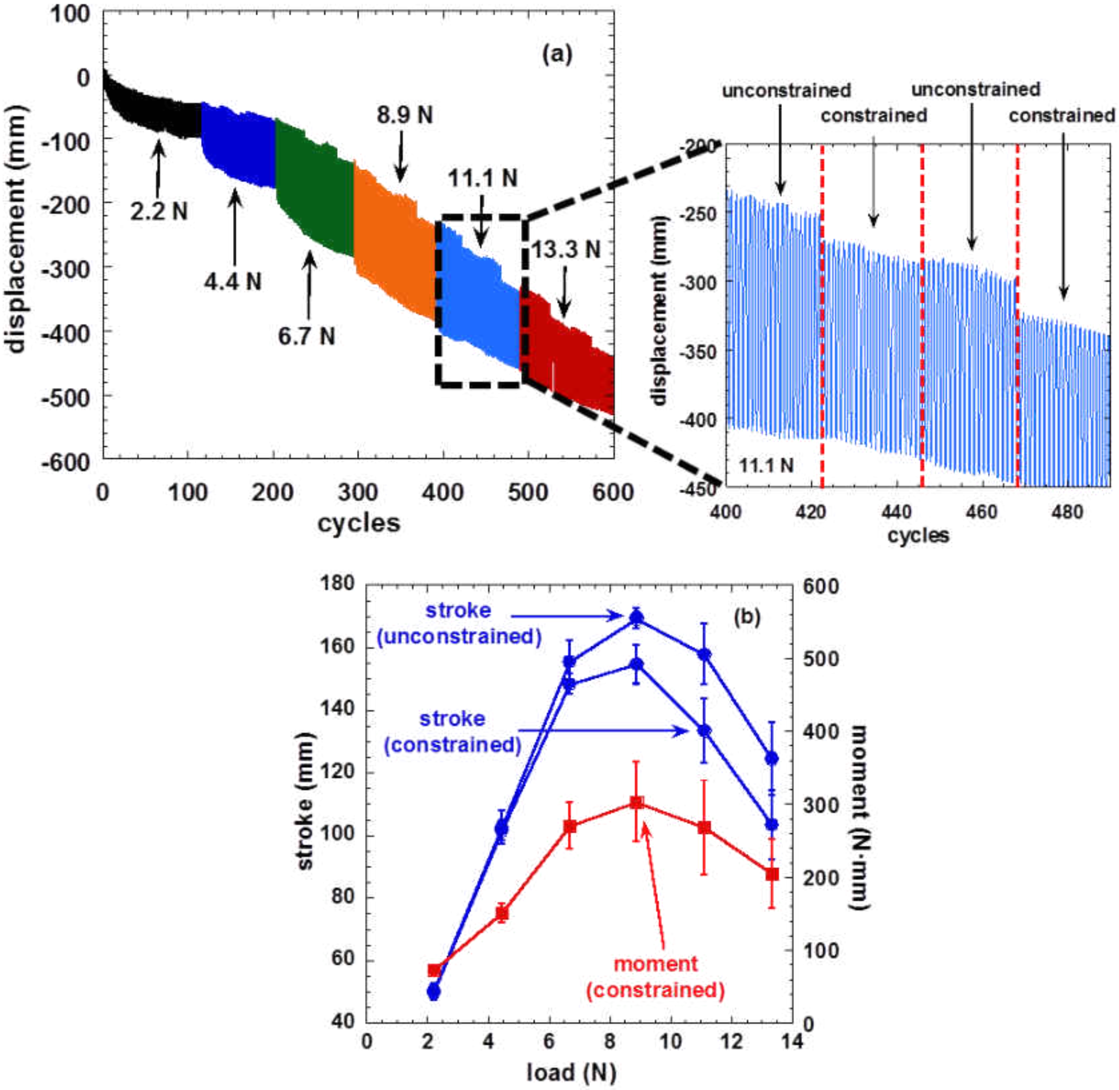

Figure 5.8: Thermomechanical response of $Ni_{19.5}Ti_{50.5}Pd_{25}Pt_5$ shape memory alloy spring *S1*: (a) raw displacement-cycle data, with alternating conditions of constraint while increasing load; (b) stroke-load data (first y-axis) for the spring under both constrained and unconstrained conditions during thermomechanical cycling. Also shown is the corresponding moment-load data for the constrained condition (second y-axis).

CHAPTER SIX: FINITE ELEMENT ANALYSIS OF $Ni_{19.5}Ti_{50.5}Pd_{25}Pt_5$ SPRINGS

In the previous chapter the adopted spring theory that was used in conjunction with apparent elastic properties acquired from the as-shape-set springs worked well in predicting $Ni_{19.5}Ti_{50.5}Pd_{25}Pt_5$ spring behavior. In this chapter non-linear spring behavior at large extensions and geometry or shape changes is investigated with the FEM using apparent elastic properties and assumptions established in Chapter 5. The FEM model was validated against available experimental monotonic spring load-extension data and corresponding analytical maximum von Mises stresses (Eq. 5.7), at stresses below the onset of detwinning and/or variant reorientation, i.e., σ_{vm}^{dev} for as-shape-set springs *S1* and *S2*. This model was then extended to post-cycled spring geometries. Outputs include spring extensions and the corresponding von Mises stress distribution. These results are then compared to the results established by analytical methods in Chapter 5. Additional analytical results from the methodology established in Chapter 5 are provided in conjunction with FEM results as needed for discussions about the evolution of stresses in the spring. The FEM procedures are given in detail in Section 3.4. Note these non-linear approach only accounts for non-linear spring mechanics as the apparent moduli obtained in Section 5.1.1 were used as input and were constant as the solution progressed to final configuration/geometry. Nonlinear material properties were assumed to be contained in the apparent moduli as justified in Chapter 5.

6.1 Finite element method model validation

Figure 6.1 shows the maximum von Mises stress with load corresponding to isothermal loading of the as-shape-set springs *S1* and *S2* at room temperature (i.e., corresponding to tests performed in Figure 5.1 and 5.3, respectively). This data was generated by both the approach presented in Chapter 5 and the FEM. Details for the FEM model used here are presented in Section 3.4. From Figure 6.1 it can be observed that the finite element model was validated within error for both spring *S1* and *S2* when compared to theory. Also, this same model was validated against the load versus extension test (Figure 5.1 and 5.3) at stresses below the onset of detwinning and/or variant reorientation σ_{vm}^{dev}.

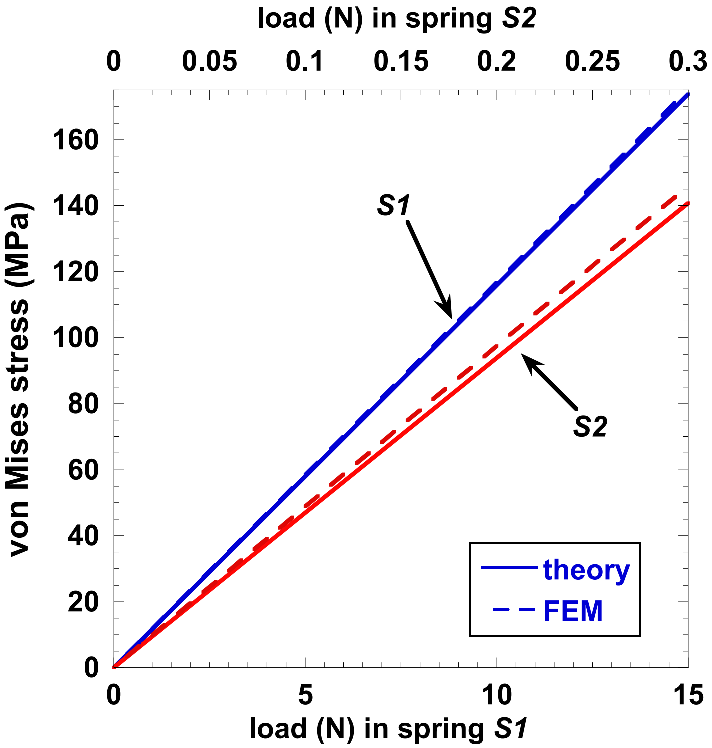

Figure 6.1: Von Mises stresses from the FEM model and elastic theory during monotonic loading of as-shape-set springs *S1* and *S2*.

6.2 Monotonic behavior of “cycled” $Ni_{19.5}Ti_{50.5}Pd_{25}Pt_{5}$ springs at room temperature

Figure 6.2a shows the isothermal load versus extension experimental results and predictions from Section 5.2.2 for cycled spring *S1* at room temperature together with the FEM results. The FEM agrees with theory (Eq. 5.2, 5.12 and 5.13) at loads below 20 N. At higher loads the FEM response gradually becomes stiffer. The error between the two predicted extensions is about 7 % at 40 N. Figure 6.2b shows the isothermal load versus extension experimental results and predictions from Section 5.2.2 for cycled spring *S2* at room temperature together with the FEM results. The FEM model agrees with the theoretical prediction (Eq. 5.2, 5.12 and 5.13) at stresses below 0.6 N. At higher loads the FEM response gradually becomes stiffer. The error between the two predicted extensions is about 18 % at 1.1 N. Under loads of 40 N and 1.1 N, springs *S1* and *S2* are under approximately the same von Mises stress (i.e., ~ 500 MPa) as governed by Equation 5.7. Increased error between the two methods of prediction in the monotonic response for spring *S2* is attributed to the increased helix angle (i.e., spring *S1* with $\alpha = 17°$ compared spring *S2* with $\alpha = 25°$) of spring *S2* compared to spring *S1* resulting from unrecovered axial deformation.

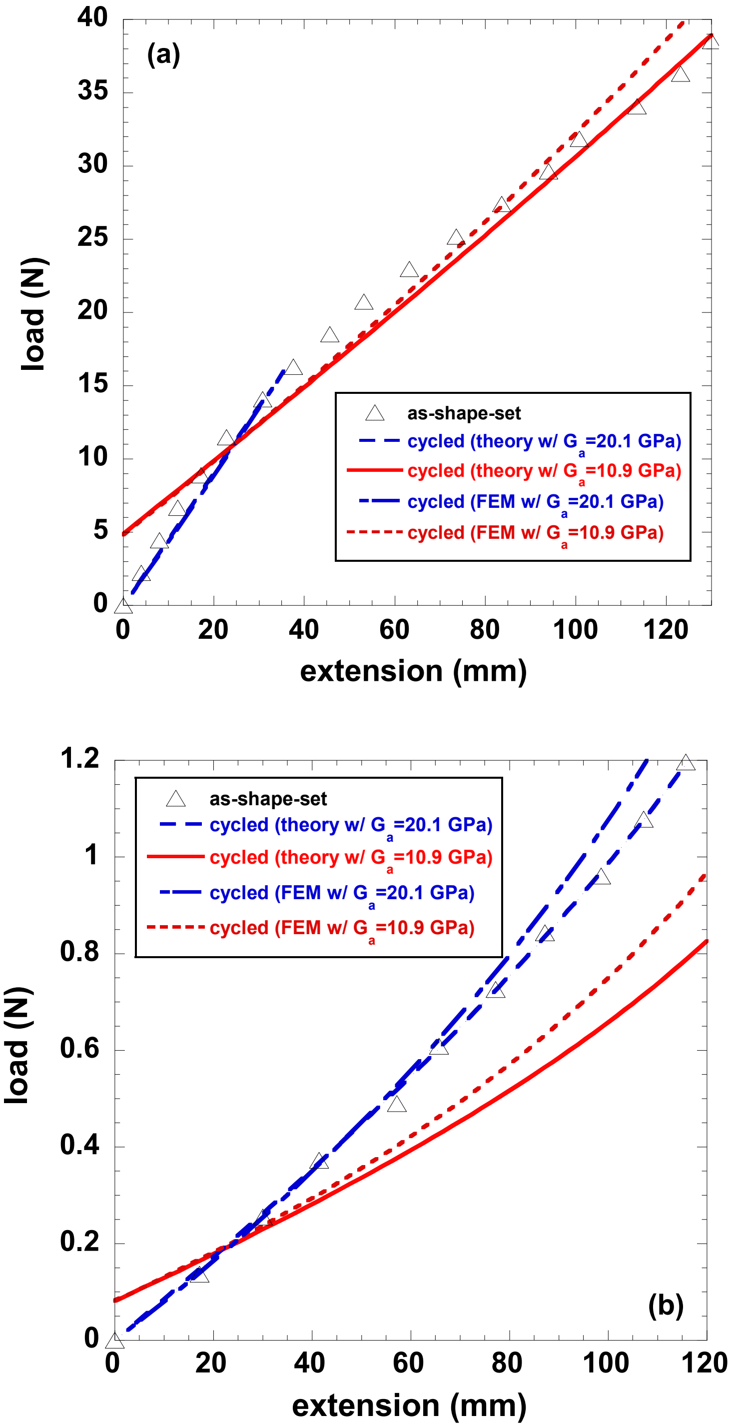

Figure 6.2: Comparisons between theory, experiment and FEM for the isothermal load-extension response of thermomechanically cycled (a) spring *S1* and (b) spring *S2*.

6.3 Evolution of stress during thermomechanical cycling

Evolution of the stress state in the springs results from evolution of the spring geometry during thermomechanical cycling. To investigate this behavior further the spring stress tensor is examined in detail. Table 6.1 summarizes all components of the stress tensor for as-shape-set and cycled spring *S1* and *S2* corresponding to a von Mises stress of 144 MPa (onset of detwinning and/or variant reorientation determined by the methodology presented in Section 5.1.2). Following cycling σ_z increases while $\tau_{\theta z}$ decreases and σ_θ remains negligible, creating a different stress state. Although, only two data points are shown, i.e., before and after thermomechanical cycling, it is expected that this stress evolution occurs continuously during each cycle as the spring geometry changes.

Table 6.1:Summary of stress tensorial components in the springs before and after thermomechanical cycling.

Spring	$\tau_{\theta z}$ (MPa)	σ_θ (MPa)	σ_z (MPa)	*P* (N)
S1 (shape-set)	82.7	-0.103	14.6	12.6
S1 (cycled)	78.3	-0.355	48.2	12.4
S2 (shape-set)	82.3	-0.047	14.6	0.31
S2 (cycled)	73.4	-0.244	68.8	0.30

Furthermore, the stress distribution evolves as a result of the changes in geometry. Figure 5.9 shows the von Mises stress distribution for the spring cross-section taken normal to the wire for various points, α = 5° (i.e. shape-set); 17° (i.e. cycled); 30°; and 45°, during the evolution of *S1*. Note, α = 5° and 17° are results from experiment, while α = 30° and 45° are extrapolated. These stresses are shown for a constant load of 10 N at room temperature. Thus, the points are in regions in which the applied methodology has been shown be accurate (i.e., at stresses below the stress at which the deviation point occurs). The amount of modeled deformation is represented by the helix angle.

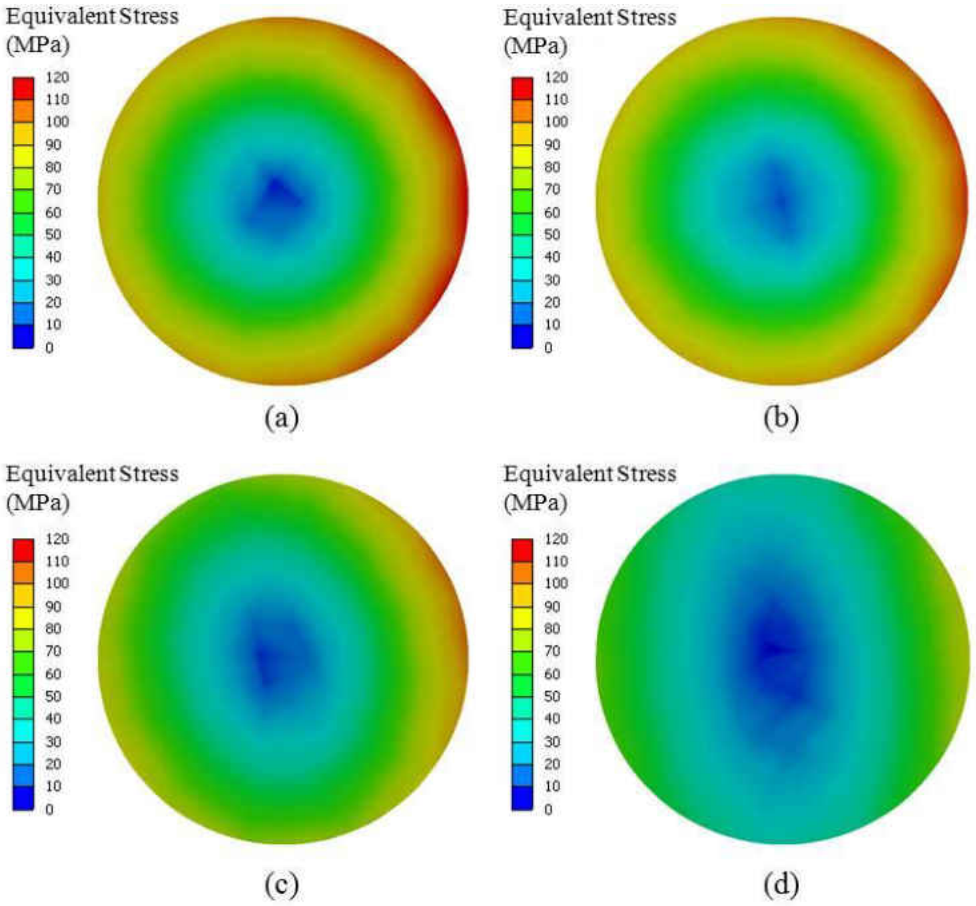

Figure 6.3: Von Mises stress distribution in spring *S1* at room temperature at a constant load of 10 N. The contour plots are shown at a cross-section normal to the spring wire and the amount of deformation is represented by the helix angle as follows: (a) α=5° (shape-set); (b) α=17° (as observed experimentally following cycling); (c) α=30°; and (d) α=45°. The spring axis is to the right of the respective plots.

In Figure 6.3 the heterogeneity of the stress in the spring can clearly be observed as it is maximum at the inner most point of the cross-section and varies to near zero at the center of the cross-section, and then increases again towards the outside of the spring. The stresses in the spring are homogeneous along the sweeping direction of the cross-section (i.e., along the wire). The stress state is independent of the number of active coils. At higher helix angles, the maximum stress begins to decrease and centro-symmetric nature of the stress state is loss. Thus, it can be clearly seen that the stress state in the spring is changing as the geometry of the spring changes with cycling.

In the case of springs, stable behavior can also arise due to geometrical considerations. Given enough load and thermomechanical cycles the spring would eventually elongate into a region where $\alpha > 60°$ and the coil diameter is near zero. In this case, the stresses will be nominal, reducing residual strain to near zero until stable behavior is achieved. This is probably a major contribution to the stability achieved in $Ni_{19.5}Ti_{50.5}Pd_{25}Pt_5$ springs after training. Also, in these regions, apparent moduli for the austenite spring are lower than the apparent moduli for the martensite spring (as reported in [28]) when geometry is not corrected for in both states. The heavily deformed spring, when martensitic, is more like a wire (i.e. it has an increased spring rate due to geometry). Upon heating the same spring to austenite it contracts, giving it a more spring like shape (i.e., it has a decreased spring constant due to geometry). Thus, the reversal of apparent moduli reported in an artifact of commonly adapted spring theories inability to capture the large deformations and is not solely due to evolution of the $Ni_{19.5}Ti_{50.5}Pd_{25}Pt_5$ microstructure as previously thought.

CHAPTER SEVEN: BEHAVIOR OF $Ni_{29.5}Ti_{50.5}Pd_{20}$ AS INVESTIGATED USING NEUTRON DIFFRACTION

In the previous chapter it was shown that irrecoverable strain led to unrecovered axial deformation in $Ni_{19.5}Ti_{50.5}Pd_{25}Pt_5$ spring actuators. Irrecoverable strain was attributed to microstructural evolution, including, martensite variant reorientation, detwinning, the buildup of retained martensite and possibly even plasticity. In this chapter microstructural evolution associated with thermomechanical cycling of $Ni_{29.5}Ti_{50.5}Pd_{20}$ is investigated using previously available neutron diffraction data [31]. Microstructural evolution is assumed to be greater in $Ni_{29.5}Ti_{50.5}Pd_{20}$ ($Ni_{29.5}Ti_{50.5}Pd_{20}$ is comparable to $Ni_{19.5}Ti_{50.5}Pd_{25}Pt_5$ without the solid solution strengthening offered by the Pt addition), thus bounding "worst case" expectations for $Ni_{19.5}Ti_{50.5}Pd_{25}Pt_5$. Experimental procedures for this data are summarized in Chapter 3. Emphasis is placed on data analysis using Rietveld refinement. Procedures for the data analysis are summarized in Chapter 4. The following sections are organized as follows. For completeness a summary of the unrefined normalized spectrum [31] is given. Additional insight into these results is given as it pertains to the subsequent analysis in the chapter. IPFs are shown to provide a detailed analysis of texture evolution. Evolution of phase volume fractions of B2 (cubic) and B19 (orthorhombic) phases are reported to show the amount of accumulated retained martensite existing above the A_f following thermomechanical cycling under load. Finally, lattice strain evolution for B19 (orthorhombic) at room temperature under no load is reported for each cycle.

7.1 Results

A series of load-bias cycles were performed *in situ* on $Ni_{29.5}Ti_{50.5}Pd_{20}$ [31]. Experimental procedures for the load-bias cycles are summarized Section 3.2. Stresses and UCT for load-bias

Cycles 0 through 7 are summarized in Table 3.2. Figure 7.1 shows a section of normalized neutron diffraction spectra for $Ni_{29.5}Ti_{50.5}Pd_{20}$ under increasing stress and UCT (i.e., Cycles 1 through 6) and a final cycle (i.e., Cycle 7) under decreased stress and UCT [31]. This spectrum was acquired from reflections with lattice planes perpendicular to the loading axis (Bank 2). Note, all UCTs were above the A_f based on transformation temperatures reported for $Ni_{29.5}Ti_{50.5}Pd_{20}$ in [24]. As stress was increased with cycling the B2 100 peak shifts to the left, indicating compressive lattice strain, as expected. A decrease in the B2 100 peak intensity occurred with increasing cycling with the exception of the final cycle. From Cycle 5 through 7 B19 100 retained martensite forms and increases with cycling.

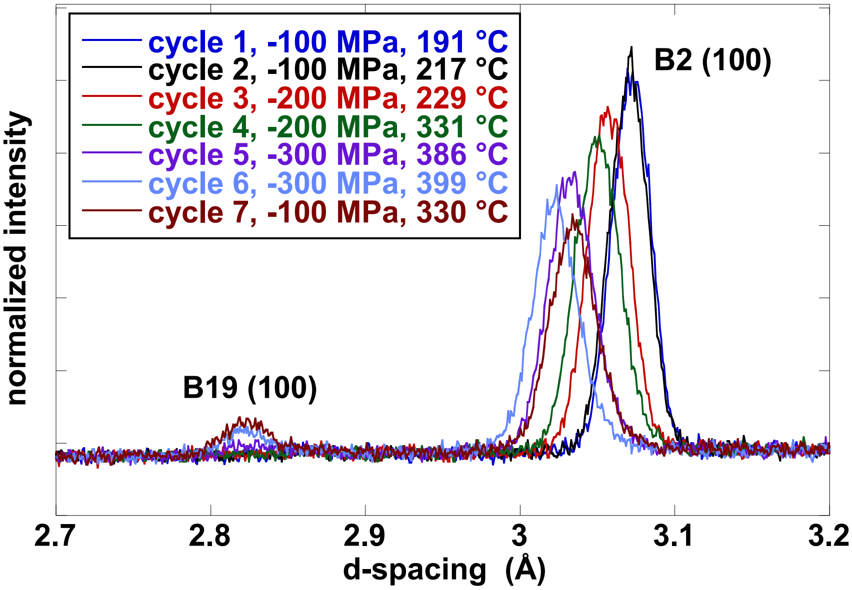

Figure 7.1: A section (d-spacing 2.7 to 3.2 Å) of normalized neutron diffraction spectra from under increasing stress and UCT (Cyles 1 through 6) and a final cycle (Cycle 7) at decreased stress and UCT [31]. The spectra are shown for reflections with lattice planes perpendicular to the loading axis (Bank 2).

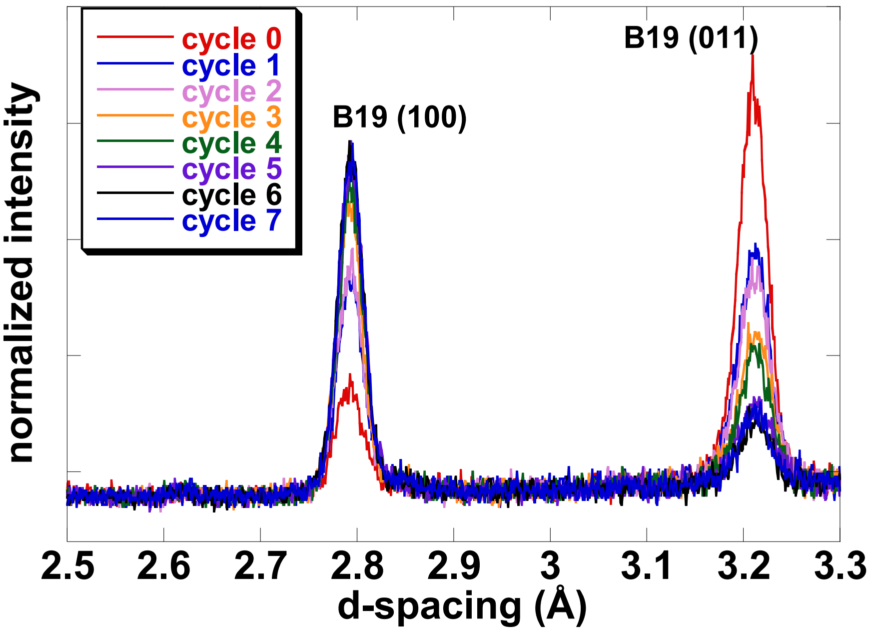

Figure 7.2: A section (d-spacing 2.5 to 3.3 Å) of normalized neutron diffraction spectrum from for $Ni_{29.5}Ti_{50.5}Pd_{20}$ under a holding load of -7 MPa at room temperature, for the as-extruded sample (Cycle 0) and following each load-bias cycle (Cycles 1 through 7) [31]. The spectra are shown for reflections with lattice planes perpendicular to the loading axis (Bank 2).

Figure 7.2 shows a section of normalized neutron diffraction spectrum for $Ni_{29.5}Ti_{50.5}Pd_{20}$ under a holding load of -7MPa at room temperature, for the as-extruded sample (Cycle 0) and following each load-bias cycle (Cycles 1 through 7) [31]. The spectra are shown for reflections with lattice planes perpendicular to the loading axis (Bank 2). The spectra encompass the 100 and 011 peaks of B19 martensite, which shows a decrease in the 011 peak intensities and increase in the 100 peak intensities with increasing cycling. The largest change in peak intensity occurred from Cycle 0 to 1. Also, larger changes in peak intensity occurred following an increase in stress during load-bias cycling (e.g., Cycles 2 to 3 stress was increased from -100 to -200MPa, see Table 3.2). Relatively small changes in the peak intensity occurred when the load-bias cycling stress was kept constant between two cycles (e.g., Cycles 1 to 2 under -100 MPa, Cycles

3 to 4 under -200 MPa and Cycles 5 to 6 under -300 MPa, see Table 3.2) although the UCT is increased in these cycles. Relatively small changes in peak intensities occurred from Cycles 6 to 7 although the load-bias cycling stress was decreased from -300 to -100 MPa.

Changes in peak intensity qualitatively indicate a change in texture with respect to individual peaks. To analyze this indication further Rietveld refinement was perform to quantify texture evolution over the entire spectra. The lattice parameters as obtained from Rietveld refinement are a=2.7977, b=4.6939 and c=4.4299 (± 0.0001Å) for B19 orthorhombic martensite and a=3.0790 (± 0.0001Å) for B2 cubic austenite. In order to minimize contributions from lattice strain from external load the lattice parameters reported here were obtained from Cycle 0 for the B19 orthorhombic martensite and from Cycle 1 for B2 cubic austenite. These values for lattice parameter agreed with the literature, in which lattice parameters were obtained from x-ray diffraction techniques, transmission electron microscopy and other neutron diffraction experiments performed on NiTiPd [18, 24, 31, 51].

Figure 7.3 shows the IPFs for Cycles 0 through 7 of B19 martensite under no load at room temperature acquired from reflections with lattice planes parallel to the loading axis (Bank 1). The numbers in the upper right hand corner of each IPF represent the maximum and minimum multiples of random distribution (MRD) of grains for some *hkl* direction (1 corresponding to a random polycrystalline material). The scale to the right also represents MRD. The initial maximum MRD in this alloy was 1.25, and is near random as expected based on the processing history of the samples (i.e., machined from hot extruded rod). Upon cycling, the maximum MRD increases until it peaks at a maximum of 1.81.

Figure 7.4 shows the IPFs for Cycles 0 through 7 of B19 martensite under no load at room temperature acquired from reflections with lattice planes perpendicular to the loading direction (Bank 2). The following can be observed in the IPFs for B19 martensite from both longitudinal and transverse directions. The largest increase in texture was observed from Cycles 0 to 1, after which the texture quickly saturated. Relatively small changes in texture occurred when the load-bias cycling stress was kept constant between two cycles (i.e., Cycles 1 to 2 under -100 MPa, Cycles 3 to 4 under -200 MPa and Cycles 5 to 6 under -300 MPa) although the UCT was increased in these cycles. A small increase in texture can be observed when the cycling stress was increased. A small decrease in texture occurred when the load bias cycling stress and UCT was decreased from Cycles 6 to 7.

Figure 7.5 shows the IPFs for Cycles 1 through 2 and 4 through 6 of B2 austenite with increasing stress and UCT (all UCTs are above A_f) and Cycle 6 through 7 with decreasing stress and UCT acquired from reflections with lattice planes parallel to the loading direction (Bank 1). It can be observed that the texture evolved slightly from random to 100 and 111 orientations being preferred. Figure 7.6 shows the IPFs for the cycles shown in Figure 7.5 acquired from reflections with lattice planes perpendicular to the loading direction (Bank 2). It can be observed that the texture devolved from 100 to random orientation. Overall the initial texture is near random and little texture evolution occurred with increasing cycle in the longitudinal and transverse directions for B2 austenite.

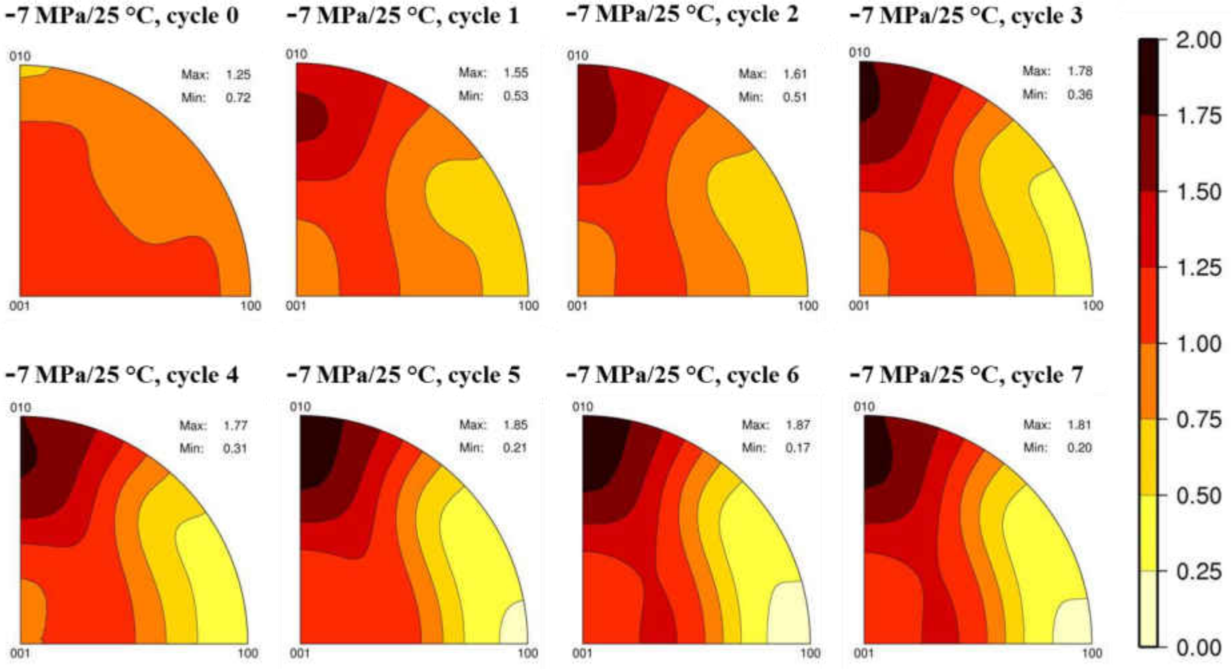

Figure 7.3: IPFs for Cycles 0 through 7 of B19 martensite under no load at room temperature acquired from reflections with lattice planes parallel to the loading axis (Bank 1).

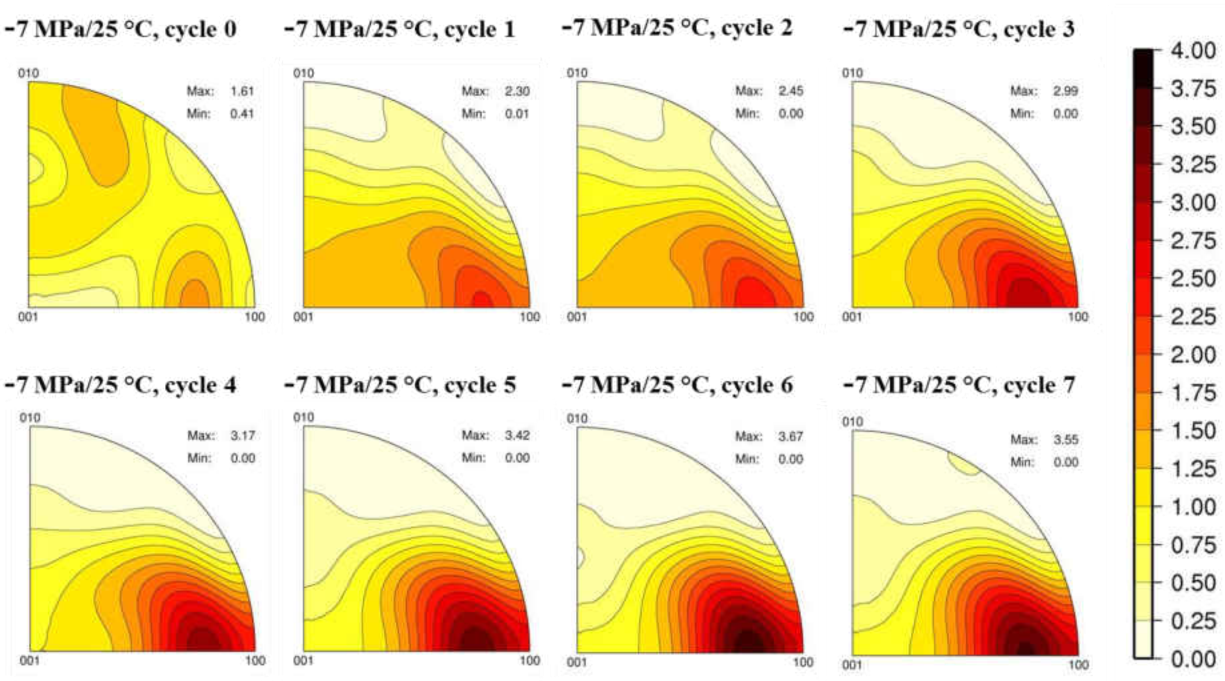

Figure 7.4: IPFs for Cycles 0 through 7 of B19 martensite under no load at room temperature acquired from reflections with lattice planes perpendicular to the loading axis (Bank 2).

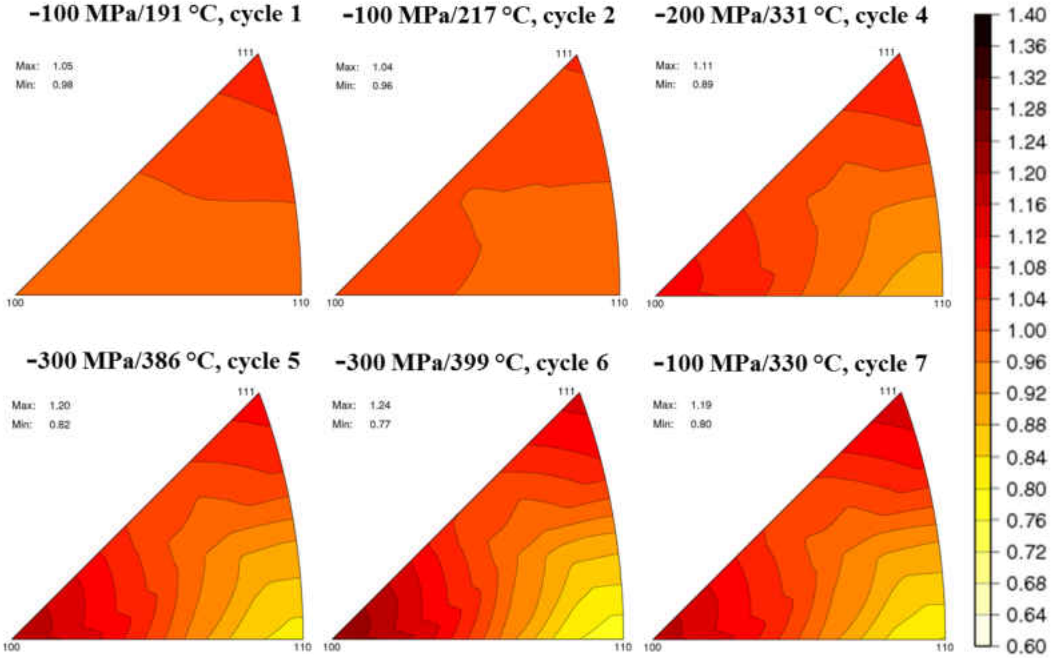

Figure 7.5: IPFs for Cycles 1 through 2 and 4 through 6 of B2 austenite with increasing stress and UCT and Cycle 6 to 7 with decreasing stress and UCT, acquired from reflections with lattice planes parallel to the loading axis (Bank 1).

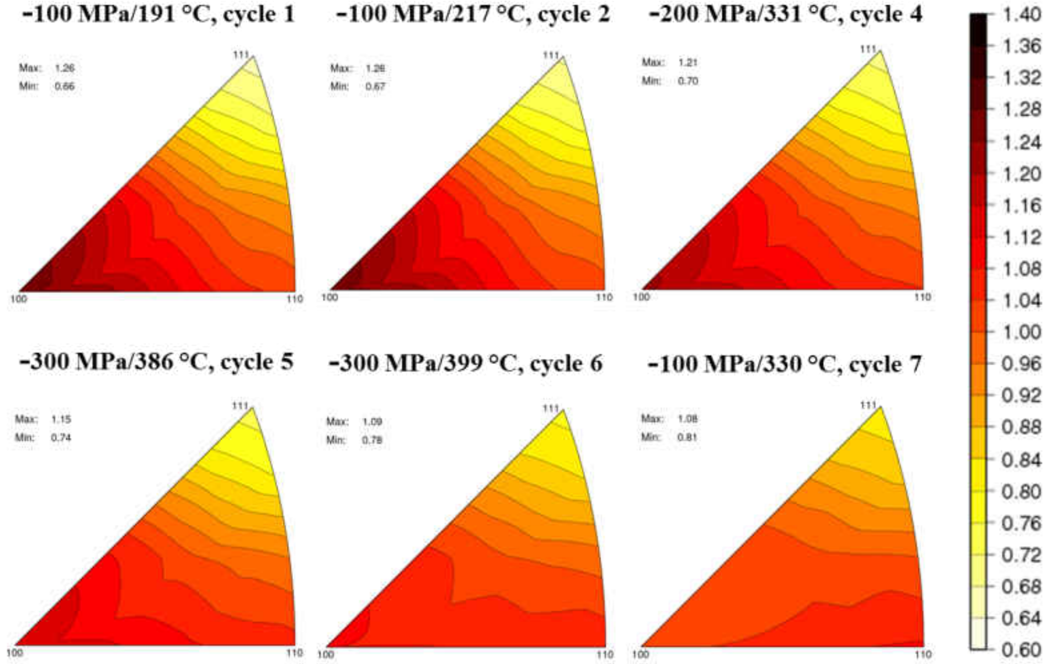

Figure 7.6: IPFs for Cycles 1 through 2 and 4 through 6 of B2 austenite with increasing stress and UCT and Cycle 6 to 7 with decreasing stress and UCT, acquired from reflections with lattice planes perpendicular to the loading axis (Bank 2).

The formation of retained martensite was observed in Figure 7.2. In order to quantify the volume fraction of B19 retained martensite and B2 austenite, Rietveld refinement was performed on both banks simultaneously as outlined in Chapter 4. Table 7.1 shows the volume fraction of retained martensite and austenite at temperatures above the A_f for Cycles 5 through 7. Note retained martensite was undetectable for Cycles 1 through 4. During Cycle 5 it was observed that 13.7 vol. % of retained martensite was present. Following Cycle 5 during Cycles 6 through 7 the retained martensite continues to increase, but appears to begin to saturate to around 20 vol. % at Cycle 7.

Table 7.1: Volume fraction (%) of retained martensite and austenite for Cycles 5 through 7.

Cycle	**Applied Load (MPa)**	**Temperature (°C)**	**Volume fraction (%)**	
			B2	**B19**
5	**-300**	**386**	**86.3**	**13.7**
6	**-300**	**399**	**81.3**	**18.7**
7	**-100**	**330**	**80.3**	**19.7**

Figure 7.7 shows the evolution of elastic lattice strain in 100, 011, 102 and 111 planes in the martensite phase under a holding stress of -7 MPa at room temperature for the as-extruded sample (Cycle 0) and following each load-bias cycle (Cycle 1 through 6). These lattice strains correspond to lattice planes perpendicular to the loading axis (Bank 2). From Figure 7.7 it can be generally observed that the lattice strains increase and then appear to level of.

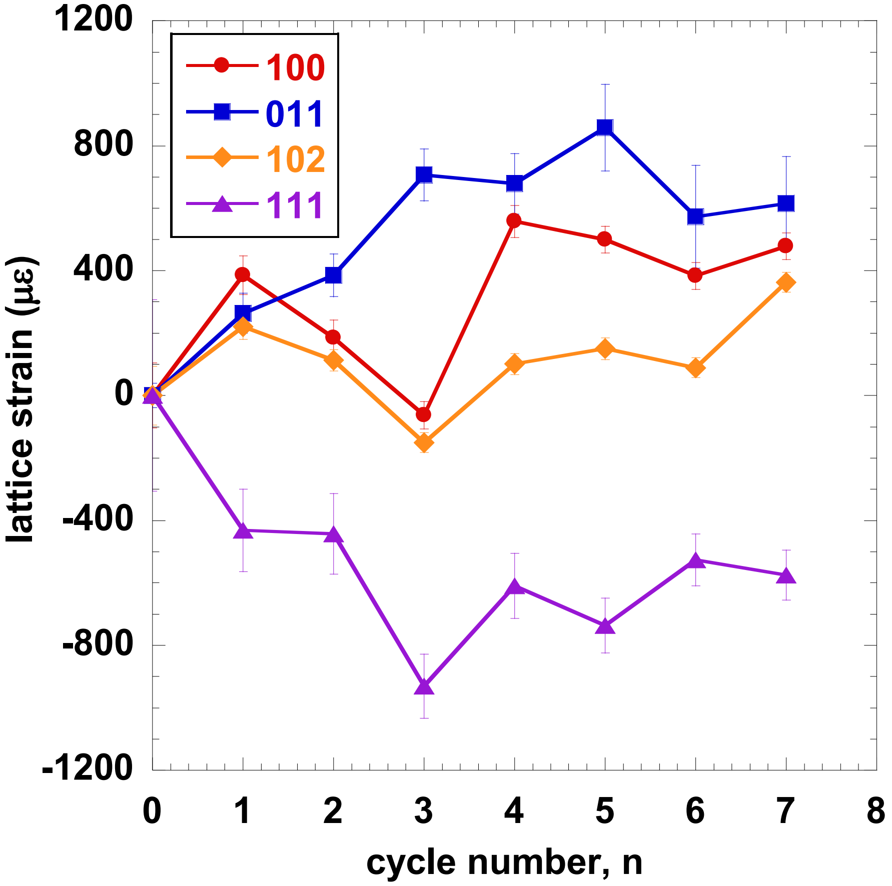

Figure 7.7: Evolution of elastic lattice strain in 100, 011, 102 and 111 planes in the martensite phase under a holding stress of -7 MPa at room temperature following each load-bias cycle. These lattice strains correspond to lattice planes perpendicular to the loading axis (Bank 2).

7.2 Discussion

In Chapter 5 it was observed that thermomechanical cycling of the $Ni_{19.5}Ti_{50.5}Pd_{25}Pt_5$ springs causes unrecovered axial deformation to accumulate with each cycle. Irrecoverable strain in this system may be attributed to microstructural evolution including martensite variant reorientation, detwinning, accumulation of retained martensite or plasticity. These mechanisms have recently been attributed to varying contributions of transformation and irrecoverable strains, throughout the thermomechanical history of the actuators. This has been observed in NiTi-based [33, 44] alloys and more specifically as it pertains to this work in NiTiPd systems [24, 25]. In the previous section results were given for data analysis of available *in situ* neutron diffraction performed on NiTiPd at SMARTS. The following sections will provide an explanation of aforementioned results in context of microstructural evolution mentioned in this work and in recent literature [24, 25, 33, 51].

7.2.1 Texture Evolution and Phase Fraction Evolution

Figure 7.4 shows texture evolution through in increase in the maximum MRD of 1.61 to ~3.55 around the 010 orientation for Cycles 0 through 7. The largest change in maximum MRD (i.e., 1.61 to 2.3) occurred on the first load bias cycle. This texture evolution is evidence of martensite variant reorientation most of which occurs during the first cycle and nearly saturates during subsequent cycles. Upon decreasing the load-bias cycling stress (from Cycle 6 through 7) there is a small devolution in the texture. This agrees with observation in the literature in which upon thermally cycling a textured NiTiPd alloy under no-load, martensite variants, given enough cycles, will reorient back to a self-accommodated state [25, 51].

From Cycle 1 through 2, 3 through 4 and 5 through 6, when the load-bias cycling stress was kept constant between two cycles, the maximum MRD increased 6.3%, 5.8% and 7.0%, respectively. The UCT was increased in each of these cycles. This suggests that UCT has little effect on texture evolution and martensite variant reorientation, under the conditions presented here. In Ref. [21] a $Ni_{19.5}Ti_{50.5}Pd_{30}$ system was load-bias cycled at a constant stress of 295 MPa while UCT was increased from 340-450°C over 110 cycles. During these experiments it was shown that a significant increase in irrecoverable strain begins when the UCT exceeds 350 °C and continues to increase as UCT is increased. A 7% increase in maximum MRD occurs between Cycle 5 at 386 °C and Cycle 6 at 399 °C under a constant load bias cycling stress of -300 MPa. Both of these cycles are performed with UCTs which have been shown to promote significant irrecoverable strain. Therefore, after the martensite variant reorientation becomes saturated following the initial cycle, further variant reorientation has little effect on the irrecoverable strain in subsequent cycles as it pertains to UCT. Also, relatively little change in the austenite texture occurs during all cycles, as shown in Figures 7.5 and 7.6. This suggests that other mechanisms are promoting irrecoverable strains at increased UCTs in the NiTiPd system. To investigate this further the phase fraction of retained martensite and austenite is quantified.

In previous work, it was shown that retained martensite forms and is detectable in $Ni_{29.5}Ti_{50.5}Pd_{20}$ when cycling under a load-bias stress of 150 MPa following the first cycle and continues to increases with no saturation [51]. During these cycles the UCT was held constant at 190°C. As shown in Table 7.1, the retained martensite is undetectable until Cycle 5 when the load-bias cycling stress reaches -200 MPa and appears to saturate by Cycle 7. Therefore, increasing UCT in this work is limiting the retained martensite from forming at decreased stress or with increased number of cycles. This is direct evidence that increasing the UCT suppresses or relieves retained martensite, while increasing the load-bias cycling stress promotes the formation and buildup of retained martensite in this system. This result is consistent with Ref. [25] which reports that retained martenites exist due to dislocation pinning of oriented martensite variants in the austenite. These dislocations may be unpinned by increasing the UCT or thermal cycling under no-load, thus allowing retained martensite to transform to austenite.

7.2.2 Lattice strain evolution

Figure 7.7 shows increases from Cycle 1 through 3 in lattice strain for the 111, 100 and 102 reflections at which point a maximum is reached. This corresponds to martensite variants preferentially reorienting during the first few cycles. Note that during Cycle 3 an intermediate UCT of 229 °C and load-bias stress of -200 MPa is reached. It has also been shown that transformation strain or recoverable strain during a load-bias cycle reaches a maximum around a UCT of 200 °C and stress of -250 MPa [24]. Thus, a favorable orientation of B19 martensite variants at an intermediate stress and UCT produces maximum transformation strain. This agrees with Ref. [33, 51], in which a similar study was performed in a binary NiTi system.

To investigate the cause and effect of retained martensite further, the lattice strain evolution for the 100 austenite reflection with vol. % retained martensite for Cycles 4, 5, 6 and 7 is shown in Figure 7.8. Note the coefficient of thermal expansion has been subtracted out, thus this data was normalized to Cycle 1. Lattice strains originally reported in Ref. [31] were only given for the 100 reflections. In this work, following the procedures in Section 4.4 lattice strains were found for the 111, 110, 210 and 211 reflections. The results are not reported, because the CTE corrected lattice strains for the 111, 110, 210 and 211 reflections were negligible compared to the 100 and/or error exceeded their value. This result is consistent with Ref. [51], in which lattice strain is a maximum in the 100 reflection as it is the more compliant direction while it was a minimum in the 111 direction as it is the stiffest direction .

Figure 7.8 shows an increase in lattice strain with increasing vol. % retained martensite up until a maximum at 18.6 vol. % on Cycle 6. A maximum lattice strain versus vol. % retained martensite was also observed in Ref. [51] at 5 vol. % retained martensite, and was attributed to internal stress mismatch being accommodated by increasing retained martensite. In this work the maximum occurs at ~18 vol. % retained martensite, because of increasing stress and UCT with each cycle.

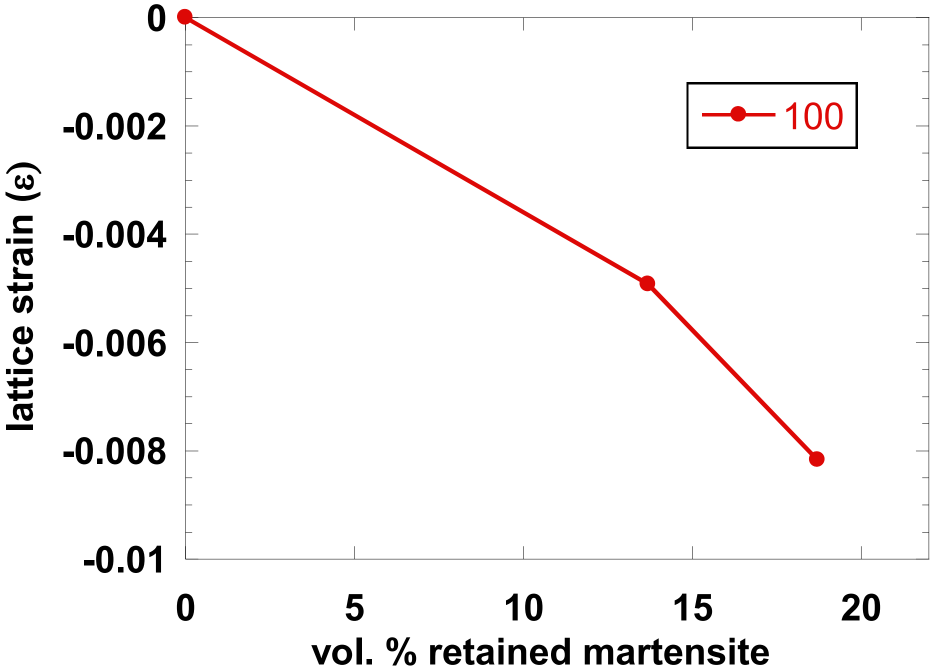

Figure 7.8: CTE corrected elastic lattice strain [31] with vol. % retained martensite in the austenite phase during load-bias Cycles 4, 5, 6 and 7. These lattice strains correspond to lattice planes perpendicular to the loading axis (Bank 2).

CHAPTER EIGHT: CONCLUSIONS AND FUTURE WORK

8.1 Conclusions

The monotonic response of $Ni_{19.5}Ti_{50.5}Pd_{25}Pt_5$ spring *S1* was experimentally observed to be piece-wise bi-linear, therefore previously established spring theory was used to fit the data and obtain apparent shear moduli for each region. Furthermore, by assuming isotropy, the overall spring behavior was compared to the uniaxial behavior of bulk $Ni_{19.5}Ti_{50.5}Pd_{25}Pt_5$. Implicit in this approach was the fact that inelastic microstructural effects (variant reorientation and detwinning) are averaged and included in the apparent moduli. With this approach, general agreement was observed in the moduli as well as the onset stress for macroscopic detwinning and variant reorientation of both the spring and the bulk material. An apparent Young's modulus of 56.3 GPa was obtained, which is expected to be considerably lower than the true elastic modulus of $Ni_{19.5}Ti_{50.5}Pd_{25}Pt_5$ based on previous measurements on a similar alloy, i.e., ~83 GPa for $Ni_{19.5}Ti_{50.5}Pd_{30}$ and based on the systematic analysis that was recently carried out for NiTi [49]. This difference in apparent versus actual moduli for $Ni_{19.5}Ti_{50.5}Pd_{25}Pt_5$ is attributed to inelastic processes such as limited detwinning and/or variant reorientation in martensite which are captured in the apparent modulus. The spring deforms linearly because initially variant reorientation and detwinning contributions are minor, similar to the case for uniaxial deformation where the initial macroscopic stress-strain curve is almost linear despite minimal variant orientation and detwinning contributions. This approach of using apparent moduli in previously established spring theory was also successful in predicting the behavior of a second spring *S2* and in quantifying the moment in spring *S1*. Thus at least for the range of deformations studied here where detwinning is minimal, anisotropic and inelastic variant reorientation and detwinning contributions to the deformation behavior can be accounted for in isotropic and linear apparent moduli, which can be used to model the behavior of $Ni_{19.5}Ti_{50.5}Pd_{25}Pt_5$ springs.

There are three reasons why this is possible. First and foremost, large spring deformation results in small strains (e.g., a 216% increase in spring *S1*'s length results in a 1.1% increase strain). The next two explanations are strengthened by the fact that the strains incurred here are small. Second, martensite in $Ni_{19.5}Ti_{50.5}Pd_{25}Pt_5$ is orthorhombic (compared to martensite in NiTi which is monoclinic in structure) and exhibits less twinning due to the higher symmetry. Thus the aforementioned anisotropic and inelastic variant reorientation and detwinning contributions can be expected to be smaller in $Ni_{19.5}Ti_{50.5}Pd_{25}Pt_5$ and not introduce significant non-linearity in the observed macroscopic behavior. This is particularly true for the case of spring *S2* where cold working of the wire results in a starting microstructure (an assumed 111 fiber texture and high dislocation density) that limits variant reorientation and detwinning. This is consistent with Ref. [52] in which the initial microstructure (in this case precipitate strengthening) limits detwinning and variant reorientation during loading and thermal mechanical cycling.. Third, using $Ni_{19.5}Ti_{50.5}Pd_{25}Pt_5$ in spring form results in a multi-axial heterogeneous stress state (for example the von Mises stress is highest at the inside of the spring cross-section, varies to near zero at the center, and then increases again towards the outside of the springs, as shown by FEM in Chapter 6). This heterogeneous stress state may result in a suppression of anisotropic effects by appropriate selection of martensite variants enabling the use of isotropic apparent moduli. Such suppression of asymmetry or anisotropy has previously been observed in NiTi [53] and NiTiPd [18] where the isothermal deformation behavior differs considerably in tension and compression but not the isobaric behavior (when variants are allowed to form under an external load during cooling).

The explanation of limited microstructure evolution at small strains and appropriate selection of variants governed by a heterogeneous stress state also holds true for the case of thermomechanical cycling. Thermomechanical cycling results in microstructural evolution (i.e., martensite variant reorientation, detwinning, retained martensite or plasticity) resulting in unrecovered axial deformation (i.e., increase in helix angle, and decrease in coil diameter) in HTSMA springs. After experimentally correcting for the unrecovered axial deformation (by rewinding on the mandrel, which causes deformation of the martensite), the apparent moduli determined from the monotonic experiments could still be used to reasonably predict the behavior of the cycled springs. Rewinding the spring back on the mandrel results in large spring deformation, however as mentioned above this results in small strains. Thus, this step should have a minimal effect on the microstructure. This assumption is confirmed by the following result. The apparent moduli also gave reasonable results when they were used in an iterative scheme that accounted for the large helix angle to predict the behavior of an extended spring following thermomechanical cycling (i.e., a spring that was not rewound on the mandrel). This again points to limited texture evolution in the martensite with cycling or a situation where in the texture is biased (i.e., variants are selected) very early on in the cycling process. It also suggests that the unrecovered axial deformation (which may result from retained martensite or plasticity) only affects the overall behavior of the spring through geometry change as the effects of microstructural evolution are limited. This is consistent with previously observed behavior in NiTi during thermomechanical cycling under load, wherein large macroscopic strains of up to

20% are observed in the sample with cycling. However, the transformation strain (difference in strain between austenite and martensite) remains mostly unchanged at about 4% despite these large macroscopic strains increasing from 0% to 20% during cycling [53].

Furthermore, larger strokes were obtained during thermomechanical cycling of rotationally unconstrained $Ni_{19.5}Ti_{50.5}Pd_{25}Pt_5$ HTSMA springs and maximum stroke was obtained at an intermediate load. The stroke obtained in the spring was dictated by the coupling between the torsional and axial loads, the resulting martensite texture, i.e., the orientation and distribution of martensite variants and the prevailing geometry and associated stress state as it evolved between a closely coiled spring to that of a wire.

Lastly, during thermomechanical cycling of the $Ni_{19.5}Ti_{50.5}Pd_{25}Pt_5$ springs, irrecoverable strain causes unrecovered axial deformation to accumulate with each cycle. Irrecoverable strain in this system may be attributed to microstructural evolution including martensite variant reorientation, detwinning, and accumulation of retained martensite or plasticity. To investigate these mechanisms further, available $Ni_{29.5}Ti_{50.5}Pd_{20}$ neutron diffraction data [31] was analyzed. Such analysis showed that significant texture evolution, indicative of martensite variant reorientation, occurred following thermomechanical cycling. The texture evolution nearly saturates after the first cycle, and is dependent on changes in load-bias stress more so than on UCT. Thermomechanical cycling under load causes retained martensite to form. Formation of retained martensite is suppressed by increased UCT. Retained martensite may be accommodated by 100 austenite. This result is consistent with Ref. [51], in which lattice strain versus vol. % retained martensite is a maximum in 100 reflection as it is the more compliant direction while it was a minimum in the 111 direction as it is the stiffest direction .

8.2 Future Work and Recommendations

The mechanisms which contribute to recoverable and irrecoverable strains in SMAs have been recognized however not fully decoupled. More specifically, the role of plasticity during the phase transformation needs to be quantified. Also, there has been very little work done investigating the evolutionary and mutli-axial response of SMAs. Thus, the author proposes additional *in situ* neutron diffraction experiments with emphasis on the role plasticity plays during the phase transformation, along with *ex-situ* and *in-situ* multi-axial SMA experiments. Understanding the multi-axial and evolutionary response of SMAs, and associated deformation mechanisms will help in developing general "state-of-art" constitutive models for predicting the thermomechanical behavior of any SMA form (e.g., wires, beams, flexures, springs, etc.). Characterization of SMAs in aforementioned various forms could be performed by taking advantage of the modularity of the test setup described in Section 3.2.

REFERENCES

[1] Calkins F T and Mabe J H 2010 Shape Memory Alloy Based Morphing Aerostructures *Journal of Mechanical Design* **132** 111012

[2] AIAA 2009 *AIAA Names Top Ten Emerging Aerospace Technologies of 2009* http://intranet.aiaa.org/industryresources/PDF/2009TopTenAerospacereRelease.pdf

[3] Szodruch J and Hilbig R 1988 Variable wing camber for transport aircraft *Progress in Aerospace Sciences* **25** 297-328

[4] Otsuka K and Wayman C M (ed) 1999 *Shape Memory Materials* (Cambridge: Cambridge University Press)

[5] Bhattacharya K (ed) 2003 *Microstructure of Martensite: Why It Forms and How It Gives Rise to the Shape-Memory Effect?* (New York: Oxford University Press)

[6] Hartl D J, Lagoudas D C, Calkins F T and Mabe J H 2009 Use of a Ni60Ti shape memory alloy for active jet engine chevron application: I. Thermomemchanical characterization *Smart Materials and Structures* **19** 10.1088/0964-1726/19/1/015020

[7] Benafan O and Vaidyanathan R 2009 A shape memory alloy controlled heat pipe based thermal switch *Proc. ASME International Mechanical Engineering Congress and Exposition* (Lake Buena Vista, FL, November 2009) **11** 107-109

[8] Krishnan V B, Bewerse C, Notardonato W U and Vaidyanathan R 2008 A thermal conduction switch based on low hysteresis NiTiFe shape memory alloy helical springs *AIP Conference Proceedings: Advances in Cryogenic Engineering Materials* **986** 3-9

[9] Duerig T W and Pelton A R (ed) 1994 *"Ti-Ni Shape Memory Alloys" in Material Properties Handbook: Titanium Alloys* (ASM International)

[10] Duerig T W, Melton K N, Stockel D and Wayman C M (ed) 1990 *Engineering Aspects of Shape Memory Alloys* (London: Butterworth-Heinemann)

[11] Duerig T, Pelton A and Stockel D 1999 An overview of nitinol medical applications *Mater. Sci. Eng. A* **273-275** 149-160

[12] Mabe J H, Calkins F and Butler G 2002 Boeing's variable geometry chevron, morphing aerostructure for jet noise reduction *47th AIAA/ ASME/ ASCE / AHS / ASC Structures, Structural Dynamics and Materials Conference* (Newport, Rhode Island, 2002)

[13] Pitt D M, Dunne J P and White E V 2002 SAMPSON smart inlet design overview and wind tunnel test. Part I: Design overview *SPIE proceedings sereies: Society of Photo-Optical Instrumentation Engineers* **4698** 13-23

[14] Pitt D M, Dunne J P and White E V 2002 SAMPSON smart inlet design overview and wind tunnel test. Part II: Wind tunnel test *SPIE proceedings sereies: Society of Photo-Optical Instrumentation Engineers* **4698** 24-36

[15] Mabe J 2008 Variable area jet nozzle for noise reduction using shape memory alloy actuators *Journal of the Acoustical Society of America* **123** 3871-3871

[16] Sholl M, Donakowski W, Gaines G A, Lampton M L, Hurwitz M, Sirk M M and Taylor E R 2003 Optics design and performance for the Cosmic Hot Interstellar Plasma Spectrometer(CHIPS) *Proc. SPIE* **5164** 63-73

[17] Noebe R D, Padula II S A, Gaydosh D, Nathal M, Biles T and Garg A 2005 Properties and potential of two (Ni,Pt)Ti alloys for use high-temperature actuator materials *Smart Structures and Materials* (San Diego, CA, February 2005) Proc. SPIE **5761** 364-375

[18] Noebe R D, Padula II S A, Bigelow G S, Rios O, Garg A and Lerch B 2006 Properties of a $Ni_{19.5}Pd_{30}Ti_{50.5}$ high-temperature shape memory alloy in tension and compression *Smart Structures and Materials* (San Diego, CA, February 2006) Proc. SPIE **6190** 279-281

[19] Noebe R D, Draper S, Gaydosh D, Garg A, Lerch B, Penney N, Bigelow G S and Padula II S A 2006 Effect of thermomechanical processing on the microstructure, properties, and work behavior of a $Ti_{50.5}Ni_{29.5}Pt_{20}$ high-temperature shape memory alloy *Shape Memory and Superelastic Technologies* (Pacific Grove, CA, May 2006) Proc. ASM International 409-426

[20] Atli K C, Karaman I, Noebe R D, Garg A, Chumlyakov Y I and Kireeva I V 2010 Improvement in the shape memory response of $Ti_{50.5}Ni_{24.5}Pd_{25}$ high-temperature shape memory alloy with scandium microalloying *Metallurgical and Materials Transactions A* **41A** 2485-2497

[21] Bigelow G S, Noebe R D, Padula II S A and Garg A 2006 Development and characterization of improved NiTiPd high-temperature shape-memory alloys by solid-solution strengthening and thermomechanical processing *Smart Materials and Structures* (Pacific Grove, CA, May 2006) Proc. ASM International 113-131

[22] Ma J, Karaman I and Noebe R D 2010 High temperature shape memory alloys *International Materials Reviews* **55** 257-315

[23] Atli K C, Karaman I, Noebe R D and Maier H J 2011 Comparative analysis of the effects of severe plastic deformation and thermomechanical training on the functional stability of $Ti_{50.5}Ni_{24.5}Pd_{25}$ high-temperature shape memory alloy *Scripta Materialia* **64** 315-318

[24] Bigelow G S, Padula II S A, Garg A, Gaydosh D and Noebe R D 2010 Characterization of Ternary NiTiPd High-Temperature Shape-Memory Alloys under Load-Biased Thermal Cycling *Metallurgical and Materials Transactions A* **41A** 3065-3079

[25] Monroe J A, Karaman I, Lagoudas D C, Bigelow G S, Noebe R D and Padula II S A 2011 Determining recoverable and irrecoverable contributions to accumulated strain in a NiTiPd high-temperature shape memory alloy during thermomechanical cycling *Scripta Materialia* **58** 1618-1628

[26] Padula II S A, Noebe R D, Bigelow G S, Culley D, Stevens M, Penney N, Gaydosh D, Quackenbush T and Carpenter B 2007 Development of a HTSMA-actuated surge control rod for high-temperature turbomachinery applications *Proc. 48th Annual AIAA Structures, Structural Dynamics and Materials Conf.* (Honolulu, HA, April 2007) **2196**

[27] Spinella I and Dragoni E 2010 Analysis and design of hollow helical springs for shape memory actuators *Journal of Intelligent Material Systems and Structures* **21** 185-199

[28] Stebner A P, Padula II S A, Noebe R D, Lerch B and Quinn D 2009 Development, characterization, and design considerations of $Ni_{19.5}Ti_{50.5}Pd_{25}Pt_5$ high-temperature shape memory alloy helical actuators *Journal Intelligent Materials Systems and Structures* **20** 2107-2126

[29] Stebner A P 2007 Developement, characterization, and application of $Ni_{19.5}Ti_{50.5}Pd_{25}Pt_5$ high-temperature shape memory alloy helical actuators *MS Thesis* University of Akron, Akron, OH

[30] Ancker C J and Goodier J N 1958 Pitch and curvature corrections for helical springs *Journal of Applied Mechanics* 466-487

[31] Krishnan V B 2007 Low Temperature NiTiFe Shape Memory Alloys: Actuator Engineering and Investigation of Deformation Mechanisms Using in Situ Neutron Diffraction at Los Alamos National Laboratory *Phd Dissertation* University of Central Florida, Orlando, FL

[32] Chang L C and Read T A 1951 Plastic deformation and diffusionless phase changes in metals - the gold cadmium beta phase *Trans. AIME* **191** 47

[33] Padula S A, Qiu S, Gaydosh D, Noebe R, Bigelow G, Garg A and Vaidyanathan R 2011 Effect of Upper-Cycle Temperature on the Load-biased, Strain-Temperature Response of NiTi *Metall. Mater. Trans. A* **Submitted**

[34] Melton K and Mercier O 1981 The mechanical properties of NiTi-based shape memory alloys *Acta Metallurgica* **29** 393-398

[35] Stoeckel D and Waram T 1991 Use of Ni-Ti shape memory alloys for thermal sensor-actuators *Active and Adaptive Optical Components, International. Society for Optical Engineering, Bellingham* **1543** 382-387

[36] Carlson H 1978 Spring designer's handbook *Mechanical Engineering, New York, Basel: Marcel Dekker, 1978* **1**

[37] Wahl A M (ed) 1963 *Mechanical Springs* (New York, NY: McGraw Hill)

[38] Grossmann C, Frenzel J, Sampath V, Depka T, Oppenkowski A, Somsen C, Neuking K, Theisen W and Eggeler G 2008 Processing and property assessment of NiTi and NiTiCu shape memory actuator springs *Materialwissenschaft und Werkstofftechnik* **39** 499-510

[39] Grossmann C, Frenzel J, Sampath V, Depka T and Eggeler G 2009 Elementary transformation and deformation processes and the cyclic stability of NiTi and NiTiCu shape memory spring actuators *Metallurgical and Materials Transactions A* **40** 2530-2544

[40] Lagoudas D C (ed) 2008 *Shape memory alloys: modeling and engineering applications* (Springer Verlag)

[41] Arbogast D J, Ruggeri R T and Bussom R C 2008 Development of a 1/4-scale NiTinol actuator for reconfigurable structures 2008) SPIE **6930** 69300L

[42] Webster J 2006 High integrity adaptive SMA components for gas turbine applications 2006) SPIE **6171** 61710F

[43] Bourke M A M, Dunand D C and Ustundag E 2002 SMARTS - A spectrometer for strain measurement in engineering materials *Appl. Phys. A* **74** S1707

[44] Qiu S, Krishnan V B, II S A P, Noebe R D, Brown D W, Clausen B and Vaidyanathan R 2009 Measurement of the lattice plane strain and phase fraction evolution during heating and cooling in shape memory NiTi *Appl. Phys. Lett.* **95** 141906

[45] Von Dreele R B 1997 Quantitative texture analysis by Rietveld refinement *J. Appl. Cryst.* **30** 517-525

[46] NIST 2007 *Crystallography Resources* http://www.ncnr.nist.gov/xtal/software/downloads.html

[47] Larson A C and Von Dreele R B 2004 General Structure Analysis System (GSAS) *Los Alamos National Laboratory Report LAUR 86-748*

[48] Clausen B 2005 *SMARTSware* http://public.lanl.gov/clausen/SMARTSware.html

[49] Qiu S, Clausen B, Padula Ii S A, Noebe R D and Vaidyanathan R 2011 On elastic moduli and elastic anisotropy in polycrystalline martensitic NiTi *Acta Materialia* **59** 5055-5066

[50] Gall K, Tyber J, Brice V, Frick C P, Maier H J and Morgan N 2005 Tensile deformation of NiTi wires *Journal of Biomedical Materials Research Part A* **75A** 810-823

[51] Qiu S 2010 Investigation of thermal, elastic and load-biased transformation strains in NiTi shape memory alloys *Phd Dissertation* University of Central Florida, Orlando, FL

[52] Benafan O, Noebe R D, Padula S A, Brown D W and Vaidyanathan R 2011 Thermomechanical Charaterization of a Stable New High Temperature NiTiHf Shape Memory Alloy *Acta Materialia* **Submitted**

[53] Benafan O, Qiu S, Padula S A, Noebe R D, Clausen B, Sisneros T A and Vaidyanathan R 2011 Unpublished NASA GRC Results **to be submitted**